Astronomy Letters, Vol. 28, No. 11, 2002, pp. 721–726. Translated from Pis'ma v Astronomicheskiĭ Zhurnal, Vol. 28, No. 11, 2002, pp. 803–808.
Original Russian Text Copyright © 2002 by Nesterov, Volvach.

Studies of the Quasar OH 471

N. S. Nesterov and A. E. Volvach*

Crimean Astrophysical Observatory, Katsiveli, Crimea, 98688 Ukraine

Received January 21, 2002

Abstract—Based on the 1964–1996 observations in the frequency range 0.325–90 GHz, we study peculiarities of the variability of the quasar OH 471 ($z = 3.4$). The double-humped spectrum had peaks at frequencies near 1 and 20 GHz. The flux density of the low-frequency component first decreased and then began to increase. The high-frequency component rose to 2.5 Jy in the late 1970s. The peak frequencies were virtually constant. VLBI observations at 1.6 GHz revealed a core–jet structure with the jet extended eastward to 5 mas. The object is a powerful quasar. © *2002 MAIK "Nauka/Interperiodica"*.

Key words: *active galactic nuclei, quasars and radio galaxies*.

INTRODUCTION

The radio source 0642+449 (OH 471) is a high-redshift ($z = 3.402$) quasar. Carswell and Strittmatter (1973) and Gearhart *et al.* (1974) determined its spectrum in the frequency range from 16.7 MHz to 85.3 GHz and pointed out its possible variability at high radio frequencies. In early 1978, the quasar had a large high-frequency excess (Efanov *et al.* 1981). The optical observations by Pica *et al.* (1980) revealed a possible variability in this spectral range as well.

Here, our goal is to study the structure and variability of the quasar OH 471 in the radio range.

OBSERVATIONS AND DATA REDUCTION

The observations of the quasar OH 471 were carried out with the 22-m radio telescope (RT-22) at the Crimean Astrophysical Observatory and with the 14-m radio telescope (RT-14) at the Metsähovi Station (Helsinki University of Technology) at 22 and 37 GHz (Efanov *et al.* 1981; Salonen *et al.* 1987; Teräsranta *et al.* 1992; Nesterov *et al.* 2000) and with the Westerbork Synthesis Radio Telescope (WSRT) (Nesterov *et al.* 2002) at 307–385 MHz and 5 GHz.

VLBI studies of the structure of the quasar OH 471 were carried out in 1997 on the European VLBI Network (EVN) in left-hand circular polarization at a frequency of 1.6 GHz. The signal was recorded with the Mark III system. Table 1 lists parameters of the radio telescopes and Fig. 1 shows the coverage of the UV plane. A correlation analysis of the data was performed at the Max-Planck-Institut für Radioastronomie in Bonn. The initial data were edited and calibrated with the NRAO AIPS (Astronomical Image Processing System) software package using the temperatures of the system and the calibration sources DA 193 and 3C 286 measured during the observations. The DIFMAP, self-calibration, and CLEAN software packages were used for imaging.

RESULTS AND DISCUSSION

Figure 2 shows flux-density variations in the quasar OH 471 at 325 MHz, 1.4, 2.7, 5, 11, 22, 37, and 90 GHz. The RT-22, RT-14, and WSRT data were supplemented with the observations by Gearhart *et al.* (1974) and Perley (1982) at 1.4 GHz, Altschuler and Wardle (1976) at 2.7 GHz, Pauliny-Toth *et al.* (1978) at 2.7 and 11 GHz, Gurvits *et al.* (1992) at 5 GHz, Simard-Normandin and Kronberg (1978) at 11 GHz, Schwartz and Waak (1978) at 90 GHz, and Teräsranta *et al.* (1998) at 22, 37, and 90 GHz.

Table 1. Parameters of the antennas involved in the VLBI observations of the quasar OH 471

VLBI station	Antenna diameter, m	SEFD, Jy
Effelsberg	100	20
Medicina	32	580
Onsala	25	390
Jodrell Bank Mk2	26	320
Toruń	32	200
Shanghai	25	2000

Note: SEFD is the system equivalent flux density.

---

*E-mail: `volvach@crao.crimea.ua`

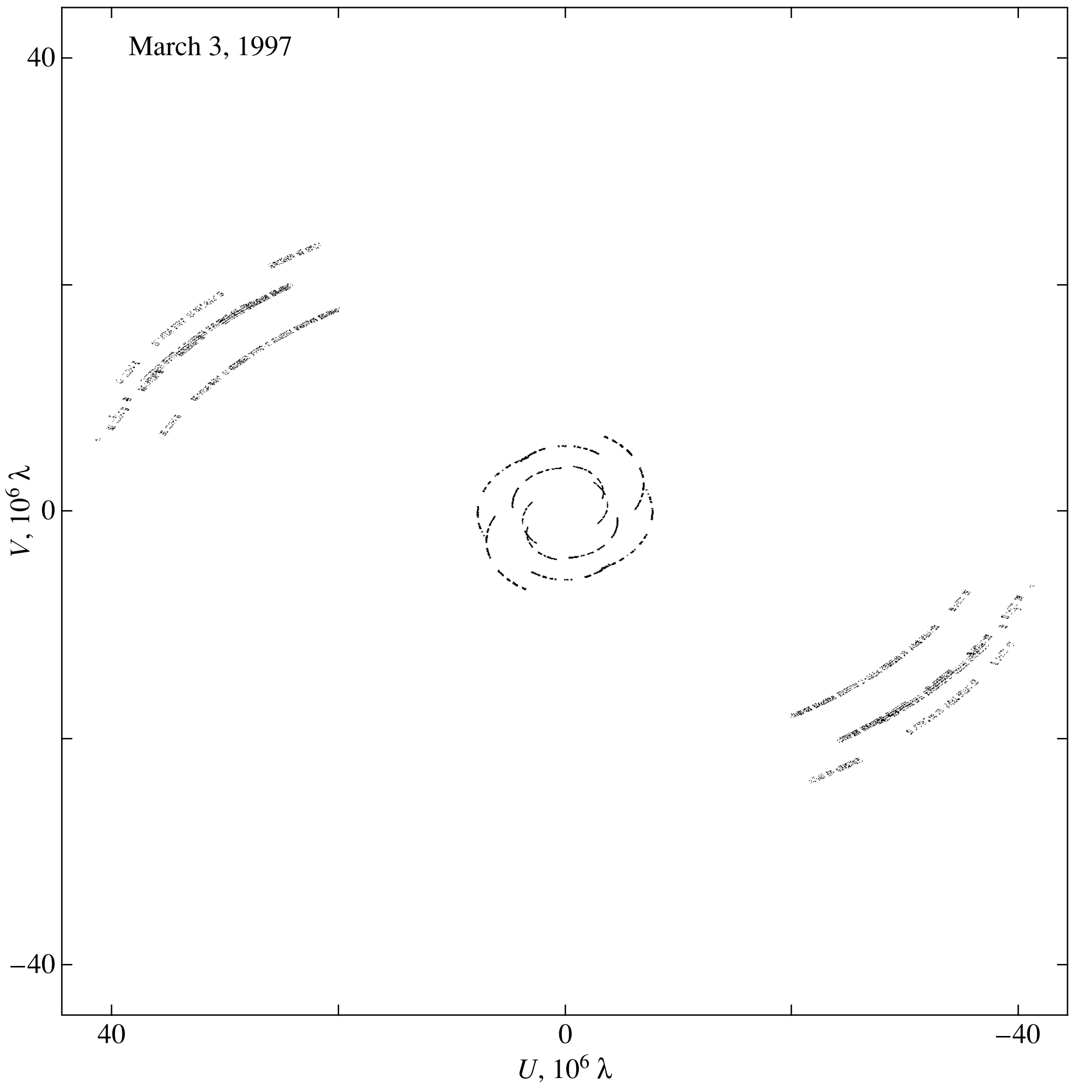

Fig. 1. Coverage of the UV plane during the 1.6-GHz observations of OH 471 in 1997.

We see from Fig. 2 that there are variations in the radio emission from the quasar OH 471 at low ($f < 5$ GHz) and high ($f > 5$ GHz) frequencies. Thus, the source flux density at low frequencies had decreased since the early 1970s. Since the late 1970s, the flux density at high frequencies had increased. Having reached its highest value in the early 1980s, the flux density at 22 and 37 GHz subsequently underwent secondary variations about 2.5 Jy. According to the WSRT observations, since the mid-1980s, an increase in the 325-MHz flux density of the quasar was recorded. Unfortunately, the observations at frequencies above 90 GHz are too few to analyze in detail the intensity variations at these frequencies.

Figure 3 shows the spectra of OH 471 that we constructed for several epochs from 1970 until 1996. As follows from Fig. 3, the radio spectrum of the quasar peaked at about 1 GHz and was, probably, flat at frequencies above 5 GHz from 1970 until 1973. In the ensuing years, there were processes that led to the evolution of the radio spectrum. In the late 1970s, an intense component appeared at high frequencies. From the early 1980s until the mid-1990s, the spectrum had a peak at about 20 GHz. No significant frequency shift of the peak with time was recorded.

Table 2 lists the spectral indices (defined as $F \sim f^{-\alpha}$) for the low- and high-frequency spectral components of OH 471 for various epochs. It gives the mean date, spectral indices of the ascending (optically thick) and descending (optically thin) branches of the spectrum, and their errors. As follows from Table 2, the spectral indices of the ascending and descending branches of the low-frequency spectral component decreased with time, while the spectral index of the ascending branch of the high-frequency component increased.

Table 2. Data on the low- and high-frequency spectral components

Date, year	Low-frequency component		High-frequency component	
	α_B	α_H	α_B	α_H
1970	-0.70 ± 0.36	0.55 ± 0.16	–	–
1973	-0.85 ± 0.54	0.46 ± 0.02	–	–
1978	–	–	-0.74 ± 0.14	–
1981	–	0.13 ± 0.05	-0.87 ± 0.09	–
1984	–	–	–	0.56 ± 0.11
1987	–	–	-0.51 ± 0.34	0.63 ± 0.06
1990	–	–	-0.45 ± 0.03	–
1996	–	–	–	–

Figure 4 shows a plot of correlated flux density against the baseline for the quasar OH 471. The decrease in the signal amplitude with an increasing baseline suggests that the source structure is unresolved. A 1.6-GHz map of OH 471 is shown in Fig. 5.

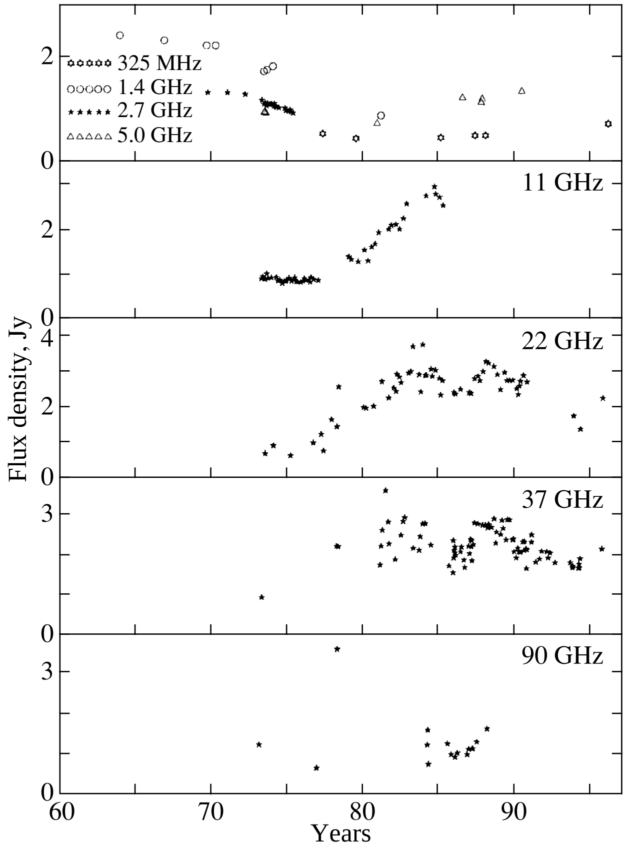

Fig. 2. Flux-density variations in OH 471 over the last 35 years.

The VLBI map at 1.6 GHz has the following parameters:

Source	0642+449
Intensity levels, % of peak flux density	−1, 1, 2, 5, 10, 25, 50, 99
Peak flux density, Jy/beam	0.328
Beam width:	
major axis, mas	12.8
minor axis, mas	2.55
position angle, deg	−24

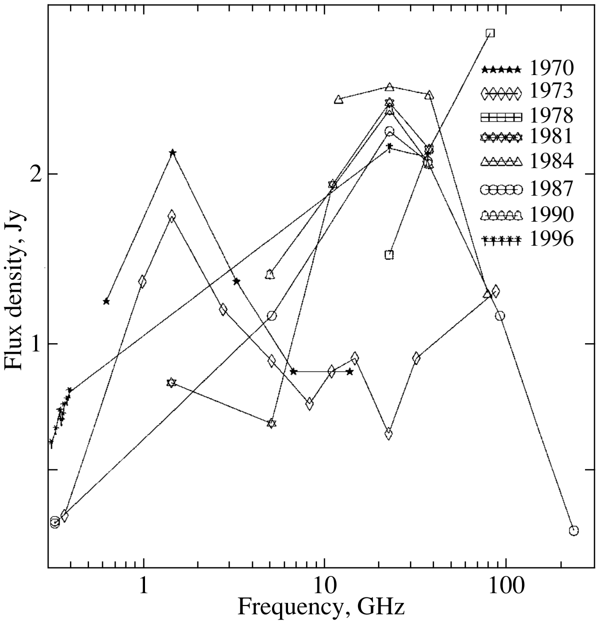

Fig. 3. The spectra of the radio source OH 471 from 1970 until 1996.

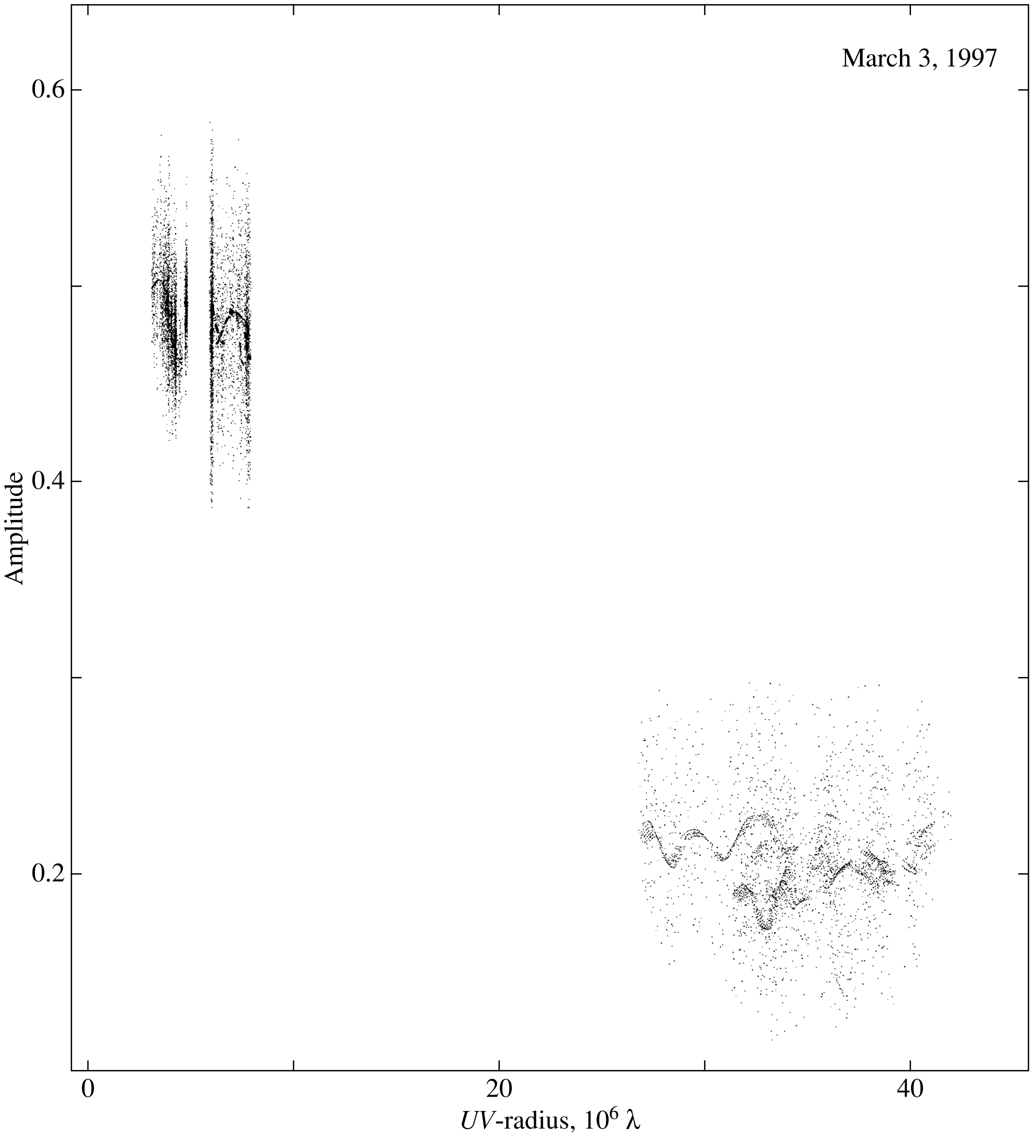

Fig. 4. The correlated 1.6-GHz flux density of the quasar OH 471 in 1997.

The results of the VLBI studies of the OH 471 structure are compared in Table 3. Its columns give the following: the epoch and frequency of observation, the source structure, the core/jet flux density ratio, and references to the publication. As we see from Table 3, the VLBI observations of OH 471 were carried out mainly in the low-frequency spectral range. Only in 1991 and 1995 was the source observed at low and high frequencies. In 1991, a compact structure of the source was detected at 22 GHz and a core–jet structure with the jet of about 3 mas in length was detected at 1.6 GHz. In 1995, a core–jet structure was also observed at 15 GHz at the detection limit (Kellermann *et al.* 1998). At a low frequency, a core–jet structure with the jet of about 3.5 mas in length was confidently detected (Fey and Charlot 1997). In 1997, our 1.6-GHz VLBI observations revealed a core–jet structure with the jet of about 5 mas in length.

Thus, the core size is about 1 mas and its peak brightness temperature is $\sim 10^{11}$ K. The jet size increases with wavelength due to an increase in optical depth.

Our data suggest that OH 471 is one of the most intense radio sources among the known quasars in the millimeter wavelength range.

Note that because of the Doppler effect, the frequencies of the quasar observations in the source's frame of reference increase by a factor of $(z+1)$. Therefore, the frequencies of the spectral peaks (Fig. 2) correspond to 4.4 GHz and 88 GHz. Thus, we can assume that the model of OH 471 is the

Table 3. VLBI observations of OH 471

Epoch	f, GHz	Structure	F_c/F_j, Jy	Reference
–	8	H	<1*	Gubbay *et al.* (1977)
–	1.6	K	1.2*	Marscher and Shaffer (1980)
1987.734	5	OJ, 7.4 mas	0.9/0.23	Gurvits *et al.* (1992)
1991.500	22	C	1.7*	Bloom *et al.* (1999)
1991.522	5	OJ, 3.03 mas	1.57/0.1	Xu *et al.* (1995)
1991.961	1.6	OJ, 3.16 mas	0.29/0.18	Polatidis *et al.* (1995)
1991.930	1.4	U	0.48*	Xu *et al.* (1995)
1995.353	15	OJ, at detection limit	1.73*	Kellermann *et al.* (1998)
1995.869	2.3	OJ, 3.7 mas	0.7/0.11	Fey and Charlot (1997)
	8.5	OJ, 3.3 mas	1.83/0.05	

Note: C—compact, U—unresolved, OJ—one-sided jet.
* Peak flux density.

model of a source with a spectral peak in the gigahertz frequency range (GPS source) (O'Dea *et al.* 1991). These radio sources are characterized by spectra with narrow peaks in the gigahertz frequency range, by a low polarization of their radio emission, by a high radio luminosity, and by a compact radio structure. Such sources are probably formed when radio-emitting relativistic plasma is compressed in the region of narrow emission lines by a dense and clumpy interstellar medium. The quasars that belong to this class of sources have high redshifts and can be located in protogalaxies with dense thermal plasma and a dusty interstellar medium.

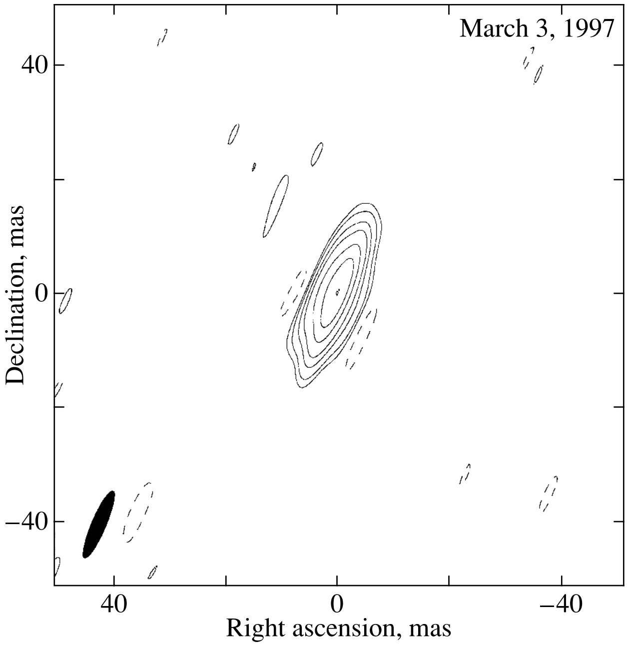

Fig. 5. The VLBI map of OH 471 obtained at 1.6 GHz in 1997; the map center is $\alpha = 0.6^h46^m32^s.0.26$, $\delta = +44°51'16''.590$.

CONCLUSIONS

Our data suggest that OH 471 is one of the most intense quasars among the known quasars in the millimeter wavelength range.

Our 1.6-GHz VLBI observations revealed a complex structure of the radio source OH 471: a core–jet with the jet extended eastward to 5 mas.

Changes in the quasar radio spectrum were recorded over the last 30 years spanned by observations. The intensity of the low-frequency component decreased in the early 1970s. An intense component appeared at high frequencies (20 GHz) in the late 1970s. From the early 1980s until the mid-1990s, the high-frequency component dominated in the spectrum of OH 471.

REFERENCES

1. D. R. Altschuler and J. F. C. Wardle, Mon. Not. R. Astron. Soc. **82**, 1 (1976).
2. S. D. Bloom, A. P. Marscher, E. M. Moore, *et al.*, Astrophys. J., Suppl. Ser. **122**, 1 (1999).
3. R. F. Carswell and P. A. Strittmatter, Nature **242**, 396 (1973).
4. V. A. Efanov, I. G. Moiseev, N. S. Nesterov, *et al.*, Izv. Krym. Astrofiz. Obs. **64**, 103 (1981).
5. A. L. Fey and P. Charlot, Astrophys. J., Suppl. Ser. **111**, 95 (1997).

6. M. R. Gearhart, J. D. Kraus, B. H. Andrew, *et al.*, Nature **249**, 743 (1974).
7. J. Gubbay, A. J. Legg, D. S. Robertson, *et al.*, Astrophys. J. **215**, 20 (1977).
8. L. I. Gurvits, N. S. Kardashev, M. V. Popov, *et al.*, Astron. Astrophys. **260**, 82 (1992).
9. K. I. Kellerman, R. C. Vermeulen, J. A. Zensus, and M. H. Cohen, Astron. J. **115**, 1295 (1998).
10. A. P. Marscher and D. B. Shaffer, Astron. J. **85**, 668 (1980).
11. N. S. Nesterov, A. E. Vol'vach, and I. D. Strepka, Pis'ma Astron. Zh. **26**, 249 (2000) [Astron. Lett. **26**, 204 (2000)].
12. N. S. Nesterov, A. E. Vol'vach, and S. V. Pogrebenko, Pis'ma Astron. Zh. **28**, 728 (2002) [Astron. Lett. **28**, 656 (2002)].
13. C. P. O'Dea, S. A. Baum, and C. Stanghellini, Astrophys. J. **380**, 66 (1991).
14. I. I. K. Pauliny-Toth, A. Witzel, E. Preuss, *et al.*, Astron. J. **83**, 451 (1978).
15. R. A. Perley, Astron. J. **87**, 859 (1982).
16. A. J. Pica, J. T. Pollock, A. G. Smith, *et al.*, Astron. J. **85**, 1442 (1980).
17. A. G. Polatidis, P. N. Wilkinson, W. Xu, *et al.*, Astrophys. J., Suppl. Ser. **98**, 1 (1995).
18. E. Salonen, H. Terasranta, S. Urpo, *et al.*, Astron. Astrophys., Suppl. Ser. **70**, 409 (1987).
19. P. R. Schwartz and J. A. Waak, Astron. J. **83**, 683 (1978).
20. M. Simard-Normandin and P. P. Kronberg, Astron. J. **83**, 1374 (1978).
21. H. Terasranta, M. Tornikoski, E. Valtaoja, *et al.*, Astron. Astrophys., Suppl. Ser. **94**, 121 (1992).
22. H. Terasranta, M. Tornikoski, A. Mujunen, *et al.*, Astron. Astrophys., Suppl. Ser. **132**, 305 (1998).
23. W. Xu, C. S. Readhead, T. J. Pearson, *et al.*, Astrophys. J., Suppl. Ser. **99**, 297 (1995).

Translated by G. Rudnitskii

Astronomy Letters, Vol. 28, No. 11, 2002, pp. 727–744. Translated from Pis'ma v Astronomicheskiĭ Zhurnal, Vol. 28, No. 11, 2002, pp. 809–828.
Original Russian Text Copyright © 2002 by Zheleznyakov, Koryagin.

Polarization Spectra of Synchrotron Radiation and the Plasma Composition of Relativistic Jets

V. V. Zheleznyakov[1,2] and **S. A. Koryagin**[1,2*]

[1]Institute of Applied Physics, Russian Academy of Sciences, ul. Ulyanova 46, Nizhni Novgorod, 603950 Russia
[2]Max-Planck-Institut für Astrophysik, Karl Schwarzschild Strasse 1, 85471 Garching bei München, Germany

Received May 29, 2002

Abstract—We investigate the problem of determining the plasma composition of relativistic jets in blazars and microquasars from the polarization frequency spectra of their synchrotron radiation. The effect of plasma composition on this radiation is attributable to a change in the structure of the ordinary and extraordinary waves in plasma, depending on the presence of a nonrelativistic electron–proton component in it and on the type of relativistic particles (electrons, positrons). The structure of the normal waves determines the properties of the observed radiation and primarily the shape of the polarization frequency spectrum. Our analytic calculations of the polarization spectra for simple models of jets with a uniform magnetic field and with a magnetic-field shear revealed characteristic features in the polarization spectra. These features allow us to differentiate between the synchrotron radiation from an admixture of relativistic particles in a cold plasma and the radiation from a relativistic plasma. However, definitive conclusions regarding the relativistic plasma composition (electrons or electron–positron pairs) can be reached only by a detailed analysis of the polarization frequency spectra that will be obtained in future radioastronomical studies with high angular and frequency resolutions. *© 2002 MAIK "Nauka/Interperiodica".*

Key words: *jet theory, active galactic nuclei, quasars and radio galaxies.*

1. INTRODUCTION

Here, we deal with the outstanding problem of the emitting-plasma composition in relativistic jets. These jets are observed over a wide frequency range among extragalactic sources—in blazars (i.e., active quasars in the radio frequency band and BL Lac objects) and in sources that belong to our Galaxy (in microquasars). An incoherent synchrotron mechanism attributable to the motion of relativistic particles in the jet magnetic field is generally believed to be responsible for the radio and optical radiation of the jets. Relativistic electrons in a nonrelativistic electron–proton plasma are commonly assumed to serve as these particles in cosmic radio sources. There is no such confidence in the case of jets, because the jet plasma is formed in the immediate vicinity of black holes and, in principle, can significantly change compared to the original plasma of accretion disks. In this case, one might expect the acceleration of the entire electron component to relativistic energies and the appearance of a positron component in the jet composition.

Attempts to detect the 0.5 MeV line in the jet spectrum attributable to the annihilation of nonrelativistic positrons and electrons have failed. At the same time, it is beyond reason to hope that the annihilation radiation can be detected from relativistic positrons whose frequency spectrum is blurred and lacks narrow spectral features.

However, the problem of whether there are relativistic electron plasma and relativistic positrons in jets can be approached from a different perspective. The point is that a high number density of relativistic electrons and positrons can change the electrodynamic properties of the plasma and affect the polarization of the normal (ordinary and extraordinary) waves in a magnetoactive plasma and, thereby, change the pattern of the observed synchrotron radiation (primarily modify the polarization frequency spectrum of the jet-emitted radiation). The normal-wave polarization depends on the ratio of the number densities of a cold plasma, relativistic electrons, and relativistic positrons. Therefore, we consider the following four jet compositions:

(I) the relativistic electron (or positron) component in a nonrelativistic (cold) plasma;

(II) the relativistic electron–positron component in a cold plasma;

(III) the relativistic electron plasma (with protons to offset the electron charge);

(IV) the relativistic electron–positron plasma.

---

[*] E-mail: `koryagin@appl.sci-nnov.ru`

In the first two cases, the relativistic components are treated as a minor admixture to the cold plasma. In this case, the cold plasma forms the structure of the normal waves and the relativistic components serve as the source of synchrotron reabsorption and radiation. In the last two cases, the relativistic plasma performs both functions: it forms the structure of the normal waves and serves as the source of synchrotron radiation.

In the first three cases, the protons serve only to offset the electron charge (or the difference between the electron and positron charges) and they are assumed to be nonrelativistic. In principle, it may well be that the protons have relativistic energies. In that case, the energy transferred by the jet significantly increases. Electrodynamically, however, this case does not differ from the corresponding case with cold protons, because, being massive, they have virtually no effect on the polarization and dispersive properties of the normal waves. At the same time, the synchrotron radiation from the protons at those frequencies at which the electrons effectively radiate is relatively weak.

Below, our specific calculations are based on a simple model of synchrotron radiation (a jet) with a uniform spatial plasma distribution in a layer of linear size L along the line of sight, an isotropic particle momentum distribution (in the jet frame of reference), and a power-law energy spectrum of the emitting relativistic particles bounded below by energy $E_{\min} \gg mc^2$:

$$N(E) \propto \begin{cases} 0 & \text{for } E < E_{\min} \\ E^{-\gamma} & \text{for } E \geq E_{\min}, \end{cases} \tag{1.1}$$

where the spectral index $\gamma > 2$. The electron and positron energy spectra in cases II and IV are assumed to be identical. The frequency spectrum of the synchrotron radiation with significant reabsorption at low frequencies is

$$I(\omega) \propto \begin{cases} \omega^{5/2} & \text{for } \omega \ll \omega_{\max} \\ \omega^{-(\gamma-1)/2} & \text{for } \omega \gg \omega_{\max}, \end{cases} \tag{1.2}$$

where

$$\omega_{\max} \gg \omega_{\min} = (3/2)\omega_B \Gamma_{\min}^2 \sin\varphi.$$

Here, $\omega_B = eB/(mc)$ is the nonrelativistic electron gyrofrequency, B is the magnetic field oriented at angle φ to the propagation direction of the radiation, m is the electron rest mass, e is the elementary charge, c is the speed of light, and $\Gamma_{\min} = E_{\min}/(mc^2)$ is the Lorentz factor of the electrons with energy $E_{\min}$. At frequency $\omega_{\max}$, the intensity frequency spectrum reaches a maximum. This frequency is close to $\omega_{\tau=1}$, where the optical depth τ of the source related to the reabsorption of the synchrotron radiation is equal to unity. If $\tau \ll 1$ in the entire frequency range $\omega \gg \omega_{\min}$, then the intensity frequency spectrum is described by the second formula from (1.2) in this range and falls off toward low frequencies as $\omega^{1/3}$ at $\omega \ll \omega_{\min}$. The magnetic field $\mathbf{B}$ in the jet is assumed to be constant along the line $\mathbf{n}$, except for case IV, where we consider a magnetic-field shear—the change in the orientation of the $\mathbf{B}$ projection onto the plane orthogonal to the line-of-sight $\mathbf{n}$.

2. THE METHOD FOR CALCULATING THE POLARIZATION OF THE RADIATION FROM A SYNCHROTRON SOURCE

In a magnetoactive plasma at high frequencies,

$$\omega \gg \omega_{\min} \gg \omega_B, \quad \omega \gg \omega_{\mathrm{L}} \tag{2.1}$$

the permittivity tensor approaches a unit tensor and the normal waves become transverse. The Langmuir frequency ω_{L} in (2.1) determines the isotropic part of the permittivity tensor $\varepsilon_0 = 1 - \omega_{\mathrm{L}}^2/\omega^2$. In this case, the polarization vectors $\mathbf{e}_{\mathrm{e}}$ and $\mathbf{e}_{\mathrm{o}}$ of the extraordinary and ordinary normal waves, their absorption coefficients $\varkappa_{\mathrm{e}}$ and $\varkappa_{\mathrm{o}}$ in amplitude, and the difference $k_{\mathrm{o}} - k_{\mathrm{e}}$ between the wave numbers can be determined from the dispersion relation

$$\frac{\omega}{c}\sum_{\beta}[(\varepsilon_{\alpha\beta} - \varepsilon_0\delta_{\alpha\beta})e_{\mathrm{e}\beta}] = 2(k_{\mathrm{e}} - k_{\mathrm{i}} + i\varkappa_{\mathrm{e}})e_{\mathrm{e}\alpha},$$
$$\frac{\omega}{c}\sum_{\beta}[(\varepsilon_{\alpha\beta} - \varepsilon_0\delta_{\alpha\beta})e_{\mathrm{o}\beta}] = 2(k_{\mathrm{o}} - k_{\mathrm{i}} + i\varkappa_{\mathrm{o}})e_{\mathrm{o}\alpha} \tag{2.2}$$

(see, e.g., Sazonov 1969). Here, $k_{\mathrm{i}} = \sqrt{\varepsilon_0}\omega/c$ is the wave number of the normal waves in an isotropic (nonmagnetized) plasma; $e_{\mathrm{e}\alpha}$ and $e_{\mathrm{o}\alpha}$ are the components of the polarization vectors $\mathbf{e}_{\mathrm{e}}$ and $\mathbf{e}_{\mathrm{o}}$ along the x, y, z axes of a Cartesian coordinate system in which the z axis is directed along the ray $\mathbf{n}$ of radiation propagation; and the indices α and β run through the values of x and y. The tensor $\varepsilon_{\alpha\beta} - \varepsilon_0\delta_{\alpha\beta} \ll 1$, where $\delta_{\alpha\beta}$ is the Kronecker symbol, describes the deviation of the permittivity tensor $\varepsilon_{\alpha\beta}$ from an isotropic tensor.

To simplify the formulas, it is convenient to direct the y axis along the magnetic-field projection onto the xy picture plane. In this coordinate system, the tensor

$$\frac{\omega}{c}(\varepsilon_{\alpha\beta} - \varepsilon_0\delta_{\alpha\beta}) = \begin{pmatrix} h & if \\ -if & -h \end{pmatrix} + i\begin{pmatrix} \mu+\lambda & 0 \\ 0 & \mu-\lambda \end{pmatrix}, \tag{2.3}$$

where the first and second terms describe the Hermitian and anti-Hermitian parts of the tensor $\omega(\varepsilon_{\alpha\beta} -$

$\varepsilon_0\delta_{\alpha\beta})/c$, respectively. The nondiagonal elements of the anti-Hermitian part are ignored in formula (2.3), because they are much smaller than μ and λ in the diagonal elements.[1] The coefficients h, f, μ, and λ for $\gamma > 2$ appear as follows (Sazonov 1969):

$$h = h_\mathrm{c} + h_\mathrm{rel}, \quad f = f_\mathrm{c} + f_\mathrm{rel}, \tag{2.4}$$

$$h_\mathrm{c} = -\frac{4\pi e^2}{mc\omega}\left(\frac{\omega_B \sin\varphi}{\omega}\right)^2 \frac{n_\mathrm{c}}{2},$$

$$f_\mathrm{c} = \frac{4\pi e^2}{mc\omega}\frac{\omega_B \sin\varphi}{\omega} n_\mathrm{c}\cot\varphi,$$

$$h_\mathrm{rel} = -\frac{4\pi e^2}{mc\omega}\left(\frac{\omega_B \sin\varphi}{\omega}\right)^2 \frac{(\gamma-1)(n_- + n_+)\Gamma_\mathrm{min}}{\gamma-2},$$

$$f_\mathrm{rel} = \frac{4\pi e^2}{mc\omega}\frac{\omega_B \sin\varphi}{\omega}\frac{(\gamma-1)(n_- - n_+)\cot\varphi \ln\Gamma_\mathrm{min}}{(\gamma+1)\Gamma^2_\mathrm{min}},$$

$$\mu = \frac{4\pi e^2}{mc\omega}\left(\frac{\omega_B \sin\varphi}{\omega}\right)^{(\gamma+2)/2}\frac{3^{\gamma/2}}{a(\gamma)}(\gamma-1) \times (n_- + n_+)\Gamma^{\gamma-1}_\mathrm{min},$$

$$\lambda = \frac{4\pi e^2}{mc\omega}\left(\frac{\omega_B \sin\varphi}{\omega}\right)^{(\gamma+2)/2}\frac{3\gamma+6}{3\gamma+10}\frac{3^{\gamma/2}}{a(\gamma)} \times (\gamma-1)(n_- + n_+)\Gamma^{\gamma-1}_\mathrm{min},$$

where h_c, f_c and h_rel, f_rel describe the contributions of the cold and relativistic plasma components to the coefficients h and f^2; n_c is the number density of the cold electrons; n_- and n_+ are the number densities of the relativistic electrons and positrons, respectively; and the factor

$$a(\gamma) = \frac{8}{\sqrt{3}\Gamma\left(\frac{3\gamma+2}{12}\right)\Gamma\left(\frac{3\gamma+22}{12}\right)} \sim 3. \tag{2.5}$$

It follows from expressions (2.4) that in our case of a power-law distribution (1.1) of relativistic particles and high frequencies (2.1), the anti-Hermitian part of the tensor (2.3) is much smaller than its Hermitian part for any plasma composition: $\mu \ll h_\mathrm{rel} < h$, $\lambda \ll h_\mathrm{rel} < h$. Taking this circumstance into account, we obtain from the dispersion relation (2.2)

$$k_\mathrm{o} - k_\mathrm{e} = \sqrt{h^2 + f^2}, \quad 2\varkappa_\mathrm{e} = \mu[1 + \rho^\varkappa \cos(2\sigma)], \tag{2.6}$$

$$2\varkappa_\mathrm{o} = \mu[1 - \rho^\varkappa \cos(2\sigma)];$$

$$e_{\mathrm{e}x} = \cos\sigma, \quad e_{\mathrm{e}y} = i\sin\sigma, \tag{2.7}$$

$$e_{\mathrm{o}x} = i\sin\sigma, \quad e_{\mathrm{o}y} = \cos\sigma;$$

where the angle σ determines the shape of the polarization ellipses for the normal waves and is specified by the equalities

$$\cos(2\sigma) = \frac{-h}{\sqrt{h^2+f^2}}, \quad \sin(2\sigma) = \frac{f}{\sqrt{h^2+f^2}}, \tag{2.8}$$

and the parameter

$$\rho^\varkappa \equiv \frac{\lambda}{\mu} = \frac{3\gamma+6}{3\gamma+10} \tag{2.9}$$

characterizes the difference between the absorption coefficients of the extraordinary and ordinary waves. For linearly polarized normal waves, when $\sigma = 0$, $\rho^\varkappa = (\varkappa_\mathrm{e} - \varkappa_\mathrm{o})/(\varkappa_\mathrm{e} + \varkappa_\mathrm{o})$. Since the polarization vectors (2.7) in our approximation are determined only by the Hermitian part of the tensor (2.3), they are mutually orthogonal. The slight nonorthogonality results from the difference between the absorption coefficients of the ordinary and extraordinary waves ($\rho^\varkappa \neq 0$) and is disregarded here.

The polarization of the radiation emerging from the jet is determined by the solution to the transfer equation (Zheleznyakov 1968, 1997)

$$\frac{\mathrm{d}I_{\alpha\beta}}{\mathrm{d}z} = P_{\alpha\beta} + \sum_{\alpha',\beta'}[(R_{\alpha\beta\alpha'\beta'} - K_{\alpha\beta\alpha'\beta'})I_{\alpha'\beta'}] \tag{2.10}$$

for the radiation polarization tensor $I_{\alpha\beta}$. The latter is related to the Stokes parameters I, Q, U, and V by

$$I = I_{xx} + I_{yy}, \quad Q = I_{xx} - I_{yy}, \tag{2.11}$$
$$U = I_{yx} + I_{xy}, \quad V = i(I_{yx} - I_{xy}).$$

The emissivity tensor of the medium $P_{\alpha\beta}$ is related to the total emissivity of the two normal waves

$$P = \frac{e^2\omega}{8\pi^2 c}\left(\frac{\omega_B \sin\varphi}{\omega}\right)^{(\gamma+1)/2}\frac{3^{\gamma/2}}{\gamma+1}\Gamma\left(\frac{3\gamma-1}{12}\right) \times \Gamma\left(\frac{3\gamma+19}{12}\right)(\gamma-1)(n_- + n_+)\Gamma^{\gamma-1}_\mathrm{min}$$

by the relations

$$P_{xx} = \frac{1+\rho^S}{2}P, \quad P_{yy} = \frac{1-\rho^S}{2}P, \tag{2.12}$$
$$P_{xy} = P_{yx} = 0,$$

where the degree of linear polarization of the sources is

$$\rho^S = \frac{3\gamma+3}{3\gamma+7}. \tag{2.13}$$

The zero nondiagonal elements of the tensor $P_{\alpha\beta}$ imply that we ignore the weak circular polarization

---

[1] This relationship between the diagonal and nondiagonal elements is retained as long as the electron momentum distribution is slightly anisotropic on the scale of the synchrotron radiation beam for a single particle.

[2] If $\gamma < 2$, then h_rel has a different frequency dependence (see Sazonov 1969). This case requires a special analysis.

of the sources [it is $\Gamma_{\min}^{-1}(\omega_{\min}/\omega)^{1/2}\cot\varphi$ in order of magnitude]. The tensors $R_{\alpha\beta\alpha'\beta'}$ and $K_{\alpha\beta\alpha'\beta'}$ are

$$R_{\alpha\beta\alpha'\beta'} = i(k_{\mathrm{e}} - k_{\mathrm{o}})(e_{\mathrm{e}\alpha}e^{*}_{\mathrm{o}\beta}e^{*}_{\mathrm{e}\alpha'}e_{\mathrm{o}\beta'} - e_{\mathrm{o}\alpha}e^{*}_{\mathrm{e}\beta}e^{*}_{\mathrm{o}\alpha'}e_{\mathrm{e}\beta'}), \tag{2.14}$$

$$K_{\alpha\beta\alpha'\beta'} = (\varkappa_{\mathrm{e}}+\varkappa_{\mathrm{o}})(e_{\mathrm{e}\alpha}e^{*}_{\mathrm{o}\beta}e^{*}_{\mathrm{e}\alpha'}e_{\mathrm{o}\beta'} + e_{\mathrm{o}\alpha}e^{*}_{\mathrm{e}\beta}e^{*}_{\mathrm{o}\alpha'}e_{\mathrm{e}\beta'}) + 2\varkappa_{\mathrm{e}}e_{\mathrm{e}\alpha}e^{*}_{\mathrm{e}\beta}e^{*}_{\mathrm{e}\alpha'}e_{\mathrm{e}\beta'} + 2\varkappa_{\mathrm{o}}e_{\mathrm{o}\alpha}e^{*}_{\mathrm{o}\beta}e^{*}_{\mathrm{o}\alpha'}e_{\mathrm{o}\beta'},$$

where the asterisk denotes a complex conjugate.[3]

The solutions to Eq. (2.10) in the limiting cases of circularly and linearly polarized normal waves were obtained by Zheleznyakov (1968) and Pacholczyk and Swihart (1970) (see also Zheleznyakov 1997). The solution of Eq. (2.10) in the general case of elliptically polarized normal waves is required to analyze the polarization of the emergent radiation. For a spatially homogeneous source, the tensors $P_{\alpha\beta}$, $R_{\alpha\beta\alpha'\beta'}$, and $K_{\alpha\beta\alpha'\beta'}$ do not depend on the z coordinate and the solution to Eq. (2.10) takes the form

$$\begin{aligned} I_{\alpha\beta} = \sum_{\alpha',\beta'} \Bigg\{ & e_{\mathrm{e}\alpha}e^{*}_{\mathrm{e}\beta}e^{*}_{\mathrm{e}\alpha'}e_{\mathrm{e}\beta'}P_{\alpha'\beta'}\frac{1-\exp(-2\varkappa_{\mathrm{e}}z)}{2\varkappa_{\mathrm{e}}} \\ & + e_{\mathrm{o}\alpha}e^{*}_{\mathrm{o}\beta}e^{*}_{\mathrm{o}\alpha'}e_{\mathrm{o}\beta'}P_{\alpha'\beta'}\frac{1-\exp(-2\varkappa_{\mathrm{o}}z)}{2\varkappa_{\mathrm{o}}} \\ & + e_{\mathrm{e}\alpha}e^{*}_{\mathrm{o}\beta}e^{*}_{\mathrm{e}\alpha'}e_{\mathrm{o}\beta'}P_{\alpha'\beta'} \times \frac{1-\exp[-(\varkappa_{\mathrm{e}}+\varkappa_{\mathrm{o}})z + i(k_{\mathrm{e}}-k_{\mathrm{o}})z]}{\varkappa_{\mathrm{e}}+\varkappa_{\mathrm{o}} - i(k_{\mathrm{e}}-k_{\mathrm{o}})} \\ & + e_{\mathrm{o}\alpha}e^{*}_{\mathrm{e}\beta}e^{*}_{\mathrm{o}\alpha'}e_{\mathrm{e}\beta'}P_{\alpha'\beta'} \times \frac{1-\exp[-(\varkappa_{\mathrm{e}}+\varkappa_{\mathrm{o}})z - i(k_{\mathrm{e}}-k_{\mathrm{o}})z]}{\varkappa_{\mathrm{e}}+\varkappa_{\mathrm{o}} + i(k_{\mathrm{e}}-k_{\mathrm{o}})} \Bigg\}. \end{aligned} \tag{2.15}$$

In formula (2.15), we assume that the z coordinate is measured from the ray base in the source and that no external radiation falls on the source.

We determine the Stokes parameters (2.11) of the emergent radiation (at point $z = L$, where L is the ray length in the source) from (2.15) and expressions (2.7) and (2.12) for the polarization vectors and the emissivity tensor:

$$I = PL\Bigg(\frac{1+\rho^{S}\cos(2\sigma)}{2}\,\frac{1-\exp(-\tau_{\mathrm{e}})}{\tau_{\mathrm{e}}} + \frac{1-\rho^{S}\cos(2\sigma)}{2}\,\frac{1-\exp(-\tau_{\mathrm{o}})}{\tau_{\mathrm{o}}}\Bigg), \tag{2.16}$$

$$\begin{aligned} Q = PL\Bigg(& \cos(2\sigma)\frac{1+\rho^{S}\cos(2\sigma)}{2} \times \frac{1-\exp(-\tau_{\mathrm{e}})}{\tau_{\mathrm{e}}} - \cos(2\sigma)\frac{1-\rho^{S}\cos(2\sigma)}{2} \\ & \times \frac{1-\exp(-\tau_{\mathrm{o}})}{\tau_{\mathrm{o}}} + \rho^{S}\sin^{2}(2\sigma)\exp(-\tau) \times \frac{\tau(\exp\tau - \cos\phi) + \phi\sin\phi}{\tau^{2}+\phi^{2}}\Bigg), \end{aligned} \tag{2.17}$$

$$U = PL\rho^{S}\sin(2\sigma)\exp(-\tau)\frac{\phi(\exp\tau - \cos\phi) - \tau\sin\phi}{\tau^{2}+\phi^{2}}, \tag{2.18}$$

$$\begin{aligned} V = PL\Bigg(& -\sin(2\sigma)\frac{1+\rho^{S}\cos(2\sigma)}{2} \times \frac{1-\exp(-\tau_{\mathrm{e}})}{\tau_{\mathrm{e}}} + \sin(2\sigma)\frac{1-\rho^{S}\cos(2\sigma)}{2} \\ & \times \frac{1-\exp(-\tau_{\mathrm{o}})}{\tau_{\mathrm{o}}} + \rho^{S}\sin(2\sigma)\cos(2\sigma)\exp(-\tau) \times \frac{\tau(\exp\tau - \cos\phi) + \phi\sin\phi}{\tau^{2}+\phi^{2}}\Bigg). \end{aligned} \tag{2.19}$$

In (2.16)–(2.19), we use the following notation: $\tau_{\mathrm{e}} = [1 + \rho^{\varkappa}\cos(2\sigma)]\tau$ and $\tau_{\mathrm{o}} = [1 - \rho^{\varkappa}\cos(2\sigma)]\tau$ are the optical depths of the layer for the extraordinary and ordinary waves, $\tau = (\varkappa_{\mathrm{e}} + \varkappa_{\mathrm{o}})L$ is the mean optical depth for the two types of waves ($\tau = (\tau_{\mathrm{e}} + \tau_{\mathrm{o}})/2$), and

$$\phi = (k_{\mathrm{o}} - k_{\mathrm{e}})L = \sqrt{h^{2}+f^{2}}L \tag{2.20}$$

is the phase difference between the ordinary and extraordinary waves acquired on the layer length L [see (2.6)]. Formulas (2.16)–(2.19) transform into the corresponding expressions derived by Zheleznyakov (1968) and Pacholczyk and Swihart (1970) for circularly ($\sigma = \pi/4$) and linearly ($\sigma = 0$) polarized normal waves.

Formulas (2.16)–(2.19) simplify in the range of high frequencies under consideration ($\omega \gg \omega_{\min}$), because the phase difference ϕ significantly exceeds the optical depth τ of the layer [this is because the anti-Hermitian part of the tensor (2.3) is small compared to its Hermitian part: $\phi = \sqrt{h^{2}+f^{2}}L \gg \mu L = \tau$]. This circumstance allows the parameter τ to be retained only in the exponents in (2.18) and in

---

[3] The transfer equation (2.10) with the tensors (2.12) and (2.14) is valid for orthogonally polarized normal waves. The corresponding transfer equation that includes the nonorthogonality of the normal waves with a weak anisotropy of the permittivity tensor was derived by Sazonov and Tsytovich (1968). In the latter case, the solution is more complex (see Pacholczyk and Swihart (1975); Jones and O'Dell (1977a)) than the solution to Eq. (2.10). At the same time, in our case of a power-law particle distribution (1.1) and high frequencies (2.1), the effects related to the nonorthogonality of the normal waves introduce relatively small corrections to the solution and, hence, are marginal.

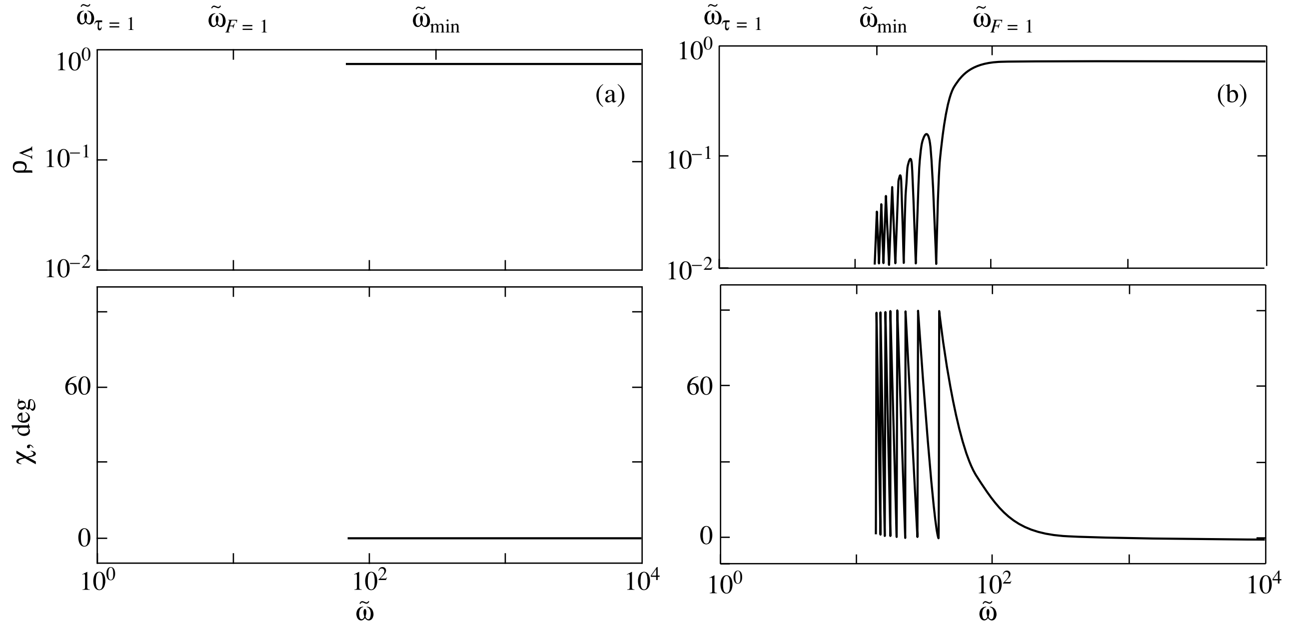

Fig. 1. The polarization spectra of the synchrotron radiation from a source with cold plasma and with an admixture of relativistic electrons and positrons: (a) case A for $\gamma = 3$, $\Gamma_{\min} = 10^2$, $\varphi = 45°$, $n_c/(n_- + n_+) = 10^4$, $F_0 = 10^2$; (b) case B for $\gamma = 3$, $\Gamma_{\min} = 10^2$, $\varphi = 45°$, $n_c/(n_- + n_+) = 10^4$, $F_0 = 10^4$.

the third terms of (2.17)–(2.19):[4]

$$Q = PL\left(\cos(2\sigma)\frac{1+\rho^S\cos(2\sigma)}{2} \times \frac{1-\exp(-\tau_e)}{\tau_e} - \cos(2\sigma)\frac{1-\rho^S\cos(2\sigma)}{2} \times \frac{1-\exp(-\tau_o)}{\tau_o} + \rho^S\sin^2(2\sigma)\exp(-\tau)\frac{\sin\phi}{\phi}\right), \tag{2.21}$$

$$U = PL\rho^S\sin(2\sigma)\frac{1-\exp(-\tau)\cos\phi}{\phi}, \tag{2.22}$$

$$V = PL\left(-\sin(2\sigma)\frac{1+\rho^S\cos(2\sigma)}{2} \times \frac{1-\exp(-\tau_e)}{\tau_e} + \sin(2\sigma)\frac{1-\rho^S\cos(2\sigma)}{2} \times \frac{1-\exp(-\tau_o)}{\tau_o} + \rho^S\sin(2\sigma)\cos(2\sigma)\exp(-\tau)\frac{\sin\phi}{\phi}\right). \tag{2.23}$$

Our subsequent analysis of the polarization frequency spectrum is based on expressions (2.16) and (2.21)–(2.23), which are convenient to reduce to a dimensionless form. To this end, we normalize ω to the frequency

$$\omega_{\tau=1} = \omega_B\sin\varphi \times \left[\frac{4\pi e^2 L}{mc\omega_B\sin\varphi}\frac{3^{\gamma/2}}{a(\gamma)}(\gamma-1)(n_- + n_+)\Gamma_{\min}^{\gamma-1}\right]^{2/(\gamma+4)}, \tag{2.24}$$

at which the optical depth of the layer $\tau = 1$. We denote the dimensionless frequency $\omega/\omega_{\tau=1}$ by $\tilde{\omega}$. With this normalization, the frequency dependence of the optical depth assumes a simple form:

$$\tau = \tilde{\omega}^{-(\gamma+4)/2}. \tag{2.25}$$

Recall that near the frequency $\omega_{\tau=1} \sim \omega_{\max}$, a maximum is formed in the intensity frequency spectrum of the synchrotron radiation from the layer [see (1.2)].

To characterize the radiation polarization, it will suffice to know the Q/I, U/I, and V/I ratios. These quantities define the degrees of linear and circular polarization of the radiation (Zheleznyakov 1997),

$$\rho_\Lambda = \sqrt{(Q/I)^2 + (U/I)^2}, \quad \rho_\kappa = V/I,$$

and the angle χ between the major axis of the polarization ellipse and the x axis:

$$\cos(2\chi) = \frac{Q/I}{\sqrt{(Q/I)^2 + (U/I)^2}},$$

$$\sin(2\chi) = \frac{U/I}{\sqrt{(Q/I)^2 + (U/I)^2}}.$$

While analyzing formulas (2.16) and (2.21)–(2.23) as well as expressions (2.8) and (2.20) for the functions $\cos(2\sigma)$, $\sin(2\sigma)$, and ϕ, it can be noticed

---

[4] Note that in expressions (2.7), we have already discarded the terms of the order of $\lambda/\max[h, f] \sim \tau/\phi$ that define weak nonorthogonality of the polarization vectors.

that Q/I, U/I, and V/I are determined mainly by two functions of the frequency:

$$H \equiv -hL = \frac{H_0}{\tilde{\omega}^3}, \quad F \equiv fL = \frac{F_0}{\tilde{\omega}^2}. \qquad (2.26)$$

The latter, in turn, are specified by the parameters H_0 and F_0, the values of H and F at the frequency $\tilde{\omega}_{\tau=1} = 1$. Indeed, the parameters $\cos(2\sigma)$, $\sin(2\sigma)$, and ϕ appearing in expressions (2.16) and (2.21)–(2.23) can be rewritten as

$$\cos(2\sigma) = \frac{H}{\sqrt{H^2+F^2}}, \qquad (2.27)$$

$$\sin(2\sigma) = \frac{F}{\sqrt{H^2+F^2}}, \quad \phi = \sqrt{H^2+F^2}.$$

The quantities Q/I, U/I, and V/I also depend on the parameters $\rho^{\varkappa}(\gamma)$ and $\rho^S(\gamma)$, but they vary only slightly—they remain of the order of unity when γ is varied over the range $2 < \gamma < \infty$ [see (2.9) and (2.13)]. The parameters H_0 and F_0 specify the phase difference $\phi = \sqrt{H_0^2+F_0^2}$ and the shape of the polarization ellipses for the normal waves (via the angle σ) at the selected frequency $\omega_{\tau=1}$. Below, for definiteness, we assume that the ray $\mathbf{n}$ makes an acute angle φ with the direction of the magnetic field $\mathbf{B}$. In this case, H_0, F_0, and $\cot\varphi$ are positive.

We analyze the polarization frequency spectra for various plasma compositions for fixed parameters $\Gamma_{\min}$ and γ of the relativistic-particle energy distribution and for a fixed direction of propagation of the radiation relative to the magnetic field (angle φ). In that case, H_0 and F_0 are related by

$$\frac{H_0}{F_0^{(\gamma-2)/\gamma}} = \frac{(1/3)a^{2/\gamma}(\gamma)(\cot\varphi)^{-(\gamma-2)/\gamma}\left[\dfrac{n_\mathrm{c}}{2\Gamma_{\min}} + \dfrac{\gamma-1}{\gamma-2}(n_- + n_+)\right]}{[(\gamma-1)(n_- + n_+)]^{2/\gamma}\left[n_\mathrm{c}\Gamma_{\min} + \dfrac{\gamma-1}{\gamma+1}(n_- - n_+)\dfrac{\ln\Gamma_{\min}}{\Gamma_{\min}}\right]^{(\gamma-2)/\gamma}}. \qquad (2.28)$$

The latter can be established if it is considered that

$$H_0 \propto L/\omega_{\tau=1}^3 \propto L^{(\gamma-2)/(\gamma+4)}, \qquad (2.29)$$
$$F_0 \propto L/\omega_{\tau=1}^2 \propto L^{\gamma/(\gamma+4)}.$$

Thus, it follows from our discussion that the polarization frequency spectrum can be unambiguously determined if we fix the plasma composition, the parameters of the relativistic particle energy distribution, and the angle φ and specify one of the parameters, F_0 or H_0. In this case, an increase in F_0 and H_0 corresponds to an increase in the layer length L for $\gamma > 2$.

It should be emphasized that the above formulas for calculating the polarization spectrum are valid at $\omega \gg \omega_{\min}$. The expression for $\omega_{\min}$ in dimensionless form is

$$\tilde{\omega}_{\min} \equiv \frac{\omega_{\min}}{\omega_{\tau=1}} = \frac{1}{2} \qquad (2.30)$$
$$\times \left(\frac{a(\gamma)\cot\varphi\left[n_\mathrm{c}\Gamma_{\min} + \frac{\gamma-1}{\gamma+1}(n_- - n_+)\frac{\ln\Gamma_{\min}}{\Gamma_{\min}}\right]}{(\gamma-1)(n_- + n_+)F_0}\right)^{2/\gamma}.$$

The solution (2.16), (2.21)–(2.23) describes the radiation polarization in a frame of reference where the jet plasma is static. Since the jet matter moves relative to the observer with (generally relativistic) velocity $\mathbf{v}_\mathrm{j}$, the spectrum (2.16), (2.21)–(2.23) should be recalculated from the jet frame to the observer's frame. The radiation frequencies ω and ω_obs in the jet and observer's frames are related by the Doppler transformation

$$\omega = \omega_\mathrm{obs}\frac{1-(v_\mathrm{j}/c)\cos\Theta_\mathrm{obs}}{\sqrt{1-v_\mathrm{j}^2/c^2}}, \qquad (2.31)$$

where Θ_obs is the angle between the propagation direction $\mathbf{n}_\mathrm{obs}$ of the radiation in the observer's frame of reference and the velocity $\mathbf{v}_\mathrm{j}$. The propagation direction $\mathbf{n}$ of the radiation in the jet frame of reference lies in the same plane with the vectors $\mathbf{n}_\mathrm{obs}$ and $\mathbf{v}_\mathrm{j}$ and makes an angle Θ with the direction $\mathbf{v}_\mathrm{j}$, which is determined by the aberration law

$$\cos\Theta = \frac{\cos\Theta_\mathrm{obs} - v_\mathrm{j}/c}{1-(v_\mathrm{j}/c)\cos\Theta_\mathrm{obs}}. \qquad (2.32)$$

The degrees of linear and circular polarization (ρ_Λ and ρ_κ) are invariant relative to the transformation from one frame to the other (see Landau and Lifshitz 1988). The angle χ is also conserved if it is measured from the axis perpendicular to the plane of vectors $\mathbf{n}$, $\mathbf{n}_\mathrm{obs}$, and $\mathbf{v}_\mathrm{j}$ in both frames.

Since ρ_Λ, ρ_κ, and χ are invariant, it will suffice to calculate them only in the jet frame. The polarization frequency spectra in the two frames differ only by the proportional extension along the frequency axis attributable to the Doppler effect (2.31) and by the change in the direction of propagation in accordance with the aberration law (2.32). Therefore, if the frequency in both frames is normalized, for example, to the frequency of the spectral intensity maximum, then the shape of the frequency spectra for ρ_Λ, ρ_κ, and χ does not change when changing the frame.

3. A COLD PLASMA WITH AN ADMIXTURE OF RELATIVISTIC ELECTRONS AND POSITRONS

In our model with an isotropic momentum distribution of relativistic particles, where the polarization of the synchrotron sources in the jet is almost linear, the polarization frequency spectra for cases I and II are indistinguishable. Indeed, in this approximation, the emissivity tensors $P_{\alpha\beta}$ for relativistic electrons and positrons are identical (for identical particle energy distributions). At the same time, a minor admixture of relativistic particles (irrespective of their composition) in cases I and II does not affect the normal-wave polarization, which is specified by the cold plasma.

The latter suggestion implies that the Hermitian part of the tensor (2.3) is attributable mainly to the cold plasma component: $h_{\mathrm{rel}} \ll h_{\mathrm{c}}$ and $f_{\mathrm{rel}} \ll f_{\mathrm{c}}$. These inequalities impose the following constraints on the number density of the relativistic component:

$$2(n_- + n_+)\Gamma_{\min} \ll n_{\mathrm{c}}, \qquad \frac{(n_- - n_+)\ln\Gamma_{\min}}{\Gamma_{\min}^2} \ll n_{\mathrm{c}}, \tag{3.1}$$

which determine the realization of cases I and II.

The normal waves in a cold electron–proton plasma at frequencies (2.1) are known (Zheleznyakov 1997) to be circularly polarized over a wide range of angles φ specified by the condition

$$\tan^2\varphi \ll \frac{4\omega^2}{\omega_B^2 \sin^2\varphi}.$$

In this case of the so-called quasi-longitudinal propagation ($\sigma \approx \pi/4$), H_0 may be ignored compared to F_0 [see (2.26) and (2.27)].

Let us separate out the characteristic polarization spectra of the emergent synchrotron radiation as a function of F_0.

(A) The limit $F_0 \to 0$ corresponds to an infinitely thin layer, where the phase difference $\phi \approx F_0/\tilde{\omega}^2$ in the layer, let alone its optical depth $\tau \ll \phi$, are much smaller than unity at frequencies

$$\tilde{\omega} > \tilde{\omega}_{\min} \approx \frac{F_0^{-2/\gamma}}{2}\left(\frac{a(\gamma)}{\gamma-1}\right)^{2/\gamma}\left(\frac{n_{\mathrm{c}}\Gamma_{\min}\cot\varphi}{n_- + n_+}\right)^{2/\gamma}.$$

The following values correspond to this limit:

$$F_0 \ll 2^{-2\gamma/(\gamma+4)}\left(\frac{a(\gamma)}{\gamma-1}\right)^{4/(\gamma+4)} \tag{3.2}$$
$$\times\left(\frac{n_{\mathrm{c}}\Gamma_{\min}\cot\varphi}{n_- + n_+}\right)^{4/(\gamma+4)}.$$

Under condition (3.2), the normal-wave characteristics do not affect the polarization of the radiation emerging from the jet, which is identical to the polarization of the radiation from an assembly of relativistic particles (electrons, positrons) in a vacuum. The emergent radiation is linearly polarized, with the polarization plane being perpendicular to the magnetic-field projection onto the picture plane (see Fig. 1a):

$$\rho_\Lambda = Q{-}I = \rho^S, \quad U{-}I = 0, \quad \chi = 0, \tag{3.3}$$
$$\rho_\kappa = V{-}I = 0.$$

(B) As F_0 increases to

$$F_0 \gg 2^{-2\gamma/(\gamma+4)}\left(\frac{a(\gamma)}{\gamma-1}\right)^{4/(\gamma+4)} \tag{3.4}$$
$$\times\left(\frac{n_{\mathrm{c}}\Gamma_{\min}\cot\varphi}{n_- + n_+}\right)^{4/(\gamma+4)} \gg 1$$

the following frequency band appears in the range $\tilde{\omega} > \tilde{\omega}_{\min}$:

$$\tilde{\omega}_{\min} < \tilde{\omega} \lesssim \tilde{\omega}_{F=1} = F_0^{1/2}, \tag{3.5}$$

where $F \gtrsim 1$. The Faraday rotation of the polarization plane of the radiation as it propagates in the jet becomes significant here. At frequencies (3.5), the emergent radiation remains linearly polarized, but the degree and plane of linear polarization rapidly vary (oscillate) with frequency:

$$\frac{Q}{I} = \rho^S\frac{\sin F}{F}, \quad \frac{U}{I} = \rho^S\frac{1-\cos F}{F}, \tag{3.6}$$
$$\rho_\Lambda = \rho^S\left|\frac{\sin(F/2)}{F/2}\right|, \quad \chi = \frac{\pi}{2}\left\{\frac{F}{2\pi}\right\}, \quad \rho_\kappa = \frac{V}{I} = 0.$$

The curly brackets in formula (3.6) denote the fractional part of the number $F/(2\pi)$. The angle χ, which specifies the linear polarization plane, varies over a limited range, from 0 to $\pi/2$.

At sufficiently low frequencies ($\tilde{\omega} \ll \tilde{\omega}_{F\,=\,1}$), averaging the Stokes parameters (3.6) over rapid oscillations yields

$$\frac{\langle Q\rangle}{I} = 0, \quad \frac{\langle U\rangle}{I} = \frac{\rho^S}{F} \propto \tilde{\omega}^2, \quad \frac{\langle V\rangle}{I} = 0. \tag{3.7}$$

According to (3.7), the radiation at these frequencies is, on average, polarized at angle $\chi = \pi/4$ and the degree of polarization is proportional to $\tilde{\omega}^2$.

At frequencies $\tilde{\omega} \gg \tilde{\omega}_{F\,=\,1}$, the Faraday rotation becomes negligible ($F \ll 1$), the polarization ceases to oscillate, and its degree approaches ρ^S. In this frequency range, formulas (3.3) for an infinitely thin layer again become valid. The polarization frequency spectrum for this case is shown in Fig. 1b.

(C) If F_0 increases to even larger values,

$$F_0 \gg 2^{-2\gamma/(\gamma+4)} \left(\frac{a(\gamma)}{\gamma-1}\right)^{4/(\gamma+4)} \left(\frac{\Gamma_{\min}}{\cot\varphi}\right)^{\gamma/(\gamma+4)} \tag{3.8}$$
$$\times \left(\frac{n_{\rm c}\Gamma_{\min}\cot\varphi}{n_- + n_+}\right)^{4/(\gamma+4)},$$

then the mean degree of linear polarization

$$\left.\frac{\langle U\rangle}{I}\right|_{\tilde\omega_{\min}} = \frac{\rho^S}{4F_0^{(\gamma+4)/\gamma}} \left(\frac{a(\gamma)}{\gamma-1}\right)^{4/\gamma} \left(\frac{n_{\rm c}\Gamma_{\min}\cot\varphi}{n_- + n_+}\right)^{4/\gamma}$$

at $\tilde\omega_{\min}$ (where it is at a minimum) will drop below the degree of circular polarization of the sources in the jet. The latter implies that under the condition (3.8), our approximation of purely linear polarization of the sources breaks down at frequencies

$$\tilde\omega_{\min} < \tilde\omega \lesssim \tilde\omega_{\rm cr} = \frac{F_0^{2(\gamma-1)/(5\gamma)}}{2^{1/5}} \left(\frac{\Gamma_{\min}}{\cot\varphi}\right)^{-2/5} \tag{3.9}$$
$$\times \left(\frac{a(\gamma)}{\gamma-1}\right)^{2/(5\gamma)} \left(\frac{n_{\rm c}\Gamma_{\min}\cot\varphi}{n_- + n_+}\right)^{2/(5\gamma)}.$$

Here, the calculated degree of linear polarization of the emergent radiation $\rho_\Lambda = \rho^S\tilde\omega^2/F_0$ drops below the characteristic degree of circular polarization of the sources ρ_κ^S, which is estimated to be low,[5] of the order of $\Gamma_{\min}^{-1}(\tilde\omega_{\min}/\tilde\omega)^{1/2}\cot\varphi$. However, the polarization of the radiation emerging from the layer is described by formulas (3.6) and (3.7) at higher frequencies $\tilde\omega_{\rm cr} \lesssim \tilde\omega < \tilde\omega_{F=1}$ (where our approximation of $\rho_\kappa^S = 0$ for the polarization of the sources is valid) and by formulas (3.3) at even higher frequencies ($\tilde\omega \gg \tilde\omega_{F\,=\,1}$).

Note that if we used the approximation of purely linear polarization of the sources, then a further increase in F_0 in the range (3.8) would be accompanied by new qualitative changes in the polarization spectrum of the emergent synchrotron radiation at frequencies (3.9). However, the degree of polarization of the emergent radiation at frequencies (3.9) calculated in this way is lower than the degree of circular polarization of the sources ρ_κ^S over a wide range of angles $\pi/2 - \varphi \gtrsim \Gamma_{\min}^{-1/2}$.

In particular, the frequency of the spectral intensity maximum for the radiation $\tilde\omega_{\max} \sim \tilde\omega_{\tau=1}$ lies within the range (3.9). At these frequencies, one might expect an extremely low degree of polarization (less than $\Gamma_{\min}^{-1}\cot\varphi$), which is determined by a nonzero circular polarization of the synchrotron radiation sources.

Thus, in the case of a cold electron–proton plasma with an admixture of relativistic electrons and positrons, the following two characteristic polarization frequency spectra take place: the radiation spectrum of an infinitely thin layer under the condition (3.2) and the spectrum with strong depolarization and Faraday rotation of the polarization plane at frequencies $\tilde\omega \lesssim \tilde\omega_{F\,=\,1}$ under the condition (3.4). In this case, the frequency $\tilde\omega_{F\,=\,1}$ lies above the characteristic frequency $\tilde\omega_{\tau\,=\,1}$ of the spectral intensity maximum for the layer radiation.

4. A RELATIVISTIC ELECTRON PLASMA

In the case of a relativistic electron plasma (case III), both the synchrotron radiation and the dispersion parameters of the normal waves are determined by the relativistic particles, while the effect of the cold plasma is negligible: $h_{\rm rel} \gg h_{\rm c}$, $f_{\rm rel} \gg f_{\rm c}$. This requires that the relativistic-electron number density satisfies the condition

$$\frac{n_-\ln\Gamma_{\min}}{\Gamma_{\min}^2} \gg n_{\rm c}. \tag{4.1}$$

In this section, we discuss a relativistic plasma composed only of particles of the same type (electrons); a plasma composed of relativistic electron–positron pairs is considered in the next section.

Despite the simpler plasma composition, the emerging frequency dependence of the normal-wave polarization in case III makes it considerably more difficult to analyze the polarization frequency spectrum of the source. In this case, the normal waves at $\tilde\omega > \tilde\omega_{\min}$ can be polarized linearly, elliptically, and circularly over a wide range of $\mathbf{n}$ directions. The wave polarization is almost linear at low frequencies $\tilde\omega \ll \tilde\omega_{H\,=\,F}$, where $H \gg F$; it becomes elliptical near the frequency

$$\tilde\omega_{H=F} = \tilde\omega_{\min}\frac{2(\gamma+1)}{3(\gamma-2)}g(\Gamma_{\min},\varphi), \tag{4.2}$$
$$g(\Gamma_{\min},\varphi) = \frac{\Gamma_{\min}}{\cot\varphi\ln\Gamma_{\min}},$$

and transforms into circular at $\tilde\omega \gg \tilde\omega_{H=F}$, where $F \gg H$. In this case, the frequency range of linear polarization ($\tilde\omega \ll \tilde\omega_{H=F}$) falls within the frequency range under consideration, $\tilde\omega > \tilde\omega_{\min}$, if the $\mathbf{n}$ direction satisfies the condition $\tan\varphi \gg \Gamma_{\min}^{-1}\ln\Gamma_{\min}$. This requirement excludes from our analysis a narrow

---

[5] We ignore this polarization in our calculations. A weak circular polarization of the sources takes place if the relativistic component consists of electrons alone. If, however, the relativistic component is represented only by electron–positron pairs, then ρ_κ^S is exactly equal to zero and formulas (3.3), (3.6), and (3.7) also remain valid in most of the range (3.9), where the small deviation of the normal-wave polarization from circular polarization is insignificant ($H \ll 1$).

interval of angles φ in which the synchrotron radiation is also modified into relativistic dipole radiation (Zheleznyakov 1997).

Let us follow the change in the polarization spectrum of the synchrotron radiation emerging from the jet as the parameter F_0 is varied.

(A) At sufficiently low

$$F_0 \ll \frac{a(\gamma)}{2^{\gamma/2}(\gamma+1)g(\Gamma_{\min},\varphi)} \ll 1 \qquad (4.3)$$

the polarization spectrum (3.3) of the synchrotron radiation from an infinitely thin layer is realized, because the optical depth τ is much smaller than unity at $\tilde{\omega} > \tilde{\omega}_{\min}$:

$$\tilde{\omega}_{\tau=1} \ll \tilde{\omega}_{\min} = \frac{F_0^{-2/\gamma}}{2}\left(\frac{a(\gamma)}{(\gamma+1)g(\Gamma_{\min},\varphi)}\right)^{2/\gamma}.$$

At the same time, the parameters F and H are small:

$$F < \frac{F_0}{\tilde{\omega}_{\min}^2} \ll 1; \quad H < \frac{H_0}{\tilde{\omega}_{\min}^3} = \frac{8F_0^{(\gamma+4)/\gamma}}{3}$$
$$\times \frac{\gamma+1}{\gamma-2}\left(\frac{a(\gamma)}{\gamma+1}\right)^{-4/\gamma} g^{(\gamma+4)/\gamma} \ll 1.$$

The latter implies that the phase difference $\phi \ll 1$ and the polarization characteristics of the normal waves do not affect the radiation emerging from the jet.

(B) As F_0 increases to

$$\frac{a(\gamma)}{2^{\gamma/2}(\gamma+1)g(\Gamma_{\min},\varphi)} \ll F_0 \ll \left(\frac{\gamma+1}{3(\gamma-2)}\right)^{2\gamma/(\gamma+4)} \qquad (4.4)$$
$$\times \left(\frac{a(\gamma)}{\gamma+1}\right)^{4/(\gamma+4)} g^{2(\gamma-2)/(\gamma+4)}$$

at frequencies $\tilde{\omega} > \tilde{\omega}_{\min}$, an interval of strong reabsorption appears,

$$\tilde{\omega}_{\min} < \tilde{\omega} \ll \tilde{\omega}_{\tau=1}, \qquad (4.5)$$

where the layer optical depth $\tau \gg 1$. In this case, the normal waves in the range (4.5) are linearly polarized ($H \gg F$). Here, the effect of the difference between the absorption coefficients of the normal waves on the polarization spectrum of the emergent radiation becomes noticeable. This spectrum can be obtained from formulas (2.16) and (2.21)–(2.23) by passing to the limit $\tau \to \infty$ for $\cos(2\sigma) = 1$:

$$\rho_\Lambda = \frac{|Q|}{I} = \frac{|\rho^S - \rho^\varkappa|}{1 - \rho^\varkappa \rho^S} = \frac{3}{6\gamma+13}, \qquad (4.6)$$
$$U/I = 0, \quad \chi = \pi/2, \quad \rho_\kappa = V/I = 0.$$

The reabsorption coefficient of the extraordinary wave is large [$\rho^\varkappa > \rho^S$; see (2.9) and (2.13)], so the ordinary wave dominates in the emergent radiation. The latter is polarized along the magnetic-field projection onto the picture plane, i.e., perpendicular to the polarization plane of the emergent radiation at higher frequencies $\tilde{\omega} \gtrsim \tilde{\omega}_{\tau=1}$, where an extraordinary component dominates in the radiation.

It should be noted that the phase difference between the normal waves $\phi \approx H$ is larger than unity in a wider range,

$$\tilde{\omega}_{\min} < \tilde{\omega} < \tilde{\omega}_{H=1}, \qquad (4.7)$$

than (4.5). Its upper limit

$$\tilde{\omega}_{H=1} \equiv H_0^{1/3} = F_0^{(\gamma-2)/(3\gamma)}\left(\frac{\gamma+1}{3(\gamma-2)}\right)^{1/3} \qquad (4.8)$$
$$\times \left(\frac{a(\gamma)}{\gamma+1}\right)^{2/(3\gamma)} g^{(\gamma-2)/(3\gamma)}$$

is given by the equality $H(\tilde{\omega}_{H=1}) = 1$. The range (4.7) covers part of the range $\tilde{\omega} \gg \tilde{\omega}_{\min}$ where the reabsorption is weak. This relationship between the frequencies ($\tilde{\omega}_{\tau=1} < \tilde{\omega}_{H=1}$) stems from the fact that $H > \tau$ in a relativistic electron plasma at $\tilde{\omega} \gtrsim \tilde{\omega}_{\min}$.

At $\tilde{\omega} \gg \tilde{\omega}_{\tau=1}$, the absorption is negligible and the normal-wave polarization does not affect the spectrum of the emergent radiation as before. This is because at $\tilde{\omega} \ll \tilde{\omega}_{H=1}$, $F \ll H$ and the waves are linearly polarized, with the extraordinary wave being polarized in the same fashion as the radiation from the synchrotron sources in the jet. At higher frequencies, $\tilde{\omega} \gtrsim \tilde{\omega}_{H=F} \gg \tilde{\omega}_{H=1}$, the normal-wave polarization becomes circular, but the phase difference decreases to $\phi \ll 1$ and the change in the polarization pattern of the normal waves does not affect the polarization spectrum of the emergent radiation. Thus, under the condition (4.4), the polarization spectrum of the emergent radiation at frequencies above the spectral intensity maximum ($\tilde{\omega} \gg \tilde{\omega}_{\tau=1}$) corresponds to an infinitely thin layer and it is described by formulas (3.3) (see Fig. 2a).

(C) As F_0 increases further to

$$\left(\frac{\gamma+1}{3(\gamma-2)}\right)^{2\gamma/(\gamma+4)}\left(\frac{a(\gamma)}{\gamma+1}\right)^{4/(\gamma+4)} \qquad (4.9)$$
$$\times\, g^{2(\gamma-2)/(\gamma+4)} \ll F_0 \ll \left(\frac{\gamma+1}{3(\gamma-2)}\right)^{\gamma/2}\frac{a(\gamma)}{\gamma+1} g^{(\gamma-2)/2},$$

the frequency band

$$\tilde{\omega}_{H=F} \ll \tilde{\omega} \ll \tilde{\omega}_{F=1}, \qquad (4.10)$$

appears in the range of weak reabsorption ($\tilde{\omega} \gg \tilde{\omega}_{\tau=1}$) around the frequency $\tilde{\omega}_{H=1}$. The lower limit

$$\tilde{\omega}_{H=F} \equiv \frac{H_0}{F_0} = F_0^{-2/\gamma}\frac{\gamma+1}{3(\gamma-2)}\left(\frac{a(\gamma)}{\gamma+1}\right)^{2/\gamma} g^{(\gamma-2)/\gamma}$$

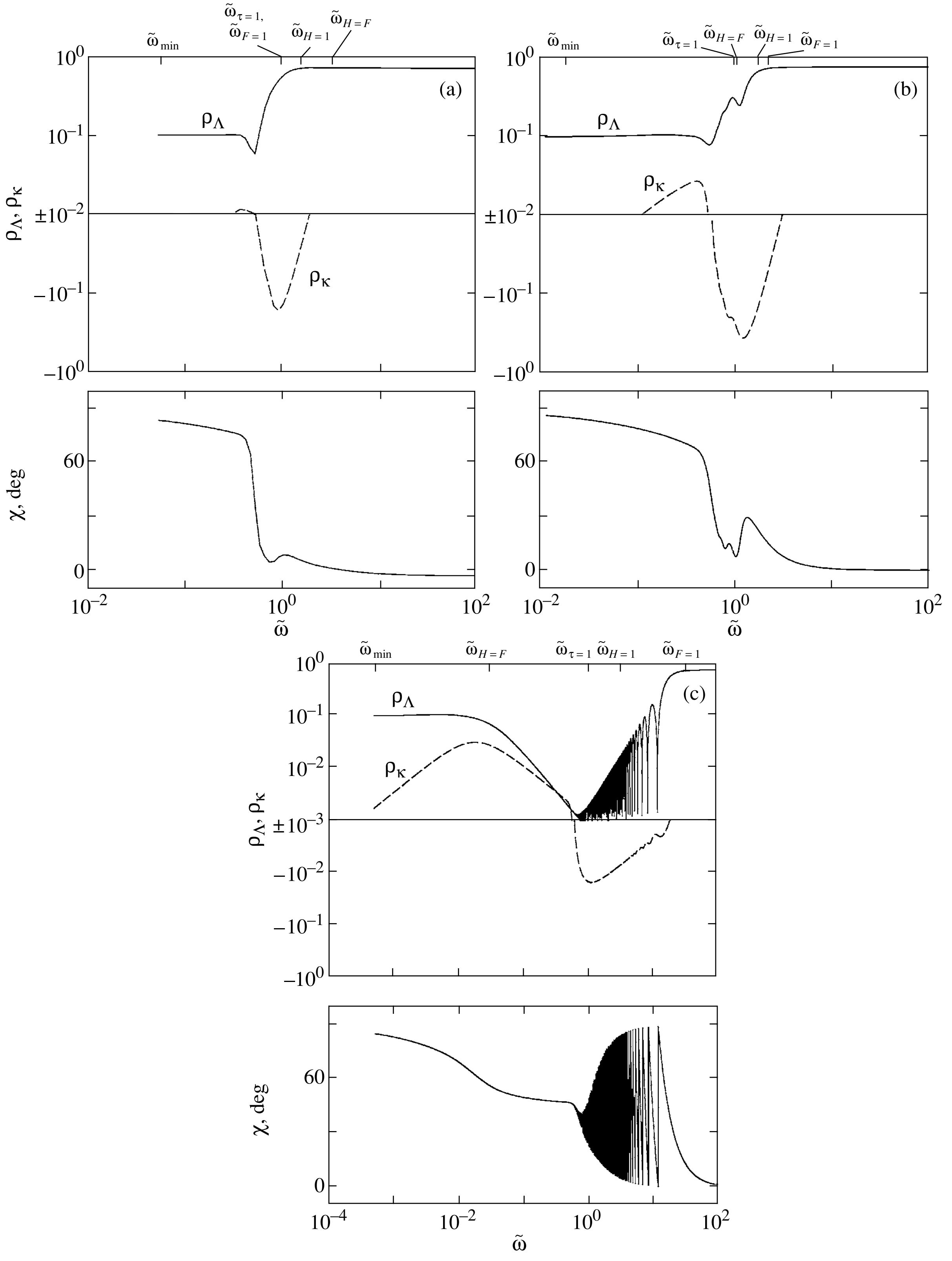

Fig. 2. The polarization spectra of the synchrotron radiation from a source with a relativistic electron plasma: (a) case B ($\gamma = 3$, $\Gamma_{\min} = 10^2$, $\varphi = 45°$, $F_0 = 1$); (b) case C ($\gamma = 3$, $\Gamma_{\min} = 10^2$, $\varphi = 45°$, $F_0 = 5$); (c) case D ($\gamma = 3$, $\Gamma_{\min} = 10^2$, $\varphi = 45°$, $F_0 = 10^3$).

of the frequency band (4.10) can be determined from the condition $H = F$ (cf. (4.2)). In the band (4.10), the normal waves are circularly polarized ($F \gg H$) and the phase difference $\phi \gg 1$. In this case, since the radiation sources and the normal waves have different polarizations, the polarization of the emergent radiation significantly decreases. In the high-frequency part of the band (4.10), where $\tilde{\omega} \gg \tilde{\omega}_{H=1}$, the radiation is depolarized by Faraday rotation, as in a cold plasma. The polarization spectrum here is described by formulas (3.6) and (3.7). In the low-frequency part $\tilde{\omega} \ll \tilde{\omega}_{H=1}$ of the band (4.10), the polarization frequency spectrum of the emergent radiation is described by the formulas

$$Q/I = 0, \qquad U/I = 0, \qquad \rho_\Lambda = 0; \qquad (4.11)$$
$$\rho_\kappa = \frac{V}{I} = -\rho^S \frac{H}{F} \propto -\tilde{\omega}^{-1}.$$

Here, the weak circular polarization of the emergent radiation (of the order of H/F) can be explained by the fact that the normal-wave polarization slightly differs from circular polarization and the electrons emit more energy into the extraordinary wave than into the ordinary wave [This effect is also known as the repolarization of radiation (Pacholczyk 1973).] As a result, the polarization of the emergent radiation is identical to the extraordinary-wave polarization.

Under the condition (4.9), the normal-wave polarization approaches a linear polarization at frequencies $\tilde{\omega} \lesssim \tilde{\omega}_{H=F}$ [i.e., below the band (4.10)]. Here, the polarization is described by expressions (4.6) at the frequencies $\tilde{\omega} \ll \tilde{\omega}_{\tau=1}$ of strong reabsorption and by formula (3.3) at frequencies $\tilde{\omega}_{\tau=1} \ll \tilde{\omega} \ll \tilde{\omega}_{H=F}$. Above the frequency band (4.10), the polarization spectrum of the synchrotron radiation corresponds to the spectrum (3.3) of an infinitely thin layer. The polarization frequency spectrum for the case under consideration (C) is shown in Fig. 2b.

(D) For even larger

$$F_0 \gg \left(\frac{\gamma+1}{3(\gamma-2)}\right)^{\gamma/2} \frac{a(\gamma)}{\gamma+1} g^{(\gamma-2)/2}, \qquad (4.12)$$

the lower limit $\tilde{\omega}_{H=F}$ of the depolarization band (4.10) is shifted to the range of strong reabsorption, $\tilde{\omega} \ll \tilde{\omega}_{\tau=1}$. In this case, the frequency band $\tilde{\omega}_{H=F} \ll \tilde{\omega} \ll \tilde{\omega}_{\tau=1}$ is formed below the frequency of the spectral intensity maximum, where the normal-wave polarization is nearly circular and the emissivities and absorption coefficients of the two types of normal waves become almost equal. The degree of polarization of the emergent radiation greatly decreases compared to the linear wave polarization (4.6). Its level is determined by the small difference between the transfer (absorption and emission) coefficients of the different normal waves due to a partial linear polarization of the latter ($\cos(2\sigma) \neq 0$):

$$\frac{Q}{I} = 0, \quad \frac{U}{I} = 0, \quad \rho_\Lambda = 0, \quad \chi = \frac{\pi}{2}, \qquad (4.13)$$
$$\rho_\kappa = \frac{V}{I} = (\rho^\varkappa - \rho^s)\frac{H}{F} \propto -\tilde{\omega}^{-1}.$$

It should be noted that the circular polarization of the emergent radiation ρ_κ changes sign at some frequency $\tilde{\omega} \sim \tilde{\omega}_{\tau=1}$, where ρ_κ becomes zero. The point is that because of the strong reabsorption of the extraordinary wave ($\rho^\varkappa > \rho^S$) at $\tilde{\omega} \ll \tilde{\omega}_{\tau=1}$, the polarization of the emergent radiation is identical to the ordinary-wave polarization. Above this frequency (at $\tilde{\omega}_{\tau=1} \ll \tilde{\omega} \ll \tilde{\omega}_{H=1}$), the reabsorption is negligible and the polarization of the emergent radiation approaches the extraordinary-wave polarization.

Outside the range $\tilde{\omega}_{H=F} \ll \tilde{\omega} \ll \tilde{\omega}_{\tau=1}$, the polarization frequency spectrum of the emergent radiation is described by the same formulas as in the case (4.9), by (4.6) at $\tilde{\omega} \ll \tilde{\omega}_{H=F}$, by (4.11) at $\tilde{\omega}_{\tau=1} \ll \tilde{\omega} \ll \tilde{\omega}_{H=1}$, by (3.6) and (3.7) at $\tilde{\omega}_{H=1} \ll \tilde{\omega} \ll \tilde{\omega}_{F=1}$, and by (3.3) at $\tilde{\omega} \gg \tilde{\omega}_{F=1}$ (see Fig. 2c).

Note that in the approximation of the purely linear polarization of the sources, a further increase in F_0 causes no new qualitative changes in the polarization spectrum: the characteristic frequencies follow in the established order

$$\tilde{\omega}_{\min} < \tilde{\omega}_{H=F} < \tilde{\omega}_{\tau=1} < \tilde{\omega}_{H=1} < \tilde{\omega}_{F=1}.$$

However, our assumption of the purely linear polarization of the sources breaks down for

$$F_0 \gtrsim \left(\frac{\gamma+1}{3(\gamma-2)}\right)^{5\gamma/(\gamma+4)} \left(\frac{a(\gamma)}{\gamma+1}\right)^{4/(\gamma+4)}$$
$$\times (\sqrt{2}\ln\Gamma_{\min})^{6\gamma/(\gamma+4)} g^{(11\gamma-4)/(\gamma+4)}.$$

In this case, the degree of polarization of the radiation at $\tilde{\omega}_{H=1}$ (where it is at a minimum) drops below the level $\rho_\kappa^S \sim \Gamma_{\min}^{-1}(\tilde{\omega}_{\min}/\tilde{\omega}_{H=1})^{1/2} \cot\varphi$ of weak circular polarization of the synchrotron sources.

Thus, for a relativistic electron plasma, the polarization spectrum of the emergent synchrotron radiation has three characteristic shapes. For low F_0 given by inequality (4.3), the polarization frequency spectrum corresponds to the spectrum (3.3) of an infinitely thin layer. In case (4.4), the polarization of the radiation remains linear at all frequencies; near the frequency of the spectral intensity maximum, the linear polarization plane rotates through $\pi/2$. In the case (4.12) corresponding to large F_0, the polarization frequency spectrum contains the frequency band (4.10), where the radiation is significantly depolarized; the degree of polarization reaches a minimum at frequency (4.8). Above this frequency, the radiation is linearly polarized and undergoes the Faraday rotation of the polarization plane as the frequency changes. Below the frequency (4.8), the radiation is circularly polarized. In this case, above the frequency of the spectral intensity maximum, the absolute value of the circular polarization depends on frequency as $\tilde{\omega}^{-1}$. Near $\tilde{\omega}_{\tau=1}$, the circular polarization changes sign. At lower frequencies, its absolute value again follows the low $\tilde{\omega}^{-1}$.

The intermediate case (4.9) clearly stands out only at sufficiently large Lorentz factors $\Gamma_{\min} \gtrsim 10^6$. At smaller $\Gamma_{\min}$, inequality (4.9) holds only in a narrow range of F_0. For example, at $\Gamma_{\min} = 10^2$, $\gamma = 3$, and $\varphi = \pi/4$, the boundaries of inequality (4.9) have similar (in order of magnitude) values, 2.7 and 5.6.

5. A RELATIVISTIC ELECTRON–POSITRON PLASMA

A plasma composed of relativistic electron–positron pairs is distinguished by the absence of gyrotropy ($F = 0$). The permittivity tensor for this plasma corresponds to a uniaxial crystal. The normal waves, along with the radiation sources in the jet, are linearly polarized over the entire frequency range. In this case, the polarization plane of the radiation sources coincides with the polarization plane of the extraordinary wave.

If there is an admixture of cold electrons in the jet, or if the positron number density is not equal to the relativistic-electron density, then, strictly speaking, the approximation of the linear normal-wave polarization holds only in a limited frequency range, $\tilde{\omega} \ll \tilde{\omega}_{H=F} \equiv H_0/F_0$. Nevertheless, the polarization spectrum of the synchrotron radiation from the jet is identical to the polarization spectrum of a jet containing only relativistic electron–positron pairs at all frequencies if the frequency $\tilde{\omega}_{H=F}$ lies in the range where the phase difference $\phi \ll 1$. The latter imposes the following constraints on the number densities of the components:

$$n_{\mathrm{c}} \ll \frac{n_- + n_+}{\Gamma_{\min}\cot\varphi}, \quad n_- - n_+ \ll \frac{(n_- + n_+)\Gamma_{\min}}{\cot\varphi \ln\Gamma_{\min}}, \tag{5.1}$$

and on the range of admissible variations in H_0:

$$H_0^{(\gamma+4)/3(\gamma-2)} \ll 3^{-\gamma/(\gamma-2)}\frac{\gamma-1}{\gamma-2}\left(\frac{a(\gamma)}{\gamma-2}\right)^{2/(\gamma-2)} \tag{5.2}$$

$$\times \frac{(n_- + n_+)\cot^{-1}\varphi}{n_{\mathrm{c}}\Gamma_{\min} + \dfrac{\gamma-1}{\gamma+1}(n_- - n_+)\dfrac{\ln\Gamma_{\min}}{\Gamma_{\min}}}.$$

The polarization of the radiation emerging from an electron–positron plasma depends on the pattern of variation in the magnetic field $\mathbf{B}(z)$ along the line of sight in the jet, more specifically, on the presence or absence of a magnetic-field shear.

Let us first consider a uniform magnetic field, $\mathbf{B}(z) = \mathrm{const}$. Since, as was noted above, the polarization planes of the sources and the normal waves coincide, the shape of the polarization frequency spectrum for the emergent radiation is related only to different normal-wave reabsorption. If

$$H_0 \ll \frac{2^{-(\gamma-2)/2}a(\gamma)}{3(\gamma-2)} \sim 1, \tag{5.3}$$

then $\tau \ll 1$ over the entire range $\tilde{\omega} > \tilde{\omega}_{\min}$ and the polarization spectrum is described by formulas (3.3) for an infinitely thin layer. In the case opposite to (5.3), $\tilde{\omega}_{\tau=1} \gg \tilde{\omega}_{\min}$ and the role of normal-wave reabsorption becomes significant. The polarization frequency spectrum has the same shape as that for a relativistic electron plasma under condition (4.4). The radiation is linearly polarized at all frequencies. At low frequencies ($\tilde{\omega} \ll \tilde{\omega}_{\tau=1}$), the polarization direction coincides with the direction of the magnetic-field projection onto the picture plane. At high frequencies ($\tilde{\omega} \gg \tilde{\omega}_{\tau=1}$), the radiation is polarized in a perpendicular direction. In this case, the degree of polarization $\rho_\Lambda = (3\gamma+3)/(3\gamma+7)$ at high frequencies is higher than the degree of polarization $\rho_\Lambda = 3/(6\gamma+13)$ at low frequencies (see Fig. 3a).

Under certain conditions, a smooth variation in magnetic field $\mathbf{B}$ (with a scale length much larger than the wavelength) leads to the so-called linear wave interaction (Zheleznyakov 1997). The latter manifests itself in the following: if, for example, only the extraordinary wave falls on a region with a nonuniform magnetic field, then two coherent extraordinary and ordinary waves emerge from this region. As a result, the linear interaction provides an additional mechanism of the change in the polarization of the emergent radiation. In our case, it is important that this effect gives rise to a strong circular polarization of the radiation from a jet filled with an electron–positron plasma.

The effect of a magnetic-field shear on the wave propagation in a cold plasma was considered by Kocharovskiĭ and Kocharovskiĭ (1980). They obtained basic criteria for the linear interaction and solved the standard problem for a monotonic shear in a plasma sheet. These results can be directly extended to the case of a relativistic electron–positron plasma concerned. At the same time, because of the absence of gyrotropy, the necessary formulas for an electron–positron plasma are identical (to within the notation) to the corresponding expressions

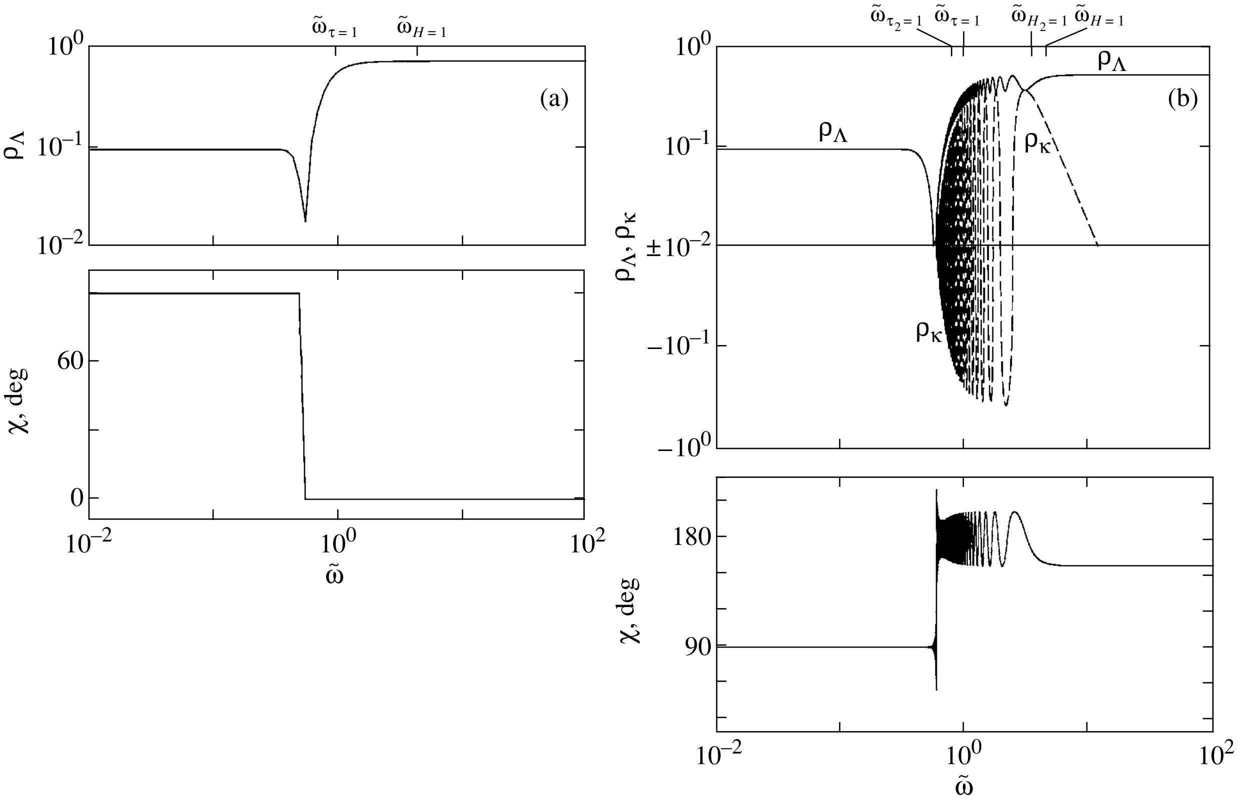

Fig. 3. The polarization spectra of the synchrotron radiation from a source with a relativistic electron–positron plasma: (a) without a magnetic-field shear ($\gamma = 3$, $\Gamma_{\min} = 10^2$, $\varphi = 45°$, $H_0 = 10^2$); (b) with a magnetic-field shear ($\gamma = 3$, $\Gamma_{\min} = 10^2$, $\varphi = 45°$, $H_0 = 10^2$, $\Delta\chi_B = 45°$, $l_2 = 0.5$).

derived by Kocharovskiĭ and Kocharovskiĭ (1982) for cholesteric liquid crystals [see also Zheleznyakov *et al.* (1983) for a review]. Electrodynamically, these crystals, as well as an electron–positron plasma with a shear, are equivalent to uniaxial crystals with a turning symmetry axis. According to Zheleznyakov *et al.* (1983), the degree of linear polarization in this case is specified by the parameter

$$G = \left| \frac{4\sqrt{2}\mathrm{d}\vartheta/\mathrm{d}z}{\mathrm{d}\tilde{q}/\mathrm{d}z} \right|, \qquad (5.4)$$

where ϑ is the angle between the magnetic-field projection $\mathbf{B}(z)$ onto the picture plane and some fixed x_0 axis in this plane and $\tilde{q} = -(2L_\phi \mathrm{d}\vartheta/\mathrm{d}z)^{-1}$. The quantity (5.4) is taken at $\tilde{q}^2 = 1$, i.e., at point z where the scale length $|\mathrm{d}\vartheta/\mathrm{d}z|^{-1}$ of the magnetic-field rotation is equal to the distance $2L_\phi \equiv 2|h_{\mathrm{rel}}^{-1}|$ at which the normal waves acquire a phase difference of the order of unity. The quantity h_{rel} is given by formulas (2.4). A numerical expression for the length $2L_\phi$ at $\gamma = 3$ convenient for practical estimates can be represented as

$$2L_\phi = 2.45 \times 10^2 \left(\frac{B\sin\varphi}{10^{-2}\,\mathrm{G}}\right)^{-2} \left(\frac{n_- + n_+}{1\,\mathrm{cm}^{-3}}\right)^{-1} \times \left(\frac{\Gamma_{\min}}{10^2}\right)^{-1} \left(\frac{\omega/(2\pi)}{10\,\mathrm{GHz}}\right)^3 \mathrm{pc}.$$

If the phase difference acquired in the region with a shear is much larger than unity, then $\tilde{q}^2 \gg 1$ for all z and the geometrical-optics approximation holds. In this case, there is no linear interaction between the normal waves: both normal waves propagate independently, with the acquired phase difference between them being approximately the same as during the passage through a region with a uniform magnetic field. In this case, a magnetic-field shear does not affect the polarization spectrum of the emergent radiation. The spectrum remains the same as that for a source with a uniform magnetic field whose direction coincides with the magnetic-field direction at the exit from the source.

A strong linear interaction ($G \ll 1$) appears in a tenuous plasma with a weak magnetic field at sufficiently high frequencies when the normal waves acquire a phase difference much smaller than unity in a region with a shear. The linear interaction is mainly localized in regions where $|\mathrm{d}\vartheta/\mathrm{d}z|^{-1} \sim 2L_\phi$.

Let us consider a simple model of a jet with a nonuniform magnetic field that has a shear, i.e., a change in the direction of the $\mathbf{B}(z)$ projection onto the picture plane along the propagation path of the radiation in the jet. The magnitude of $\mathbf{B}(z)$ and the angle φ are assumed to be constant, and only the angle ϑ is varied.

Let ray path in the jet passes through two layers, 1 and 2, of length L_1 and L_2, respectively, in which the magnetic field is uniform and the orientation of its projections $\mathbf{B}_{\perp 1}$ and $\mathbf{B}_{\perp 2}$ onto the picture plane is characterized by the angles ϑ_1 and ϑ_2 in these layers. Layers 1 and 2 are separated by a narrow transition region of length $\Delta L \ll \{L_1, L_2\}$, in which the angle ϑ smoothly and monotonically changes by $\Delta\chi_B = \vartheta_2 - \vartheta_1$. Since the extent of the transition region is small, we may ignore its intrinsic radiation compared to the radiation from layers 1 and 2.

The standard problem for this model of a shear in the transition region was solved by Kocharovskiĭ and Kocharovskiĭ (1980). If the angle ϑ changes from ϑ_1 to ϑ_2 near the point $z = L_1$ as

$$\vartheta = \vartheta_1 + 2(\Delta\chi_B/\pi)\arctan[\exp((z - L_1)/(2\Delta L))],$$

i.e., in a layer $\sim \Delta L$ in thickness, then when an extraordinary wave of unit amplitude falls on the layer, coherent extraordinary and ordinary waves with amplitudes $\sqrt{1 - Q_\mathrm{s}}$ and $\sqrt{Q_\mathrm{s}}$, respectively, will emerge from the layer. Here, the transformation coefficient

$$Q_\mathrm{s} = \frac{\sin^2(\Delta\chi_B)}{\cosh^2(\pi\Delta L/L_\phi)}. \qquad (5.5)$$

For slow magnetic-field rotation ($\Delta L \gg L_\phi$), when $\tilde{q}^2 \gg 1$ for all z and there is a weak linear interaction, the amplitude of the emerging ordinary wave is exponentially small [see formula (5.5)]. For fast magnetic-field rotation ($\Delta L \ll L_\phi$), the points $\tilde{q}^2 = 1$ appear, at which

$$G = \frac{4\sqrt{2}\Delta L}{L_\phi} \ll 1,$$

and a strong linear interaction takes place. In this case, the transformation coefficient $Q_\mathrm{s} = \sin^2(\Delta\chi_B)$ corresponds to the propagation of radiation in a vacuum, i.e., without any change in the polarization of the radiation in the transition region.

In the latter case, which we only consider here, the Stokes parameters are constant in a coordinate system whose axes are fixed in space (not tied to the magnetic-field direction). The Stokes parameters at the exit from layer 1 (and, accordingly, at the entrance into layer 2) are

$$I_1 = PL_1\left(\frac{1+\rho^S}{2}\frac{1-\exp(-2\varkappa_\mathrm{e}L_1)}{2\varkappa_\mathrm{e}L_1} + \frac{1-\rho^S}{2}\frac{1-\exp(-2\varkappa_\mathrm{o}L_1)}{2\varkappa_\mathrm{o}L_1}\right), \qquad (5.6)$$

$$Q_1 = PL_1\left(\frac{1+\rho^S}{2}\frac{1-\exp(-2\varkappa_\mathrm{e}L_1)}{2\varkappa_\mathrm{e}L_1} - \frac{1-\rho^S}{2}\frac{1-\exp(-2\varkappa_\mathrm{o}L_1)}{2\varkappa_\mathrm{o}L_1}\right),$$

$$U_1 = V_1 = 0,$$

where the factors $2\varkappa_\mathrm{e}L_1$ and $2\varkappa_\mathrm{o}L_1$ constitute the optical depths of layer 1 for the extraordinary and ordinary waves, respectively. Formulas (5.6) were derived from formulas (2.16) and (2.21)–(2.23) by taking into account the linear normal-wave polarization ($\sigma = 0$).

The Stokes parameters (5.6) describe the radiation incident on layer 2 in a x_1y_1 coordinate system with the y_1 axis directed along the projection $\mathbf{B}_{\perp 1}$ of the magnetic field in layer 1 onto the picture plane. To calculate the radiation emerging from layer 2, the parameters (5.6) should be written in a x_2y_2 coordinate system, in which the y_2 axis is directed along the projection $\mathbf{B}_{\perp 2}$ of the magnetic field in layer 2 onto the picture plane:

$$I_\mathrm{inc} = I_1, \quad Q_\mathrm{inc} = Q_1\cos(2\Delta\chi_B), \qquad (5.7)$$
$$U_\mathrm{inc} = -Q_1\sin(2\Delta\chi_B), \quad V_\mathrm{inc} = 0.$$

As a result, the radiation of the entire source emerging from layer 2 is the sum of the intrinsic radiation from layer 2 and the radiation from layer 1 modified when it passes through layer 2 by absorption and the Cotton–Mouton effect (the transverse Faraday effect), which appears in layer 2 because of the shear in the transition region between layers 1 and 2:

$$I = PL_2\left(\frac{1+\rho^S}{2}\frac{1-\exp(-2\varkappa_\mathrm{e}L_2)}{2\varkappa_\mathrm{e}L_2} + \frac{1-\rho^S}{2} \times \frac{1-\exp(-2\varkappa_\mathrm{o}L_2)}{2\varkappa_\mathrm{o}L_2}\right) + \frac{I_\mathrm{inc}+Q_\mathrm{inc}}{2}\exp(-2\varkappa_\mathrm{e}L_2) + \frac{I_\mathrm{inc}-Q_\mathrm{inc}}{2}\exp(-2\varkappa_\mathrm{o}L_2), \qquad (5.8)$$

$$Q = PL_2\left(\frac{1+\rho^S}{2}\frac{1-\exp(-2\varkappa_\mathrm{e}L_2)}{2\varkappa_\mathrm{e}L_2} - \frac{1-\rho^S}{2} \times \frac{1-\exp(-2\varkappa_\mathrm{o}L_2)}{2\varkappa_\mathrm{o}L_2}\right) + \frac{I_\mathrm{inc}+Q_\mathrm{inc}}{2}\exp(-2\varkappa_\mathrm{e}L_2) - \frac{I_\mathrm{inc}-Q_\mathrm{inc}}{2}\exp(-2\varkappa_\mathrm{o}L_2),$$

$$U = U_{\text{inc}} \cos(|h_{\text{rel}}|L_2) \exp(-(\varkappa_{\text{e}} + \varkappa_{\text{o}})L_2),$$
$$V = -U_{\text{inc}} \sin(|h_{\text{rel}}|L_2) \exp(-(\varkappa_{\text{e}} + \varkappa_{\text{o}})L_2),$$

where the factors $2\varkappa_{\text{e}}L_2$ and $2\varkappa_{\text{o}}L_2$ are the optical depths of layer 2 for the extraordinary and ordinary waves and $|h_{\text{rel}}|L_2$ is the phase difference between the normal waves in layer 2.

According to (5.8), the Cotton–Mouton effect produces a partial circular polarization of the emergent radiation. The degree of circular polarization ρ_κ of the emergent radiation is at a maximum for the magnetic-field rotation angle $\Delta\chi_B = \pi/4$ (when the linearly polarized radiation of layer 1, as it passes through the transition layer with a magnetic-field shear, transforms into coherent ordinary and extraordinary waves of layers 2 with equal amplitudes).

It follows from formulas (5.7) and (5.8) that the polarization spectrum of the radiation from a source with a shear is specified by two parameters: $H_0 = |h_{\text{rel}}(\omega_{\tau=1})|L$, the phase difference between the normal waves at frequency $\tilde{\omega}_{\tau=1}$ [given by (2.24)] on the length L of the entire source, and $l_2 = L_2/L$, the relative length of layer 2. The optical depths of layers 1 and 2 and the phase difference in layer 2 $|h_{rel}|L_2$, which appear in formulas (5.6) and (5.8), can be expressed in terms of H_0 and l_2 as

$$2\varkappa_{\text{e}}L_1 = (1 + \rho^{\varkappa})l_1\tau, \quad 2\varkappa_{\text{o}}L_1 = (1 - \rho^{\varkappa})l_1\tau, \tag{5.9}$$
$$2\varkappa_{\text{e}}L_2 = (1 + \rho^{\varkappa})l_2\tau, \quad 2\varkappa_{\text{o}}L_2 = (1 - \rho^{\varkappa})l_2\tau,$$
$$|h_{\text{rel}}|L_2 = l_2H, \quad l_1 = 1 - l_2, \quad \tau = \tilde{\omega}^{-(\gamma+4)/2},$$
$$H = H_0/\tilde{\omega}^3,$$

where l_1 is the relative length of layer 1, τ is the optical (2.25) depth of the entire source, H is the phase difference between the normal waves at frequency $\tilde{\omega}$ on the length of the entire source [cf. (2.26)], the dimensional frequency $\tilde{\omega} \equiv \omega/\omega_{\tau=1}$.

(A) As in the case of a jet with a uniform magnetic field, here, we can separate out two characteristic ranges of H_0 given by (5.3) and the inequality opposite to it. Under the condition (5.3), the phase difference $\phi = H$ and the optical depth τ of the entire layer (let alone separately for layers 1 and 2) is much smaller than unity. The emergent radiation is mainly linearly polarized and its polarization is described by the formulas

$$\frac{Q}{I} = \rho^S[1 - (1 - l_2)(1 - \cos(2\Delta\chi_B))], \tag{5.10}$$
$$\frac{U}{I} = -\rho^S(1 - l_2)\sin(2\Delta\chi_B),$$
$$\rho_\Lambda = \rho^S\sqrt{1 - 4l_2(1 - l_2)\sin^2(\Delta\chi_B)},$$
$$\rho_\kappa = \frac{V}{I} = \rho^S Hl_2(1 - l_2)\sin(2\Delta\chi_B) \ll 1.$$

A magnetic-field shear qualitatively does not change the polarization spectrum of the emergent radiation compared to the case of an infinitely thin source with uniform magnetic field. Only the degree of linear polarization of the radiation decreases at all frequencies and a weak circular polarization appears. For $l_1 \gg l_2$ or $l_2 \gg l_1$, the polarization of the emergent radiation is identical to the polarization of the intrinsic radiation from the first or second layer.

(B) In the limiting case of large H_0 opposite to (5.3), we can separate out several ranges of l_2 in which the polarization spectrum of the emergent radiation assumes different shapes. The case of a thin layer 2

$$l_2 \ll \frac{H_0^{-(\gamma+4)/(\gamma-2)}}{2^{(\gamma+4)/2}}\left(\frac{a(\gamma)}{3(\gamma-2)}\right)^{(\gamma+4)/(\gamma-2)} \tag{5.11}$$

with a small optical depth $l_2\tau$ and phase difference $l_2H \ll 1$ at $\tilde{\omega} > \omega_{\min}$ reduces to the case of a uniform source with the parameters of layer 1.

(C) The presence of layer 2 manifests itself when the inequality opposite to (5.11) is satisfied in the frequency range $\tilde{\omega} \lesssim \tilde{\omega}_{H_2=1} = (l_2H_0)^{1/3}$, where the phase difference $l_2H \gtrsim 1$. Under the condition

$$\frac{H_0^{-(\gamma+4)/(\gamma-2)}}{2^{(\gamma+4)/2}}\left(\frac{a(\gamma)}{3(\gamma-2)}\right)^{(\gamma+4)/(\gamma-2)}$$
$$\ll l_2 \ll H_0^{-1} \ll 1 \tag{5.12}$$

the upper limit $\tilde{\omega}_{H_2=1}$ of the range of appreciable effect of layer 2 is below the frequency of the spectral intensity maximum of the entire source.

In this case, the polarization spectrum of the emergent radiation at $\tilde{\omega} \gg \tilde{\omega}_{H_2=1}$ is identical to the polarization spectrum of layer 1 with a uniform magnetic field. The radiation is linearly polarized at all frequencies. Above $\tilde{\omega}_{\tau=1}$, the degree of linear polarization $f_\Lambda = (3j+3)/(3j+7)$; at $\tilde{\omega}_{H_2} = 1 \ll \tilde{\omega} \ll \tilde{\omega}_{\tau=1}$, $f_\Lambda = 3/(6j+13)$. Near the spectral intensity maximum near $\tilde{\omega}_{\tau=1}$, the polarization plane rotates through $\pi/2$.

At lower frequencies $\tilde{\omega}_{\tau_2=1} \ll \tilde{\omega} \ll \tilde{\omega}_{H_2=1}$, where the frequency $\tilde{\omega}_{\tau_2=1} = l_2^{2/(\gamma+4)}$ is determined by the condition $l_2\tau(\tilde{\omega}_{\tau_2=1}) = 1$, the phase difference $l_2H \gg 1$ and the Cotton–Mouton effect in layer 2 becomes significant. At the same time, the reabsorption in layer 2 is still weak ($l_2\tau \ll 1$) and the radiation from layer 1 dominates in the emergent radiation energing from the jet. The presence of layer 2 gives rise to a partial circular polarization of the radiation emerging from the jet. In this case, the degree of linear polarization changes in such a way that the total degree of polarization of the emergent radiation $\rho = (\rho_\Lambda^2 + \rho_\kappa^2)^{1/2}$ remains constant and is equal to the degree of polarization $\rho = |\rho^S - \rho^\varkappa|/(1 - \rho^\varkappa \rho^S)$ of the radiation from layer 1 with a uniform magnetic field in the range of strong reabsorption [see (4.6)]:

$$\frac{Q}{I} = \frac{\rho^S - \rho^\varkappa}{1 - \rho^\varkappa \rho^S} \cos(2\Delta\chi_B), \qquad (5.13)$$

$$\frac{U}{I} = -\frac{\rho^S - \rho^\varkappa}{1 - \rho^\varkappa \rho^S} \sin(2\Delta\chi_B)\cos(l_2 H),$$

$$\frac{V}{I} = \frac{\rho^S - \rho^\varkappa}{1 - \rho^\varkappa \rho^S} \sin(2\Delta\chi_B)\sin(l_2 H).$$

At very low frequencies $\tilde{\omega} \ll \tilde{\omega}_{\tau_2=1}$, the radiation from layer 1 is absorbed by layer 2 and the polarization of the emergent radiation is identical to the polarization of the radiation from layer 2. As previously, the polarization spectrum of the radiation is described by formulas (4.6) for a layer with a uniform magnetic field in the range of strong reabsorption.

(D) As the relative length l_2 of layer 2 increases to

$$H_0^{-1} \ll l_2 \ll 1, \qquad (5.14)$$

the frequency range of large circular- and linear-polarization oscillations extends to frequencies above the spectral intensity maximum of the jet radiation. The polarization oscillations in this frequency range ($\tilde{\omega}_{\tau=1} \ll \tilde{\omega} \ll \tilde{\omega}_{H_2=1}$) do not differ qualitatively from the oscillations below the spectral intensity maximum ($\tilde{\omega}_{\tau_2=1} \ll \tilde{\omega} \ll \tilde{\omega}_{\tau=1}$). Only the oscillation amplitude increases—it becomes equal to $\rho^S \sin(2\Delta\chi_B)$:

$$\frac{Q}{I} = \rho^S \cos(2\Delta\chi_B), \qquad (5.15)$$

$$\frac{U}{I} = -\rho^S \sin(2\Delta\chi_B)\cos(l_2 H),$$

$$\frac{V}{I} = \rho^S \sin(2\Delta\chi_B)\sin(l_2 H).$$

(E) For $1 - l_2 \ll 1$, layer 2 mainly contributes to the Stokes parameters. In this case, the polarization spectrum at all frequencies is again almost identical to the polarization spectrum of a source with a uniform magnetic field. Only small circular- and linear-polarization oscillations above the spectral intensity maximum (in the frequency range $\tilde{\omega}_{\tau=1} \lesssim \tilde{\omega} \lesssim \tilde{\omega}_{H=1}$) are superimposed on this spectrum. The oscillation amplitude is of the order of $1 - l_2 \ll 1$ for circular polarization and $(1 - l_2)^2 \ll 1$ for linear polarization (Fig. 3b).

Thus, the radiation spectrum of an electron–positron plasma with a magnetic-field shear is distinguished by a significant degree of circular polarization of the radiation comparable to the degree of linear polarization. The degree of circular polarization oscillates with decreasing frequency, changing sign. If the shear is localized close to the location where the ray emerges from the jet [see inequalities (5.11) and (5.12)], then either there is no noticeable circular polarization of the radiation or it occurs at very low frequencies (below the spectral intensity maximum). In the remaining cases, the frequency range of significant circular polarization includes the frequency of the spectral intensity maximum and extends above it. However, the degree of circular polarization decreases over the entire frequency range if the extent of layer 1 becomes relatively small ($1 - l_2 \ll 1$).

6. CONCLUSIONS

Our analysis of the polarization frequency spectra for synchrotron radiation without invoking any additional considerations based on the jet energetics, etc., leads us to the following conclusions regarding the possible plasma composition in jets. The standard polarization spectra for discrete cosmic synchrotron radio sources composed of cold plasma with an admixture of relativistic electrons (supernova remnants, radio galaxies, etc.) are shown in Figs. 1a and 1b. The spectral shape is determined by the fixed structure of the normal waves in cold plasma and by the polarization of the synchrotron radiation from relativistic particles. Since this polarization does not depend on the sign of the charge of these particles, the observed polarization spectrum does not depend on the composition of the relativistic component in a cold plasma: the spectra are virtually identical for the electron and positron components and for the mixed electron–positron component.

This implies that the specific composition of the admixture of relativistic particles in a cold jet plasma cannot be determined from the polarization spectrum of the synchrotron radiation. Nor can it be determined for any composition of a tenuous plasma in jets with a weak magnetic field under the conditions when the phase difference ϕ between the ordinary and extraordinary waves acquired on the jet sizes and the optical depth τ attributable to synchrotron reabsorption are small compared to unity. In this case, the polarization frequency spectra are identical and match the polarization spectrum of the electron (or positron) radiation in a vacuum: the radiation is linearly polarized and there is no circular polarization (see Figs. 1–3 for $\tilde{\omega} \gg \tilde{\omega}_{\tau=1}, \tilde{\omega} \gg \tilde{\omega}_{F=1}$).

Comparison of the spectra in Fig. 1 and Figs. 2 and 3 (see also the table) indicates that the qualitative difference between a purely relativistic (electron or electron–positron) plasma and a cold plasma with an admixture of relativistic particles is a high ($\sim$ 10%; see Figs. 2, 3) linear polarization at frequencies $\tilde{\omega} < \tilde{\omega}_{\tau=1}$ (i.e., in the range of strong reabsorption, at the low-frequency slope of the intensity spectrum

Characteristic features of the polarization spectra

Jet plasma composition	Characteristic features of polarization			
	linear polarization in the range of strong reabsorption	oscillations of ρ_Λ and χ in the range of weak reabsorption	strong circular polarization ρ_κ	oscillations of ρ_κ
Cold plasma with an admixture of relativistic particles	$-$	$+$	$-$	$-$
Relativistic electron plasma	$+$	$+$	$+$	$\mp$
Relativistic electron–positron pairs	$+$	$\mp$	$\mp$	$\mp$

Note: The $+$ signs mark the features in the polarization spectrum that distinguish a given plasma composition. The $-$ signs indicate the absence of the corresponding feature. The $\mp$ signs mean that there is no such spectral feature for a uniform magnetic field in the jet but a magnetic-field shear produces it.

for the synchrotron radiation) and the possible appearance of strong circular polarization under certain conditions. The emergence of a circularly polarized component (with $\rho_\kappa \lesssim 10\%$) in the radiation from a relativistic electron plasma is attributable to the elliptical polarization of the normal waves near $\tilde{\omega}_{H=F}$ [see Eq. (4.2)]. This component is absent in a relativistic electron–positron plasma if the magnetic field in the jet is uniform (Fig. 3a). However, in the presence of a magnetic-field shear, the situation changes sharply: a linear wave interaction attributable to the field $\mathbf{B}(z)$ rotation arises here under favorable conditions. This effect gives rise to a strong circular polarization, which can reach several tens of percent (Fig. 3b) at frequencies $\sim\tilde{\omega}_{H=1}$ or lower.

The possibility of determining the specific relativistic-plasma composition only from the shape of the polarization spectra (i.e., without an allowance for the real possibilities of pair production near black holes and without making any judgments on the efficiency of the various relativistic-particle acceleration mechanisms) appears questionable. If we compare Figs. 2b, 2c, and 3b, then we will see that there are deep linear-polarization oscillations in the case of relativistic electron plasma in a jet with a uniform magnetic field; at the same time, circular-polarization oscillations emerge in jets with a magnetic-field shear composed of electron–positron plasma. This difference can disappear if we take into account the shear effect in a jet with relativistic electron plasma, which produces ρ_κ oscillations in this case as well. At the same time, it is clear that this kind of polarization oscillations is actually difficult to detect because of the high probability of these oscillations being blurred when the polarization is averaged over the receiving-antenna beam.

In conclusion, note that the available radio-astronomical data on the polarization of jet radiation are very scarce. The measurements made by Wardle *et al.* (1998) at 15 GHz revealed a circular polarization of about 1% in the jets of the quasar 3C 279. This value is too low to reach a definitive conclusion regarding the plasma composition, especially if it is considered that it is at the level of the corrections introduced by a number of effects (a weak circularly polarized component of the synchrotron radiation from individual particles, a slightly elliptical polarization of the normal waves, etc.). These effects are difficult to take into account and to separate; and the correct conclusion regarding the plasma composition is difficult to reach on their basis. Gabuzda *et al.* (2000) reported large variations of the linear polarization and angle χ in the radio emission from the BL Lac object 0716+714 at 5 GHz on a time scale of several hours. The degree of linear polarization varied over the range from 2 to 13% and the polarization plane rotated through ∼45°. Finally, Ros *et al.* (2000) presented radio observations of the jet in the quasar 3C 345 at wavelengths of 1.3, 2.0, 3.6, and 6 cm. In the latter case, the linear polarization reached 15%, with the orientation of the polarization plane changing slowly within the jet. This circumstance suggests that the magnetic field in the jets studied is not random in nature: the field nonuniformity scale is comparable to or only several times smaller than the jet linear size. The latter justifies the choice of the simple jet models with a uniform magnetic field and with a magnetic-field shear discussed here.

Several papers devoted to this problem were previously published by Jones and O'Dell (1977b), Jones (1988), and Fraix-Burnet (2002). Fraix-Burnet (2002) considers the linear-polarization oscillations, which lead to Faraday depolarization when averaging over the source sizes, to be a distinguishing feature of a jet containing a cold plasma (see Fig. 1b). At the same time, this effect is absent in a plasma of relativistic electron–positron pairs (Fig. 3a). However, as we see from Fig. 3b, ρ_Λ oscillations of this kind appear in the presence of a magnetic-field shear. Moreover, for certain combinations of parameters in a relativistic electron plasma, the polarization frequency spectrum does not differ qualitatively from the case of relativistic electrons in a cold plasma and contains the same ρ_Λ oscillations in the range of weak reabsorption ($\tau \ll 1$), as in a jet with a cold plasma.

Based on the absence (in their opinion) of Faraday depolarization in the observed objects, Jones and O'Dell (1977b) concluded that relativistic plasma could exist in polarized compact radio galaxies.

Based on a complex jet model with random magnetic fields, Jones (1988) performed extensive numerical calculations of the polarization of synchrotron radiation. The emphasis was on the low degrees of observed polarization of the radio emission at fixed frequencies. On the other hand, averaging the polarization over the source in the adopted model leads to additional difficulties in attempting to determine the plasma composition in the jet. Actually, as we made sure, a more thorough analysis of the polarization frequency spectra for synchrotron radiation is required to solve the problem of the corpuscular composition in jets.

It follows from our study that only extensive radioastronomical observations of plasma over a wide frequency range (not only at one or two frequencies, as has been and is being done to the present day) can provide conclusive evidence for the compositions of relativistic jets and primarily for the absence or presence of cold plasma in these objects. Only polarization measurements with high angular and frequency resolutions will make it possible to differentiate between a relativistic electron plasma and a plasma composed of relativistic electron–positron pairs.

ACKNOWLEDGMENTS

We wish to thank R.A. Sunyaev, on whose initiative this study was carried out, for fruitful discussions and remarks when discussing the paper. This study was supported by the Max-Planck-Institut für Astrophysik (Garching, Germany), the Russian Foundation for Basic Research (project no. 02-02-16236), the Counsil for Support of Leading Scientific Schools (project no. 00-15-96674), and the "Astronomy" Programs of the Presidium of the Russian Academy of Sciences and the Ministry of Industry, Science, and Technology.

REFERENCES

1. D. Fraix-Burnet, Astron. Astrophys. **381**, 374 (2002).
2. D. C. Gabuzda, P. Y. Kochenov, T. V. Cawthorne, and R. I. Kollgaard, Mon. Not. R. Astron. Soc. **313**, 627 (2000).
3. T. W. Jones, Astrophys. J. **332**, 678 (1988).
4. T. W. Jones and S. L. O'Dell, Astrophys. J. **214**, 522 (1977a).
5. T. W. Jones and S. L. O'Dell, Astron. Astrophys. **61**, 291 (1977b).
6. V. V. Kocharovskiĭ and Vl. V. Kocharovskiĭ, Fiz. Plazmy **6**, 565 (1980) [Sov. J. Plasma Phys. **6**, 308 (1980)].
7. V. V. Kocharovskiĭ and Vl. V. Kocharovskiĭ, Opt. Spektrosk. **52**, 297 (1982) [Opt. Spectrosc. **52**, 180 (1982)].
8. L. D. Landau and E. M. Lifshitz, *Course of Theoretical Physics,* Vol. 2: *The Classical Theory of Fields* (Nauka, Moscow, 1988; Pergamon, Oxford, 1975).
9. A. G. Pacholczyk, Mon. Not. R. Astron. Soc. **163**, 29P (1973).
10. A. G. Pacholczyk and T. L. Swihart, Astrophys. J. **161**, 415 (1970).
11. A. G. Pacholczyk and T. L. Swihart, Astrophys. J. **196**, 125 (1975).
12. E. Ros, J. A. Zensus, and A. P. Lobanov, Astron. Astrophys. **354**, 55 (2000).
13. V. N. Sazonov, Zh. Éksp. Teor. Fiz. **56**, 1075 (1969) [Sov. Phys. JETP **29**, 578 (1969)].
14. V. N. Sazonov and V. N. Tsytovich, Izv. Vyssh. Uchebn. Zaved., Radiofiz. **11**, 1287 (1968).
15. J. F. C. Wardle, D. C. Homan, R. Ojha, and D. H. Roberts, Nature **395**, 457 (1998).
16. V. V. Zheleznyakov, Astrophys. Space Sci. **2**, 417 (1968).
17. V. V. Zheleznyakov, *Radiation in Astrophysical Plasma* (Yanus-K, Moscow, 1997).
18. V. V. Zheleznyakov, V. V. Kocharovskiĭ, and Vl. V. Kocharovskiĭ, Usp. Fiz. Nauk **141**, 257 (1983) [Sov. Phys. Usp. **26**, 877 (1983)].

Translated by V. Astakhov

Astronomy Letters, Vol. 28, No. 11, 2002, pp. 745–754. Translated from Pis'ma v Astronomicheskiĭ Zhurnal, Vol. 28, No. 11, 2002, pp. 829–839.
Original Russian Text Copyright © 2002 by Suleimanov, Ghosh, Austin, Ramsey.

X-ray Emission from Accretion Disks in Active Galactic Nuclei

V. F. Suleimanov[1]*, K. K. Ghosh[2], R. A. Austin[2], and B. D. Ramsey[2]

[1] *Kazan State University, ul. Lenina 18, Kazan, 420008 Tatarstan, Russia*
[2] *NASA/G. Marshall Space Flight Center, Department of Space Research, USA*

Received February 15, 2002

Abstract—We constructed a grid of relativistic models for standard high-relative-luminosity accretion α-disks around supermassive Kerr black holes (BHs) and computed X-ray spectra for their hot, effectively optically thin inner parts by taking into account general-relativity effects. They are known to be heated to high ($\sim 10^6$–10^9 K) temperatures and to cool down through the Comptonization of intrinsic thermal radiation. Their spectra are power laws with an exponential cutoff at high energies; i.e., they have the same shape as those observed in active galactic nuclei (AGNs). Fitting the observed X-ray spectra of AGNs with computed spectra allowed us to estimate the fundamental parameters of BHs (their mass and Kerr parameter) and accretion disks (luminosity and inclination to the line of sight) in 28 AGNs. We show that the Kerr parameter for BHs in AGNs is close to unity and that the disk inclination correlates with the Seyfert type of AGN, in accordance with the unification model of activity. The estimated BH masses M_x are compared with the masses $M_{\rm rev}$ determined by the reverberation mapping technique. For AGNs with luminosities close to the Eddington limit, these masses agree and the model under consideration may be valid for them. For low-relative-luminosity AGNs, the differences in masses increase with decreasing relative luminosity and their X-ray emission cannot be explained by this model. *© 2002 MAIK "Nauka/Interperiodica".*

Key words: *active galactic nuclei, quasars, radio galaxies, X-ray emission, disk accretion.*

INTRODUCTION

A high proportion of active galactic nuclei (AGNs) possess a noticeable X-ray emission whose spectrum is a power law in the energy range 2–10 keV, $F_\nu \sim \nu^{-\alpha_x}$ (see Mushotsky *et al.* 1993), with the index α_x varying over a wide range, from 0.3 to 1.2. Recent BeppoSAX observations have revealed an exponential cutoff at energies above 50 keV (Matt 2001). A noticeable reflected component in the energy range 10–30 keV and an iron line at energies 6–7 keV are also observed. These additional components are assumed to arise when the emission from a primary source with a power-law spectrum is reflected from an accretion disk (AD) and/or from a system of clouds above the disk plane. Here, we investigate the nature of the primary X-ray source and discuss the possibility of explaining the reflected component in terms of the model under consideration.

The power-law spectral shape with a high-energy cutoff can be easily explained by an unsaturated Comptonization model (Sunyaev and Titarchuk 1980). Therefore, most of the models proposed to explain the X-ray emission from AGNs contain a cloud or a layer of hot electrons with $T_{\rm e} \sim 10^8$–10^9 K and $\tau_{\rm e} \sim 1$ in which the soft external photons emitted by the AD are Comptonized as the main element. Geometrically, this can be either a hot corona above a relatively cold disk (Bisnovatyi-Kogan and Blinnikov 1977; Haardt and Marashi 1993; Rozanska *et al.* 1999) or a hot cloud inside a cold AD with a corona (Meyer *et al.* 2000; Rozanska and Czerny 2000).

Here, we explore the possibility of explaining the X-ray emission from AGNs by the emission from the inner, effectively optically thin regions of a standard accretion disk with a luminosity close to the Eddington limit that cool down via the Comptonization of intrinsic thermal radiation. The existence of such regions was first shown but Shakura and Sunyaev (1973) and such models were later developed by Wandel and Liang (1991) and Beloborodov (1998). Clearly, this model cannot be universal, because not all AGNs with X-ray emission have luminosities close to the Eddington limit.

We computed X-ray spectra for these hot inner regions by taking into account relativistic effects and estimated the fundamental parameters of black holes (BHs) and ADs in 28 AGNs by fitting the observed X-ray spectra with computed theoretical spectra.

---

*E-mail: `vals@ksu.ru`

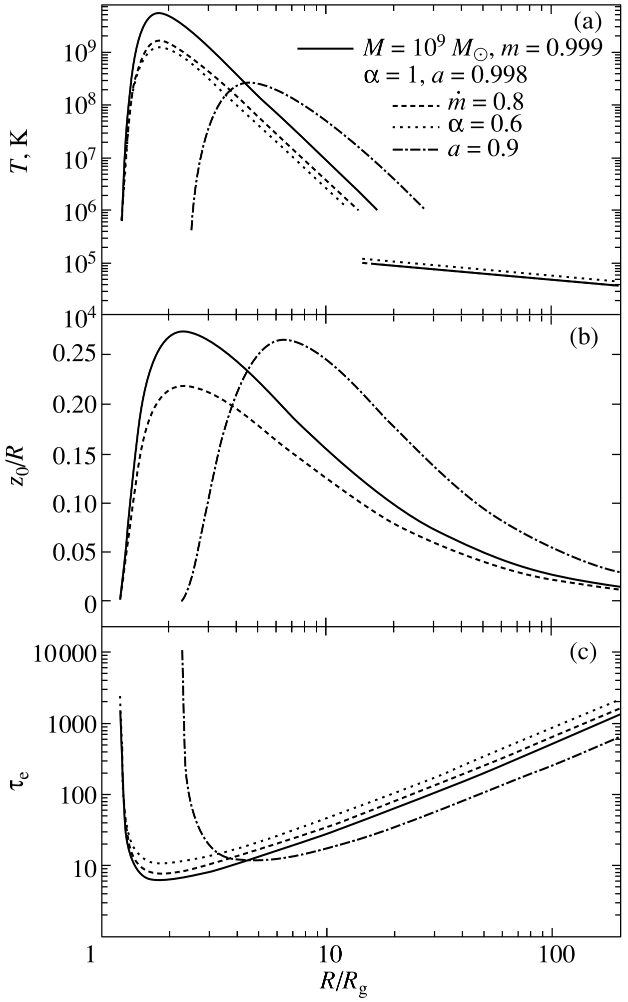

Fig. 1. The distributions of (a) temperature, (b) relative half-thickness, and (c) optical depth for electron scattering along the disk radius for models with various partameters. The temperature distributions for the basic model are indicated by solid lines. The remaining models here and in Figs. 3 and 4 have the same principal parameters of disk accretion as the basic model except for the indicated value of one of the parameters shown for the corresponding line.

THEORETICAL SPECTRA

To compute theoretical X-ray spectra for ADs around supermassive BHs, the following fundamental parameters must be specified: the BH mass M_x, the relative BH angular momentum a (Kerr parameter), the relative AD luminosity $L/L_{\rm Edd}$ (or the corresponding relative accretion rate $\dot{m} = \dot{M}/\dot{M}_{\rm Edd}$), the viscosity parameter α, and the cosine of the angle of disk inclination to the line of sight $\mu = \cos i$.

First, we computed a relativistic model for a standard AD (Shakura and Sunyaev 1973) by using the relativistic corrections from Riffert and Herold (1995). This model includes the distributions of effective temperature $T_{\rm eff}(R)$, surface density $u_0(R)$, and disk half-thickness $z_0(R)$ along the disk radius R. To this end, we solved the following equations:

the angular-momentum equation

$$2\pi W_{r\varphi} = \dot{M} w \frac{D}{A}; \tag{1}$$

the energy-balance equation

$$\sigma T_{\rm eff}^4 = \frac{3}{8\pi} w^2 \dot{M} \frac{D}{B}; \tag{2}$$

the viscosity equation

$$W_{r\varphi} = 2\alpha P z_0 \frac{A}{\sqrt{BC}}; \tag{3}$$

and the equation of hydrostatic equilibrium along the z axis

$$P = \frac{w^2 u_0 z_0}{4} \frac{C}{B}. \tag{4}$$

Here, $w = \sqrt{GM_x/R^3}$ is the Keplerian angular velocity at radius R, T is the parameter that characterizes the total radiation flux at a given disk radius, and P is the total pressure in the disk. Since we considered only those inner disk regions with the dominance of radiation pressure (the contribution of the gas pressure does not exceed 1%), we took the radiation pressure as the total pressure,

$$P \approx P_{\rm rad} = \frac{\sigma T_{\rm eff}^4 \sigma_{\rm e} u_0}{4c}, \tag{5}$$

where $\sigma_{\rm e} \approx 0.34$ cm^2 g^{-1} is the electron scattering coefficient in a hot plasma (with completely ionized hydrogen) of solar chemical composition. The contribution of the remaining opacity sources is negligible.

The relativistic corrections are defined in terms of the dimensionless geometric variables r and x expressed in units of the gravitational radius $R_{\rm g} = GM_x/c^2$ and the Kerr parameter:

$$A = 1 - \frac{2}{r} + \frac{a^2}{r^2},$$

$$B = 1 - \frac{3}{r} + \frac{2a}{r^{3/2}},$$

$$C = 3A - 2B,$$

$$D = \frac{1}{2\sqrt{r}} \int_{r_0}^{r} \frac{x^2 - 6x + 8a\sqrt{x} - 3a^2}{\sqrt{x}(x^2 - 3x + 2a\sqrt{x})}\, dx.$$

The dimensionless radius of the marginally stable orbit r_0 is defined by the following formulas (Page and Thorne 1974):

$$r_0 = 3 + Z_2 - [(3 - Z_1)(3 + Z_2 + Z_1)]^{1/2},$$

$$Z_1 = 1 + (1 - a^2)^{1/3}[(1 + a)^{1/3} + (1 - a)^{1/3}],$$

$$Z_2 = (3a^2 + Z_1^2)^{1/2}.$$

Next, based on the energy-balance equation, we calculated the temperature $T_e(R)$ at each radius of the inner hot region:

$$\sigma T_{\rm eff}^4 = L_{\rm ff} z_0 (1 + A'), \tag{6}$$

where $L_{\rm ff}$ is the rate of energy losses through free–free emission:

$$L_{\rm ff} = 5.35 \times 10^{-24} \left(\frac{u_0}{2 z_0 m_p}\right)^2 \times (kT_e({\rm keV}))^{1/2} \ \frac{\rm erg}{\rm s\ cm}.$$

The disk at a given radius was assumed to be homogeneous and isothermal along the z axis. In the accretion-disk region with a dominant radiation pressure, the disk is homogeneous in z coordinate (Shakura and Sunyaev 1973). When it cools down through the Comptonization of its intrinsic radiation, the temperature does not change greatly with depth, increasing to the surface (Sunyaev and Tilarchuk 1985), so the assumption that the disk is homogeneous and isothermal in z coordinate should not significantly affect the results. We use the amplification factor of the energy losses through Comptonization, A', in the form proposed by Svensson (1984):

$$A' = f(y_1) \frac{3}{4} \ln^2 \frac{2.35}{x_0}, \tag{7}$$

where

$$y_1 = \zeta \frac{\tau_e^2 \ln(1 + 4\theta + 16\theta^2)}{\ln(\theta / x_0)},$$

$$f(y_1) = 2\left(y_1^2 - (y_1 + y_1^2)\exp(-1/y_1)\right).$$

Here, $\theta = kT_e/m_e c^2$ is the dimensionless electron temperature and ζ is the geometric factor close to unity for a disk. The dimensionless frequency $x_0 = h\nu_0/kT_e$ corresponds to the frequency ν_0 at which the probabilities for photons to be absorbed via free–free processes and to undergo Compton scattering become equal (Kompaneets 1956; Illarionov and Sunyaev 1972), and $\tau_e = \tau_e u_0(R)/2$ is the disk optical depth for electron scattering.

Examples of computed temperature distributions for ADs with various parameters are shown in Fig. 1a. We restricted our analysis to regions with $T_e > 10^6$ K and did not use any interpolation formulas to describe the transition from effectively optically thin disk regions to effectively optically thick regions (see, e.g., Beloborodov 1998). The temperature distributions for effectively optically thick outer disk regions presented in the same figure are shown only for illustration. Figures 1b and 1c show the distributions of the relative half-thickness $z_0(R)/R$ and the optical depth for electron scattering $\tau_e = \sigma_e u_0(R)/2$ along the radius of the same disk models as those in Fig. 1a.

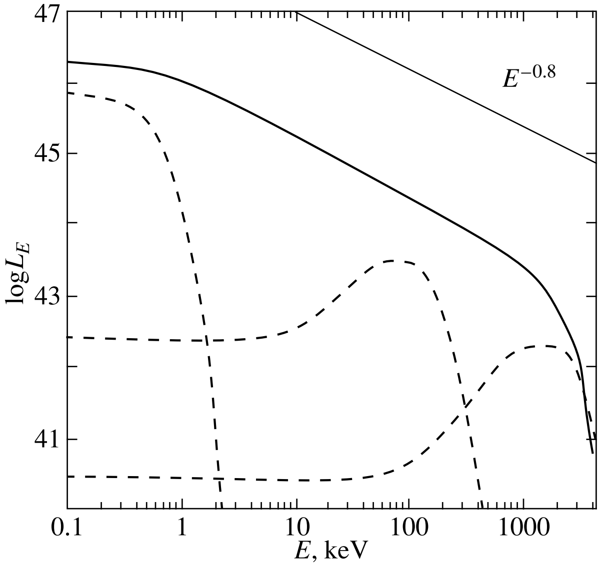

Fig. 2. The spectrum of the basic model and the local spectra of three rings in the hot region: with minimum (1.3×10^6 K), intermediate (3.3×10^8 K), and maximum (6.2×10^9 K) temperatures.

For each radius, the local spectrum $F_\nu(R)$ was computed from the known T_e and τ_e as the spectrum of a flat, homogeneous, isothermal layer, as prescribed by Sunyaev and Titarchuk (1980):

$$F_\nu = W \left(\frac{h\nu}{kT_e}\right)^{-\alpha_{\rm ST}} e^{-\frac{h\nu}{kT_e}} \times \int_0^\infty t^{\alpha_{\rm ST}-1} e^{-t} \left(t + \frac{h\nu}{kT_e}\right)^{\alpha_{\rm ST}+3} dt, \tag{8}$$

where

$$\alpha_{\rm ST} = \sqrt{\frac{9}{4} + \gamma} - \frac{3}{2}, \quad \gamma = \frac{\pi^2}{12} \frac{1}{\theta(\tau_e + 2/3)}.$$

The dilution factor W can be determined from the condition for the emergent flux at a given radius being equal to the theoretical flux:

$$\sigma T_{\rm eff}^4 = \pi \int_{\nu_0}^\infty F_\nu d\nu. \tag{9}$$

In this case, the Comptonization is saturated ($y = \tau_e^2 kT_e/(m_e c^2) > 1$) and the local spectra are Wien ones with the emission peak corresponding to the temperature at a given radius.

The resultant spectrum at infinity is the sum of the local spectra for rings with allowance made for their area and the relativistic radiative transfer function $T(\mu, R, \nu_0/\nu)$ that includes the relativistic Doppler

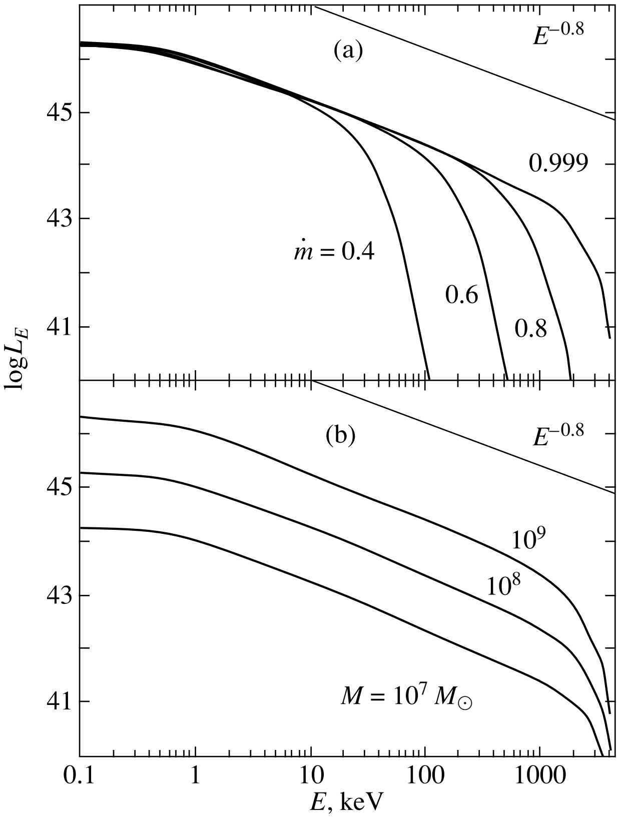

Fig. 3. Comparison of the model spectra for various relative disk luminosities (a) and BH masses (b).

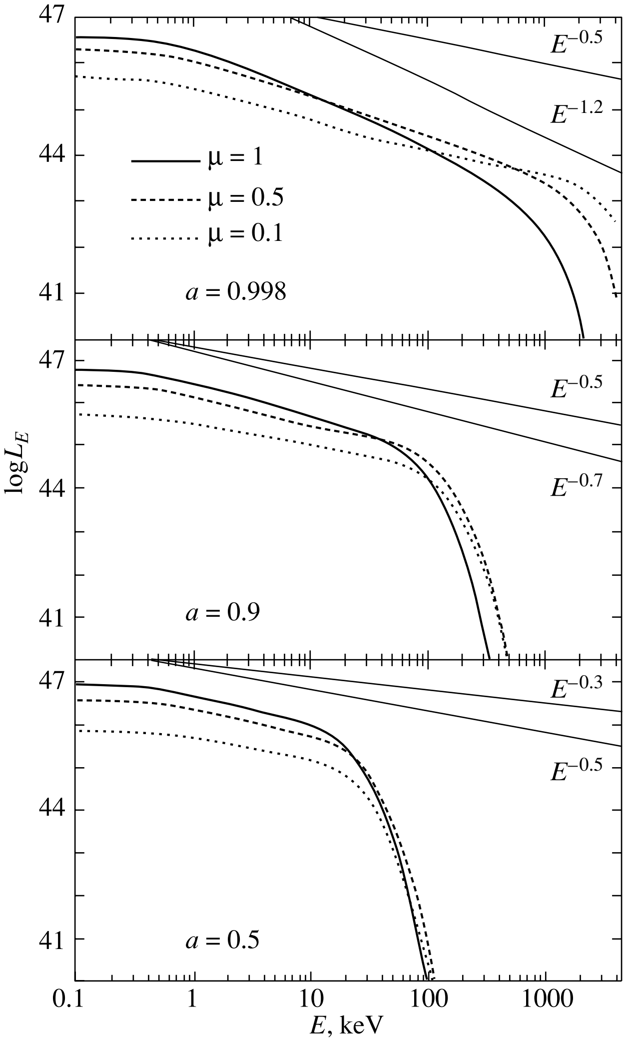

Fig. 4. Comparison of the model spectra with various values of the Kerr parameter for three different AD inclinations to the line of sight.

effect, the gravitational redshift, and the bending of light rays in the gravitational field (Laor *et al.* 1990):

$$L(\mu, \nu_0) = \int F_\nu(R) T\left(\mu, R, \frac{\nu_0}{\nu}\right) R\, dR\, d\left(\frac{\nu_0}{\nu}\right). \quad (10)$$

The relativistic transfer function also includes limb darkening according to the law of an electron scattering atmosphere.

Although the local spectra of the disk are Wien ones, its integrated spectrum proves to be a power law with an exponential cutoff at an energy corresponding to the maximum temperature in the disk in a wide energy range. An example of the integrated spectrum and the contribution of the local spectra for three disk rings to it are shown in Fig. 2.

The maximum temperature in the disk depends on its relative luminosity, the Kerr parameter, and the disk viscosity (α) (see Fig. 1a). Therefore, the high-energy spectral cutoff is at different energies for different values of these parameters. In particular, the cutoff energy must vary with disk luminosity (see. Fig. 3).

The gradient of the temperature distribution in hot disk regions depends weakly on the BH and AD parameters (see Fig. 1a) and the integrated spectral index α_x must be approximately the same ($\sim$0.75) for the spectra of all disks, irrespective of their parameters. However, because of the gravitational redshift, the relativistic Doppler effect, and the bending of light rays in the BH gravitational field, the spectral slope for a remote observer differs for different disk inclinations to the line of sight (see. Fig. 4).

FITTING TECHNIQUES AND RESULTS

The observed X-ray spectra of AGNs can be described by three parameters (without considering the excess of soft X-ray emission, the reflected component, and the lines): the spectral index α_x, the 2–10-keV luminosity L_{2-10} (we used $H_0 = 50$ km s^{-1} Mpc^{-1}), and the exponential-cutoff energy E_c. Analysis of theoretical spectra indicates that the luminosity L_{2-10} depends mainly on the BH

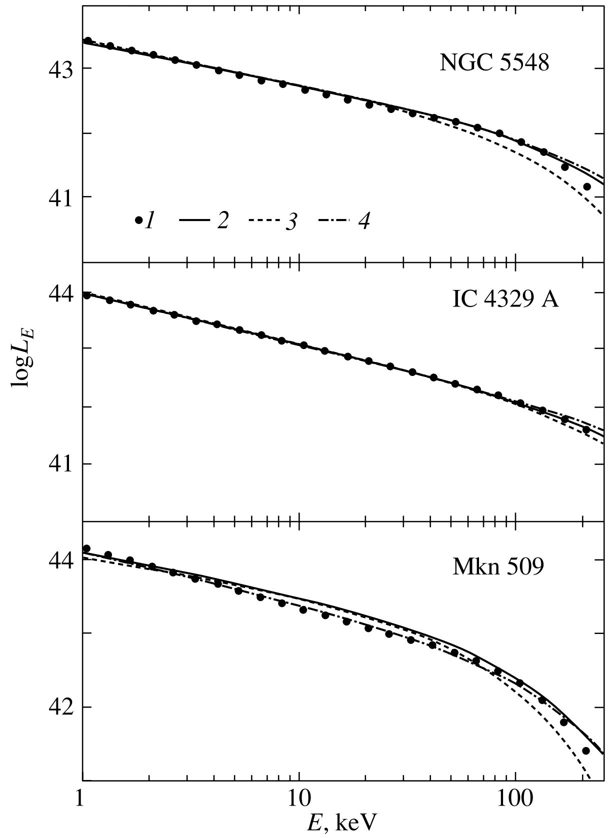

Fig. 5. Comparison of the theoretical spectra (*1*) with the best power-law fits with an exponential cutoff to the observed X-ray spectra (see the text) of three Seyfert galaxies (*2*). Also shown are the fits to the observed spectra with minimum (*3*) and maximum allowable parameters (*4*).

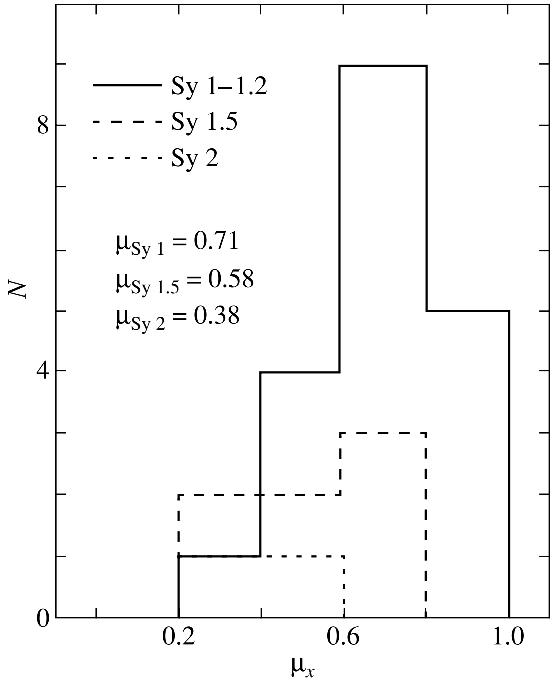

Fig. 6. The number of AGNs of various Seyfert types versus AD inclination to the line of sight.

mass M_x, because high-temperature states can exist only in a narrow range of the dimensionless parameters $\dot{m}$, α, and a (from $\sim$0.5 to 1). The energy $E_{\rm c}$ depends on these parameters. The spectral index α_x is determined mainly by the disk inclination to the line of sight and, to a lesser extent, by the Kerr parameter a (see Fig. 4).

We used the following fitting technique. The model spectra ($\sim$600 spectra) computed over a wide range of M_x, a, $\dot{m}$, α, and μ were fitted by a power law with an exponential cutoff in the observed X-ray energy range 2–250 keV. In this way, we determined the theoretical values of α_x, L_{2-10}, and $E_{\rm c}$; i.e., each set of five values of M_x, a, $\dot{m}$, α, and μ was associated with a triplet of α_x, L_{2-10}, and $E_{\rm c}$ values. Next, for the observed α_x, L_{2-10}, and $E_{\rm c}$, we determined all the triplets of theoretical values of the same quantities that matched the observed ones, to within their errors, and, hence, all the admissible values of the BH and AD fundamental parameters.

We chose 28 AGNs for our analysis. For these AGNs, either all three parameters of the X-ray spectrum or the masses of their central BHs $M_{\rm rev}$ determined from the lag between broad-emission-line variability and continuum variability are known. The observed parameters of the AGN spectra and the fitting results are presented in Tables 1 and 2. If only $E_{\rm c}$ estimates are known from observations, the corresponding values in Table 1 are given in parentheses. If $E_{\rm c}$ is not known from observations, it was assumed to be 200 keV. In both cases, the uncertainty in the cutoff energy was assumed to be 100 keV. Note that not all sources have the spectral index determined by taking into account the reflected component, which introduces an additional uncertainty into the derived AGN parameters. Examples of theoretical fits to the observed spectra are shown in Fig. 5. The spectra of the models with the parameters in Table 2 for these AGNs were used as the theoreticl spectra. In power-law spectra with an exponential cutoff with index α_x and cutoff energy $E_{\rm c}$ from Table 1 for these AGNs are shown as the observed spectra.

DISCUSSION

It follows from the fitting results (see Table 2) that, according to our model, BHs in AGNs are close to extreme rotation ($a \sim 1$). According to Thorne (1974), BHs cannot be spun up to $a > 0.998$ via accretion. However, since this theoretical result needs to be verified by observations, we also used models with large a. With a few exceptions, the spectra of almost

Table 1. Observed parameters of the spectra for the AGNs studied

Name	Type^1	$\lg L_{2-10}$	α_x	E_c, keV	$\lg L_{\rm bol}^{15}$	$\lg \nu L_\nu$, 60 μm^{15}
PG 0804+761	Sy 1.0	44.61^2	$0.43^{+0.77\ 2}_{-0.72}$	(200)	46.20	44.65
PG 0844+349	Sy 1.0	43.64^2	$1.02^{+0.07\ 2}_{-0.06}$	(200)	45.48^{14}	44.1^{14}
PG 0953+414	Sy 1.0 ?	44.85^2	$0.98^{+0.17\ 2}_{-0.15}$	(200)	–	–
PG 1211+143	Sy 1.0	43.96^2	$1.16^{+0.04\ 2}_{-0.08}$	(200)	46.07	44.69
PG 1411+442	Sy 1.0 ?	43.88^2	$1.26^{+0.78\ 2}_{-0.74}$	(200)	–	–
NGC 3227	Sy 1.5	42.01^3	0.52 ± 0.04^3	(200)	44.47	43.66
NGC 3516	Sy 1.5	43.43^3	$1.07^{+0.20\ 9}_{-0.08}$	$(350)^9$	44.66	43.55
NGC 3783	Sy 1.0	43.25^3	0.70 ± 0.08^9	$160^{+90\ 9}_{-60}$	44.73	43.88
3C 120	Sy 1.0	44.46^4	0.90 ± 0.03^4	$(400)^4$	45.58	44.50
3C 273	Sy 1.0	45.90^5	0.60 ± 0.06^5	$(500)^5$	47.45	46.04
3C 390.3	Sy 1.0	44.28^7	$0.80^{+0.05\ 6}_{-0.04}$	$380^{+\infty\ 6}_{-260}$	45.58	44.55^{16}
NGC 4051	Sy 1.5	41.56^3	0.92 ± 0.06^3	(200)	42.62	43.08
NGC 4151	Sy 1.5	42.97^3	0.35 ± 0.20^9	70 ± 20^9	44.22	43.20
NGC 4593	Sy 1.0	43.06^3	0.87 ± 0.05^9	$(250)^9$	–	–
NGC 4945	Sy 2.0+SB	43.48^8	0.6 ± 0.3^8	$140^{+170\ 8}_{-40}$	–	44.52^{16}
NGC 5548	Sy 1.5	43.76^3	$0.63^{+0.04\ 9}_{-0.03}$	$160^{+50\ 9}_{-70}$	45.04	43.77
NGC 7469	Sy 1.2	43.60^3	1.04 ± 0.05^9	$(330)^9$	45.36	45.21
Fairall 9	Sy 1.0	44.26^3	$1.05^{+0.11\ 9}_{-0.09}$	$(320)^9$	45.85^{14}	44.44^{14}
IC 4329A	Sy 1.2	44.20^{10}	0.86 ± 0.03^9	$270^{+170\ 9}_{-80}$	45.09	43.99
MCG-5-23-16	Sy 2.0	43.45^{11}	0.81 ± 0.05^{11}	130 ± 70^{11}	–	–
MCG-6-30-15	Sy 1.2	43.07^3	1.06 ± 0.03^9	$160^{+130\ 9}_{-60}$	–	–
MCG+8-11-11	Sy 1.5	44.02^{12}	$0.8 \pm 0.1^{12,13}$	$170^{+300\ 9}_{-80}$	45.29	44.49
Mkn 841	Sy 1.5	43.82^3	$0.75 \pm 0.2^{9,3}$	$(250)^9$	45.41	44.16
Mkn 110	Sy 1.0	44.15^2	0.73 ± 0.08^2	(200)	–	–
Mkn 335	Sy 1.0	43.41^2	$0.84^{+0.15\ 2}_{-0.16}$	(200)	45.39	43.58
Mkn 509	Sy 1.2	44.47^{12}	0.58 ± 0.1^{12}	$80^{+20\ 9}_{-30}$	45.76	44.61
Mkn 279	Sy 1.0	44.04^{17}	1.09 ± 0.05^{17}	(200)	45.32	44.34
Akn 120	Sy 1.0	44.15^{17}	1.08 ± 0.05^{17}	(200)	45.80	44.19

Notes: 1—NED (http://nedwww.ipac.caltech.edu), 2—George *et al.* (2000), 3—Nandra *et al.* (1997), 4—Eracleous *et al.* (2000), 5—Mineo *et al.* (2000), 6—Grandi *et al.* (1999), 7—Sambruna *et al.* (1999), 8—Guainazzi *et al.* (2000), 9—Matt (2001), 10—Perola *et al.* (1999), 11—Weaver *et al.* (1998), 12—Perola *et al.* (2000), 13—Grandi *et al.* (1998), 14—Elvis *et al.* (1994), 15—Mas-Hesse *et al.* (1995), 16—de Grijp *et al.* (1987), and 17—the ASCA database.

all AGNs proved to be consistent with the condition a $\leq$ 0.998. The spectral indices of AGNs with $a > 0.998$ were determined without considering the reflected component and their luminosities are much lower than the Eddington limit. Therefore, we cannot assert that $a > 0.998$ for BHs in these AGNs. The small error in Kerr parameter is determined by a strong dependence of this model on a near unity.

Analysis of the dependence of the derived AD inclinations in AGNs on their Seyfert type indicates that Sy 1–1.2 AGNs have, on average, larger inclinations to the line of sight (seen face-on) than Sy 1.5–

Table 2. Derived parameters of BHs and ADs in the AGNs studied

Name	M_x, $10^7 M_\odot$	$M^1_{\rm rev}$, $10^7 M_\odot$	$\log \dfrac{L_{\rm bol}}{L_{\rm Edd}}$	a	$\dot{M}/\dot{M}_{\rm Edd}$	μ_x
PG 0804+761	8.8 ± 4.8	$16.3^{+1.6}_{-1.5}$	-0.11	0.965 ± 0.035	0.75 ± 0.25	0.45 ± 0.25
PG 0844+349	0.72 ± 0.12	$2.7^{+1.1}_{-1.0}$	-0.05	0.9998	0.75 ± 0.15	0.8 ± 0.1
PG 0953+414	10.8 ± 2.8	$16.4^{+2.5}_{-3.0}$	–	0.995 ± 0.005	0.75 ± 0.1	0.75 ± 0.15
PG 1211+143	1.56 ± 0.2	3.2 ± 0.8	0.60	0.9998	0.86 ± 0.06	0.95 ± 0.05
PG 1411+442	1.8 ± 0.68	$8.8^{+3.3}_{-3.2}$	–	0.975 ± 0.025	0.72 ± 0.22	0.6 ± 0.4
NGC 3227	0.02 ± 0.01	$4.9^{+2.6}_{-4.9}$	-1.32	0.965 ± 0.035	0.78 ± 0.22	0.35 ± 0.15
NGC 3516	0.4 ± 0.2	$2.3^{+1.3}_{-1.0}$	-0.80	0.9998	0.84 ± 0.09	0.8 ± 0.05
NGC 3783	0.32 ± 0.16	$1.10^{+1.07}_{-0.98}$	-0.41	0.975 ± 0.025	0.75 ± 0.25	0.6 ± 0.3
3C 120	4.56 ± 0.16	$3.0^{+1.9}_{-1.4}$	0.006	0.9994 ± 0.0004	0.9 ± 0.1	0.6 ± 0.05
3C 273	144.0 ± 32.0	40 ± 20	0.76	0.975 ± 0.025	0.87 ± 0.12	0.4 ± 0.1
3C 390.3	2.92 ± 1.28	37^{+12}_{-14}	-1.09	0.985 ± 0.015	0.82 ± 0.18	0.65 ± 0.25
NGC 4051	0.006 ± 0.02	$0.14^{+0.15}_{-0.09}$	-1.63	0.9994 ± 0.0004	0.72 ± 0.12	0.75 ± 0.15
NGC 4151	0.292 ± 0.2	$1.2^{+0.83}_{-0.7}$	-0.96	0.95 ± 0.05	0.75 ± 0.25	0.3 ± 0.2
NGC 4593	0.18 ± 0.06	–	–	0.985 ± 0.015	0.8 ± 0.2	0.75 ± 0.25
NGC 4945	0.92 ± 0.12	$0.16^{+0.04}_{-0.04}$ [2]	–	0.965 ± 0.035	0.75 ± 0.25	0.25 ± 0.05
NGC 5548	0.88 ± 0.4	11 ± 3	-1.03	0.965 ± 0.035	0.78 ± 0.22	0.55 ± 0.15
NGC 7469	0.6 ± 0.12	$0.75^{+0.74}_{-0.75}$	0.39	0.9994 ± 0.0004	0.87 ± 0.13	0.85 ± 0.1
Fairall 9	2.72 ± 0.16	$8.3^{+2.5}_{-4.3}$	-0.17	0.9994 ± 0.0004	0.84 ± 0.09	0.8 ± 0.05
IC 4329A	2.40 ± 0.48	$0.7^{+1.8}_{-0.7}$	0.15	0.995 ± 0.005	0.75 ± 0.1	0.7 ± 0.15
MCG-5-23-16	0.60 ± 0.08	–	–	0.9994 ± 0.0004	0.57 ± 0.08	0.5 ± 0.15
MCG-6-30-15	0.18 ± 0.02	–	–	0.9994 ± 0.0004	0.8 ± 0.1	0.85 ± 0.1
MCG+8-11-11	1.56 ± 0.64	–	–	0.975 ± 0.025	0.8 ± 0.2	0.7 ± 0.3
Mkn 841	1.04 ± 0.44	–	–	0.975 ± 0.025	0.8 ± 0.2	0.6 ± 0.2
Mkn 110	2.24 ± 0.92	$0.77^{+0.28}_{-0.29}$	–	0.975 ± 0.025	0.8 ± 0.2	0.65 ± 0.25
Mkn 335	0.40 ± 0.16	$0.38^{+0.14}_{-0.10}$	0.71	0.975 ± 0.025	0.8 ± 0.2	0.65 ± 0.25
Mkn 509	4.4 ± 2.16	7.5 ± 2.5	-0.22	0.965 ± 0.035	0.77 ± 0.23	0.65 ± 0.25
Mkn 279	1.72 ± 0.2	4.2 ± 1.0 [3]	-0.4	0.9994 ± 0.0004	0.84 ± 0.09	0.95 ± 0.05
Akn 120	2.12 ± 0.36	$18.7^{+4.0}_{-4.4}$	-0.57	0.9994 ± 0.0004	0.8 ± 0.1	0.9 ± 0.1

Notes: 1—Kaspi *et al.* (2000), 2—Greenhill *et al.* (1997), and 3—Ho (1999).

and Sy 2 AGNs, in accordance with the unification scheme of activity. The distribution of AGNs in inclination (a histogram) for various Seyfert types is shown in Fig. 6. As was mentioned above, our model can only account for the X-ray emission from a high-luminosity (of the order of the Eddington limit) AGN. Therefore, the derived histogram, which also includes objects with luminosities below the Eddington limit, probably reflects the fact that the observed spectral slope of the X-ray source (irrespective of its nature) can be partly attributed to relativistic effects of the propagation of radiation from inner disk region to a distant observer.

The mass estimates for BHs in AGNs are of the greatest interest. Our masses M_x are compared with

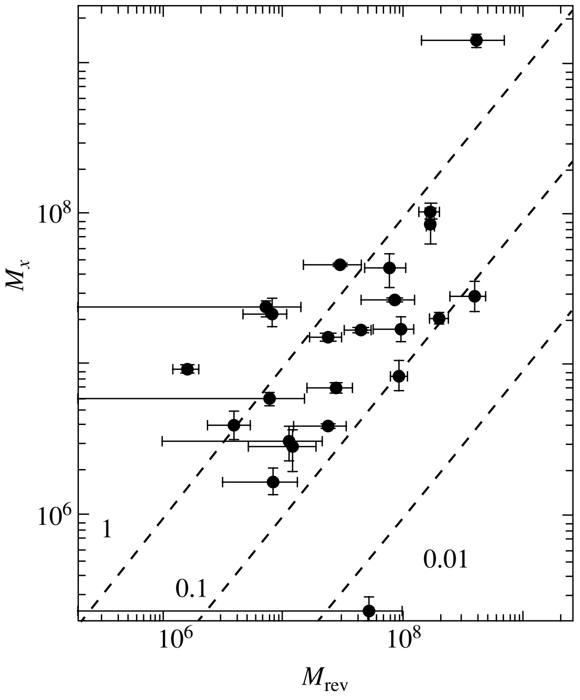

Fig. 7. Comparison of our BH masses M_x in AGNs with the masses $M_{\rm rev}$ determined from the lag between broad-emission-line variability and continuum variability. All masses are given in solar masses.

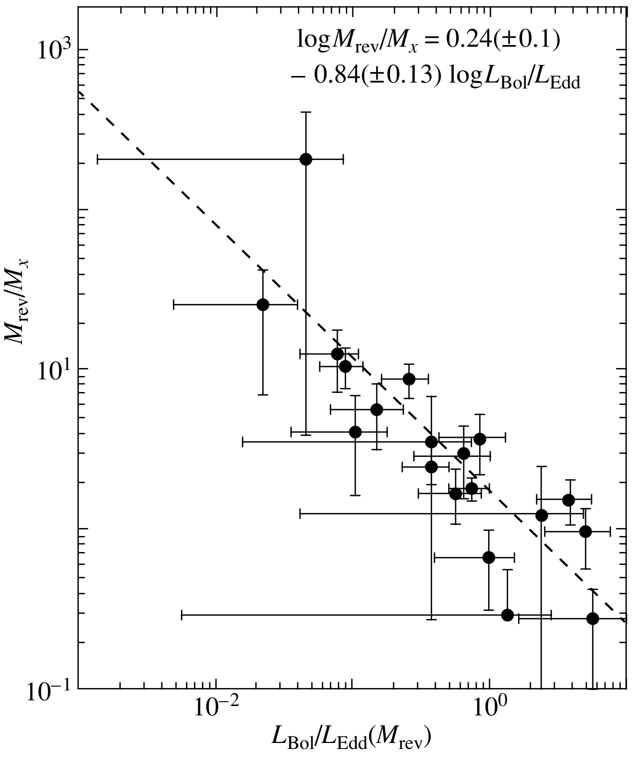

Fig. 8. $M_{\rm rev}/M_x$ ratio versus relative AGN luminosity.

the previously determined $M_{\rm rev}$ (Wandel *et al.* 1999; Kaspi *et al.* 2000) in Fig. 7.

Clearly, some of the AGNs have masses M_x comparable to $M_{\rm rev}$. However, most of our values are an order of magnitude lower; the lower is the relative AGN luminosity $L/L_{\rm Edd}(M_{\rm rev})$, the larger the $M_{\rm rev}/M_x$ ratio (see Fig. 8). The relation shown in Fig. 8 results from the fact that the luminosity in our model is assumed to be close to the Eddington limit and if the actual AGN luminosity were much lower than the Eddington limit, then our AGN mass M_x would be underestimated. This implies that, as we assumed from the outset, our model can be applied only to high-relative-luminosity AGNs and that the hot AD regions under consideration can contribute significantly to the X-ray emission from AGNs with luminosities close to the Eddington limit. The X-ray source of low-relative-luminosity AGNs must be different in nature.

In addition, the X-ray source under consideration may not be the only source even in high-relative-luminosity AGNs. Thus, our masses of two radio-bright AGNs, 3C 273 and IC 4329A, proved to be higher than their $M_{\rm rev}$. Since the masses in our model are determined mainly by the X-ray luminosity, this fact implies that another X-ray source, probably a jet, contributes to the X-ray flux from these two objects.

The inner radiation-dominated AD zones are known (Shakura and Sunyaev 1976) to be unstable. This raises the question of whether our model can be physically realized. However, more recent numerical calculations by Honma *et al.* (1991) showed that advection stabilizes the inner parts of the disk at high but still subcritical accretion rates ($\dot{m} \geq 0.5$). Since precisely such (or even higher) relative accretion rates are required for our model to be realized, we assume that our model can be realized for high-relative-luminosity AGNs. In subsequent papers, we plan to include advection in our model.

Let us consider the possibility of explaining other observed properties of the X-ray emission from AGNs in terms of our model. First, variations in the X-ray spectral slope and a change in the energy of the high-energy cutoff are observed in several AGNs. Whereas the change in cutoff energy can be explained by the relatively small change in accretion rate, the dependence of the the spectral slope on accretion rate is weak (see Fig. 3). However, the variations in spectral slope in a narrow energy range (2–20 keV) may be due to the variability of the reflected Compton component. Precisely this factor is responsible for the variability of the X-ray spectral slope in NGC 5548 (Nandra *et al.* 1991). In addition, the variations in spectral slope can be produced by the precession of the disk as a whole or of its inner parts.

The spectra of several galaxies exhibit a broad iron line with a mean half-width that corresponds to a velocity of 47 000 km s^{-1} (Nandra *et al.* 1997). For some galaxies, the line half-width reaches 100 000 km s^{-1}. Such velocities can be explained by the Keplerian rotation velocities of an AD in which the line originates at distances 10–40 R_g from the BH. In our model, the hot, completely ionized matter that produces power-law X-ray emission is located at distances of less than 10–15 R_g (see Fig 1a). At large radii, the disk is ionized incompletely ($T \sim 10^5$–10^6 K) and can emit an X-ray iron line with the observed half-width. The possibility that there is a system of relatively cold clouds above the disk plane up to its inner parts, which is an extension of the system of clouds responsible for the broad emission lines, cannot be ruled out either. In this case, the X-ray iron line and the reflected component can be emitted by this system of clouds. In addition, both the reflected component and the iron line can also be reemitted far from the central source. The BeppoSAX observations of the galaxy NGC 4051 in May 1998 (Guainazzi *et al.* 1998) revealed both the reflected component and the iron line, while the source of power-law emission was absent. This suggests that the sources of the reflected components in this galaxy lie far from the central source.

Since our model of the central X-ray source is not universal, its inconsistency with the observed properties of some AGNs cannot serve as evidence that it is invalid for all AGNs. But can we specify a property of this model that would serve as evidence that it it applicable to a specific active AGN? In our view, the detection of a correlation between the e-folding energy of the high-energy cutoff and the AGN luminosity at different observing epochs because of its variability (the higher is the luminosity, the higher the cutoff energy) for an AGN with a luminosity close to the Eddington limit could be such evidence.

CONCLUSIONS

We have attempted to compute the theoretical X-ray spectra for the inner, effectively optically thin parts of high-relative-luminosity ADs around supermassive BHs and to use them to describe the observed X-ray spectra of AGNs. We determined the fundamental parameters of BHs and ADs in 28 AGNs by fitting their X-ray spectra with the computed theoretical spectra.

We showed that, according to our model, the angular momenta of BHs in AGNs with a luminosity close to the Eddington limit are close to their extreme value and that the AD inclinations to the line of sight are in agreement with the unification scheme of activity.

Our BH masses M_x proved to be, on average, lower than those determined from the lag between line variability and continuum variability $M_{\rm rev}$; the lower the relative AGN luminosity $L/L_{\rm Edd}(M_{\rm rev})$, the larger the $M_{\rm rev}/M_x$ ratio. However, for AGNs with luminosities close to the Eddington limit, these differences are at a minimum and our model is applicable to them. The X-ray emission from a low-relative-luminosity AGN must be explained by other factors.

We discussed the fundamental possibility of explaining the reflected component and the iron line observed in the X-ray spectra of several AGNs in terms of our model.

ACKNOWLEDGMENTS

We wish to thank the referee for remarks that improved the quality of the paper. V. Suleimanov is grateful to the Russian Foundation for Basic Research (project no. 02-02-17174) for financial support and the University Space Research Association (USRA, USA) and M. Weisskopf, director of the Department of Space Research at the Marshall Space Flight Center (NASA), for hospitality and financial support during this study.

REFERENCES

1. A. M. Beloborodov, Mon. Not. R. Astron. Soc. **297**, 739 (1998).
2. G. S. Bisnovatyi-Kogan and S. I. Blinnikov, Astron. Astrophys. **59**, 111 (1977).
3. M. H. K. de Grijp, G. K. Miley, and J. Lub, Astron. Astrophys., Suppl. Ser. **70**, 95 (1987).
4. M. Elvis, B. J. Wilkes, J. C. McDowell, *et al.*, Astrophys. J., Suppl. Ser. **95**, 1 (1994).
5. M. Eracleous, R. Sambruna, and R. F. Mushotsky, Astrophys. J. **537**, 654 (2000).
6. I. M. George, T. J. Turner, T. Yaqoob, *et al.*, Astrophys. J. **531**, 52 (2000).
7. P. Grandi, F. Haardt, G. Ghisellini, *et al.*, Astrophys. J. **498**, 220 (1998).
8. P. Grandi, M. Guainazzi, F. Haardt, *et al.*, Astron. Astrophys. **343**, 33 (1999).
9. L. J. Greenhill, J. M. Moran, and J. R. Hernstein, Astrophys. J. Lett. **481**, L23 (1997).
10. M. Guainazzi, F. Nicastro, F. Fiore, *et al.*, Mon. Not. R. Astron. Soc. **301**, L1 (1998).
11. M. Guainazzi, G. Matt, W. N. Brandt, *et al.*, Astron. Astrophys. **356**, 463 (2000).
12. F. Haardt and L. Marashi, Astrophys. J. **413**, 507 (1993).
13. L. C. Ho, in *Observational Evidence for Black Holes in the Universe,* Ed. by S. K. Chakrabarti (Kluwer, Dordrecht, 1999), p. 153.
14. F. Honma, R. Matsumoto, Sh. Kato, and M. A. Abramovich, Publ. Astron. Soc. Jpn. **43**, 261 (1991).

15. A. F. Illarionov and R. A. Syunyaev, Astron. Zh. **49**, 58 (1972) [Sov. Astron. **16**, 45 (1972)].
16. S. Kaspi, P. S. Smith, H. Netzer, *et al.*, Astrophys. J. **533**, 631 (2000).
17. A. S. Kompaneets, Zh. Éksp. Teor. Fiz. **31**, 876 (1956) [Sov. Phys. JETP **4**, 730 (1957)].
18. A. Laor, H. Netzer, and T. Piran, Mon. Not. R. Astron. Soc. **242**, 560 (1990).
19. J. Mas-Hesse, P. M. Rodríguez-Pascual, L. Sanz Fernández de Cordoba, *et al.*, Astron. Astrophys. **298**, 22 (1995).
20. G. Matt, AIP Conf. Proc. **599**, 209 (2001).
21. F. Meyer, B. Liu, and E. Meyer-Hofmeister, Astron. Astrophys. **354**, L67 (2000).
22. T. Mineo, F. Fiore, A. Laor, *et al.*, Astron. Astrophys. **359**, 471 (2000).
23. R. Mushotsky, C. Done, and K. Pounds, Annu. Rev. Astron. Astrophys. **31**, 717 (1993).
24. K. Nandra, K. A. Pounds, G. C. Stewart, *et al.*, Mon. Not. R. Astron. Soc. **248**, 760 (1991).
25. K. Nandra, I. M. George, R. F. Mushotsky, *et al.*, Astrophys. J. **477**, 602 (1997).
26. D. N. Page and K. S. Thorn, Astrophys. J. **191**, 499 (1974).
27. G. Perola, G. Matt, F. Fiore, *et al.*, Astron. Astrophys. **351**, 937 (1999).
28. G. Perola, G. Matt, F. Fiore, *et al.*, Astron. Astrophys. **358**, 117 (2000).
29. H. Riffert and H. Herold, Astrophys. J. **450**, 508 (1995).
30. A. Rozanska and B. Czerny, Astron. Astrophys. **360**, 1170 (2000).
31. A. Rozanska, B. Czerny, P. T. Zycki, and G. Pojmanski, Mon. Not. R. Astron. Soc. **305**, 481 (1999).
32. R. Sambruna, M. Eracleous, and R. Mushorzky, Astrophys. J. **526**, 60 (1999).
33. N. I. Shakura and R. A. Sunyaev, Astron. Astrophys. **24**, 337 (1973).
34. N. I. Shakura and R. A. Sunyaev, Mon. Not. R. Astron. Soc. **175**, 613 (1976).
35. R. A. Sunyaev and L. G. Titarchuk, Astron. Astrophys. **86**, 121 (1980).
36. R. A. Sunyaev and L. G. Titarchuk, Astron. Astrophys. **143**, 374 (1985).
37. R. Svensson, Mon. Not. R. Astron. Soc. **209**, 175 (1984).
38. K. Thorne, Astrophys. J. **191**, 507 (1974).
39. A. Wandel and E. P. Liang, Astrophys. J. **380**, 84 (1991).
40. A. Wandel, B. Peterson, and M. A. Malkan, Astrophys. J. **526**, 579 (1999).
41. K. Weaver, J. Krolik, and E. Pier, Astrophys. J. **498**, 213 (1998).

Translated by V. Astakhov

Astronomy Letters, Vol. 28, No. 11, 2002, pp. 755–768. Translated from Pis'ma v Astronomicheskiĭ Zhurnal, Vol. 28, No. 11, 2002, pp. 840–854.
Original Russian Text Copyright © 2002 by Moiseev.

Two-Dimensional Spectroscopy of Double-Barred Galaxies

A. V. Moiseev[*]

Special Astrophysical Observatory, Russian Academy of Sciences,
Nizhnii Arkhyz, Karachai-Cherkessian Republic, 357147 Russia

Received May 29, 2002

Abstract—We describe the results of our spectroscopy for a sample of barred galaxies whose inner regions exhibit an isophotal twist commonly interpreted as a secondary bar. The line-of-sight velocity fields of the ionized gas and stars and the light-of-sight velocity dispersion fields of the stars were constructed from two-dimensional spectroscopy with the 6-m Special Astrophysical Observatory telescope. We detected various types of noncircular motions of ionized gas: radial flows within large-scale bars, counterrotation of the gas and stars at the center of NGC 3945, a polar gaseous disk in NGC 5850, etc. Our analysis of the optical and near-infrared galaxy images (both ground-based and those from the Hubble Space Telescope) revealed circumnuclear minispirals in five objects. The presence of an inner (secondary) bar in the galaxy images is shown to have no effect on the circumnuclear kinematics of the gas and stars. Thus, contrary to popular belief, the secondary bar is not a dynamically decoupled galactic structure. We conclude that the so-called double-barred galaxies are not a separate type of galaxy but are a combination of objects with distinctly different morphologies of their circumnuclear regions.

Key words: *galaxies, dynamics of galaxies, interstellar gas.*

1. INTRODUCTION

According to observational estimates, galaxies with central bars account for a major fraction (50–70%) of the total number of nearby disk galaxies (Selwood and Wilkinson 1993; Knapen *et al.* 2000b). The motion of stars and gaseous clouds within the bar differs markedly from unperturbed circular rotation; the radial flows of gas toward the center prove to be significant, as confirmed by direct observations (Afanasiev and Shapovalova 1981; Duval and Monnet 1985; Knappen *et al.* 2000a) and by numerous model calculations [see Lindblad (1999) for a review]. The central regions of such galaxies are decoupled in their dynamical parameters, star-formation rates, and densities of the gas and dust. For example, the molecular-gas density within the central kiloparsec in barred galaxies is an order of magnitude higher than that in unbarred galaxies (Sakamoto *et al.* 1999).

The dynamical effect of the bar is considered to be a major mechanism of the transportation of interstellar gas from the disk into the circumnuclear region, where it becomes fuel for a circumnuclear starburst or an active nucleus (Combes 2000). In the latter case, however, the relationship between the bar and the active (for a disk galaxy, Seyfert) nucleus is far from being unequivocal. Thus, the relative fraction of bars in Seyfert galaxies only slightly exceeds this fraction in galaxies without active nuclei (Knapen *et al.* 2000b). The main problem is that the gas in the bar is concentrated not in the nucleus itself, but in a ring of several hundred parsecs in radius, in the region of the inner Lindblad resonance. Therefore, an additional mechanism is required to take angular momentum away from the gas at a distance of 100–1000 pc from the centre and to transport the gas into the region where the gravitational forces of a central supermassive black hole are in action (Combes 2000). An elegant solution to the problem of mass transport to an active nucleus is the assumption made by Shlosman *et al.* (1989) that another bar can be formed in the gaseous disk (ring) within a large-scale bar that again produces flows of gas toward the nucleus. The system of two bars is capable of sweeping away the interstellar medium on scales of several kpc and of concentrating it at distances of 1–10 pc from the centre. Recently, this process was numerically simulated by Heller *et al.* (2001), although, in essence, the authors considered the evolution of the inner elliptical ring rather than the stellar–gaseous bar.

Increased interest in double bars stems from the fact that something like it is occasionally seen in the images of barred galaxies. Vaucouleurs (1975) detected a bar-like structure within the large-scale bar in NGC 1291. The first systematic observational study of a double-barred galaxy was undertaken by Buta and Crocker (1993). They published a list of

---

[*] E-mail: `moisav@sao.ru`

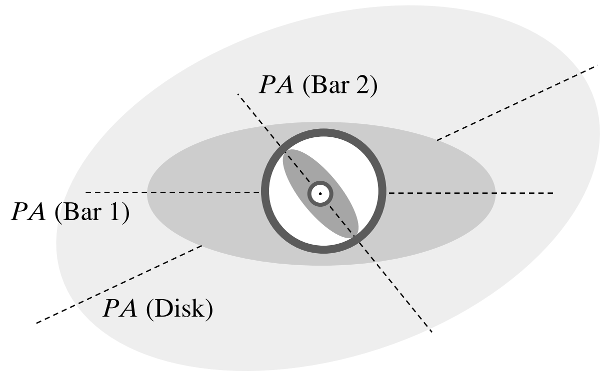

Fig. 1. A schematic view of a double-barred galaxy in projection onto the plane of the sky. The ring that corresponds to the region of the inner Lindblad resonance in the outer bar is highlighted. The principal isophotal orientations (see Subsect. 3.1) are indicated by dashed lines.

13 galaxies with an arbitrary orientation of the inner (secondary) bar relative to the outer (primary) bar. Analysis of the isophote shapes revealed secondary bars in the optical (Wozniak *et al.* 1995; Erwin and Sparke 1999) and infrared images of galaxies (Friedli *et al.* 1996; Jungwiert *et al.* 1997; Laine *et al.* 2002). An extensive bibliography and a list of 71 candidates for double bars compiled from literature are given in Moiseev (2001b).

Although there are now many papers on this subject, the dynamical behavior of such stellar configurations is still unclear. Maciejewski and Sparke (2000) showed that closed orbital loops maintaining the shapes of both bars that rotate with different angular velocities could exist. Similar independently rotating structures also occasionally appear in experiments on simulating stellar–gaseous disks (Pfenninger and Norman 1990; Friedli and Martinet 1993). The behavior of the gas in double bars was numerically analyzed by Maciejewski *et al.* (2002) and Shlosman and Heller (2002). Figure 1 shows the scheme of a galaxy with two independently rotating bars, which actually may be considered to be universally accepted.

It should be noted that, despite several interesting results obtained in numerical experiments, they are strongly model-dependent. Khoperskov *et al.* (2002b) showed that a secondary bar could periodically arise only at certain stages of the galaxy dynamical evolution; a long-lived secondary bar cannot yet be simulated (Friedli and Martinet 1993; Erwin and Sparke 2002). New observational data are required to verify contradictory theoretical predictions.

Numerous observational studies indicate that in the case of double bars, we probably come across a new structural feature of barred galaxies. However, the vast majority of these studies are based only on photometric data, when an extended structure is seen in the image of the galaxy within its primary bar (Fig. 2). Formal application of an isophotal analysis (Wozniak *et al.* 1995) even allowed several authors to distinguish triple bars (Jungwiert *et al.* 1997; Friedli *et al.* 1996; Erwin and Sparke 1999) without any reasoning on the dynamical stability of such configurations. However, the observed photometric structural features of such galaxies can also be explained in less exotic ways, without invoking secondary or third bars. An oblate bulge, an intricate distribution of star-forming regions and dust in the circumnuclear region, and an elliptical ring in the resonance region of the major bar can all create the illusion of a secondary bar in the galaxy images (Friedli *et al.* 1996; Moiseev 2001b). Kinematic data, i.e., measurements of the line-of-sight velocities and velocity dispersions of the gas and stars, are required to solve the problem. Since the observed objects are definitely not axisymmetric, two-dimensional spectroscopy can be of great help. It allows the two-dimensional distributions of line-of-sight velocities and their dispersions in the plane of the sky to be constructed.

In this paper, we discuss the results of the first systematic study of such galaxies by using the two-dimensional spectroscopy carried out in 2000–2002 with the goal to answer the following question: Are the secondary bars dynamically decoupled systems? Since the observational data themselves were described in detail by Moiseev *et al.* (2002), we discuss here only the most important features of the objects under study. The observing techniques are described in Section 2. In Section 3, we analyze the velocity and velocity dispersion distributions in the galaxies and describe the minispiral structures detected in the central regions of several galaxies. Our results are discussed in Section 4 and our main conclusion is formulated in Section 5.

2. OBSERVATIONS AND DATA REDUCTION

We drew our sample from the list of candidates for double bars (Moiseev 2001b) based on the convenience of their observation with the 6-m telescope: $\delta > 0°$; the diameter of the secondary bar fits into the MPFS field of view. Observational data were obtained for 13 galaxies, which account for about half of the total number of such objects in the northern sky. The table gives the name of the galaxy, its morphological type from the NED database, and the sizes of the apparent semimajor axes of the outer (a_1) and inner (a_2) bars in arcseconds with a reference to the corresponding papers.

All spectroscopic and some photometric observations were carried out with the 6-m Special Astrophysical Observatory telescope at $1-2''.5$ seeing.

Parameters of the observed galaxies

Name	Type	a_1	a_2	References to photometry
NGC 470	SAb	32″	8″	Wozniak *et al.* (1995); Friedli *et al.* (1996)
NGC 2273	SBa	24	8	Mulchaey *et al.* (1997)
NGC 2681	SAB0/a	29	5	Wozniak *et al.* (1995); Erwin and Sparke (1999)
NGC 2950	SB0	38	6	Wozniak *et al.* (1995); Friedli *et al.* (1996)
NGC 3368	SABab	24	4	Jungwiert *et al.* (1997)
NGC 3786	SABa	25	7	Afanasiev *et al.* (1998)
NGC 3945	SB0	42	20	Wozniak *et al.* (1995); Erwin and Sparke (1999)
NGC 4736	SAab	26	10	Shaw *et al.* (1993)
NGC 5566	SBab	24	6	Jungwiert *et al.* (1997)
NGC 5850	SBb	84	9	Buta and Crocker (1993); Wozniak *et al.* (1995)
NGC 5905	SBb	37	6	Wozniak *et al.* (1995); Friedli *et al.* (1996)
NGC 6951	SABbc	44	5	Wozniak *et al.* (1995)
NGC 7743	SB0	57	10	Wozniak *et al.* (1995)

The detector was a TK1024 CCD array. A log of observations and a detailed description of individual galaxies and the data reduction procedure were given by Moiseev *et al.* (2002).

The circumnuclear regions of all galaxies were observed with the Multipupil Field Spectrograph (MPFS) (Afanasiev *et al.* 2001). It simultaneously takes spectra from 240 spatial elements in the shape of square lenses that comprise a 16 × 15 matrix in the plane of the sky. The angular size of a single matrix element is 1″. The MPFS spectrograph is described on the Internet at http://www.sao.ru/~gafan/devices/mpfs/mpfs_main.htm. The observations were carried out in the spectral range λ4800–6100 Å and, for several galaxies, in the range λ5800–7100 Å; the dispersion was 1.35 Å per pixel. The covered spectral range included absorption features typical of the old (G–K-type) galactic stellar population. The line-of-sight velocity and velocity dispersion fields of the stars were constructed by using a cross-correlation technique modified for work with MPFS data (Moiseev 2001a). The line-of-sight velocities and velocity dispersions were determined with an accuracy of $\sim$10 km s^{-1}, on the average. Based on the MPFS observations, we also mapped the two-dimensional intensity distribution and the velocity field of the ionized gas in the Hβ, [O III] λ4959, 5007 Å and [N II] λ6548, 6583 Å emission lines. The line-of-sight velocities were measured with an accuracy of $\sim$10 km s^{-1}. No emission features were detected in NGC 2950 and NGC 5566. Six galaxies with intense emission features were observed with a scanning Fabry–Perot interferometer (FPI) in the 235th order of interference in a spectral region near the wavelength of the Hα line. The instrumental profile width was 2.5 Å ($\sim$110 km s^{-1}); the field of view was about 5′ with a scale of 0.56″–0.68″ per pixel. The instrument and reduction techniques were described previously (Moiseev 2002). We constructed the velocity fields of the ionized gas in Hα or [N II] λ6548, 6583 Å with an accuracy of $\sim$5 km s^{-1}.

The optical V- and R-band images of seven galaxies were obtained at the prime focus of the 6-m telescope using the SCORPIO focal reducer (its description can be found on the Internet at http://www.sao.ru/~moisav/scorpio/scorpio.html). The reducer field of view is 4′.8 with a scale of 0″.28 per pixel. In addition, we used the JHK-band images obtained with the 2.1-m OAN telescope in Mexico [for more detail, see Moiseev *et al.* (2002)]. We also used the galaxy images from the Hubble Space Telescope (HST) archive obtained with the Wide-Field and Planetary Camera (WFPC2) and with the Near-IR Camera (NICMOS).

As an example of the observational data used, Fig. 2 shows the images of NGC 2273 and NGC 2950, and Fig. 3 shows the velocity fields of the gas and stars and the velocity dispersion fields of the stars in NGC 2273, NGC 2950, and NGC 3945.

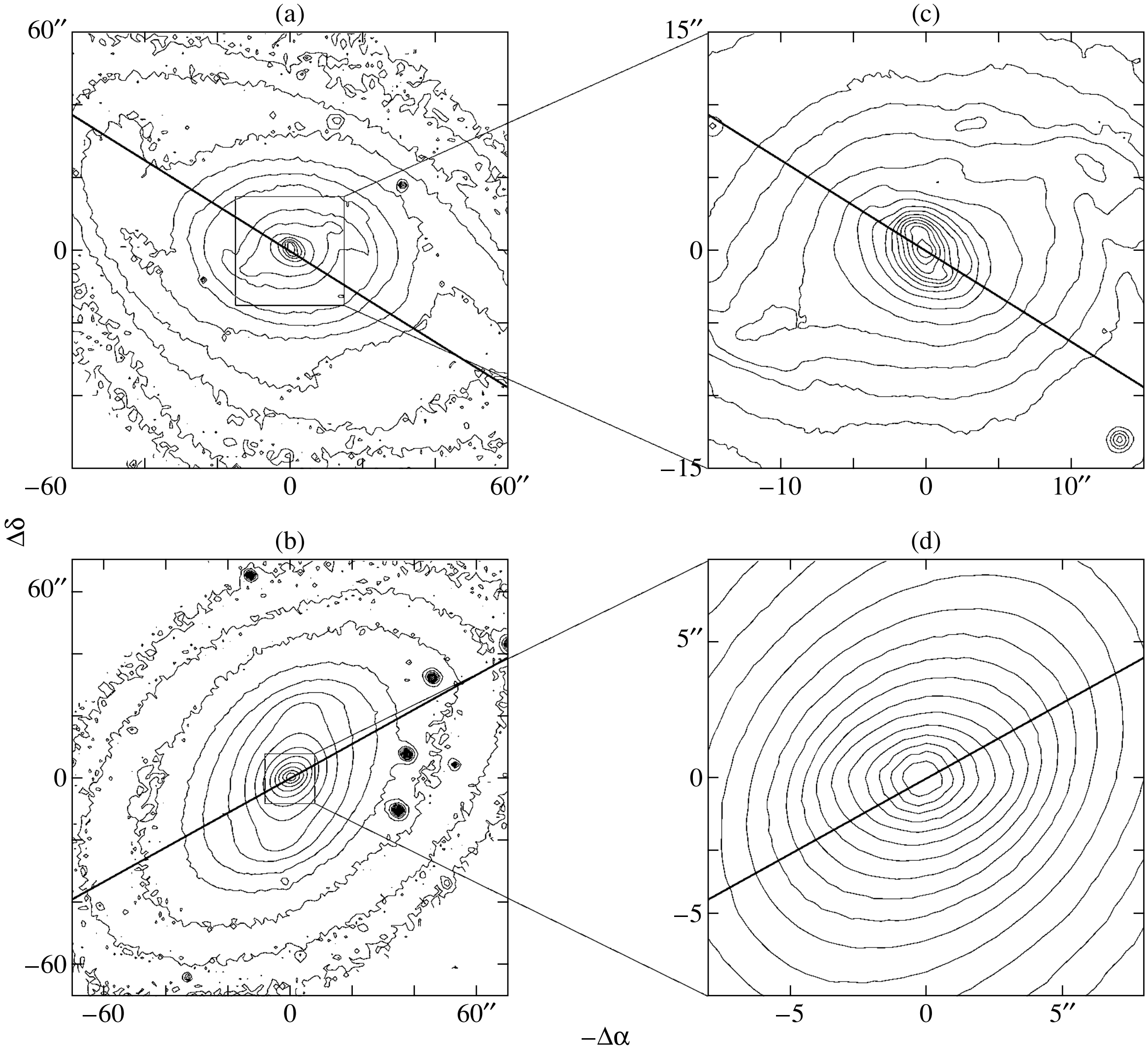

Fig. 2. The R-band images of (a) NGC 2273 and (b) NGC 2950 obtained with the 6-m telescope; (c) and (d) the enlarged central regions highlighted by the square in panels (a) and (b), respectively. The inner isophotal twist relative to the outer bars is clearly seen. The heavy lines indicate the orientation of the line of nodes of the disk.

3. ANALYSIS OF THE SPECTROSCOPIC AND PHOTOMETRIC OBSERVATIONS

3.1. Velocity Dispersion

The velocity dispersion distribution of the stellar disk is one of its important parameters. It allows unambiguous multicomponent models of the mass distribution in galaxies to be constructed (Khoperskov *et al.* 2002a). Numerical calculations show that because of the bar formation, the velocity dispersion distribution in the galactic disk differs greatly from the unperturbed (without a bar and spiral structure) axisymmetric case (Miller and Smith 1979; Vauterin and Dejonghe 1997). The bar is a much hotter dynamical subsystem; the velocity dispersion in it increases sharply. In addition, the velocity ellipsoid is found to be highly anisotropic. This anisotropy manifests itself in different distributions of the radial, azimuthal, and vertical velocity dispersions in the disk plane.

The model maps of the line-of-sight stellar velocity dispersion constructed for various disk and bar orientations (Miller and Smith 1979; Vauterin and Dejonghe 1997; Khoperskov *et al.* 2002b) indicate that the line-of-sight velocity dispersion (σ_*) distribution within the bar is symmetric about the bar major axis rather than about the disk major axis (line of nodes), as would be the case in the absence of a bar.

Unfortunately, the observational manifestations of the velocity-dispersion anisotropy in the σ_* distribution are fe in number. The series of papers by Kormendy (1982, 1983) are an example of the most consistent approach to measuring the velocity-dispersion anisotropy in barred galaxies. However, most authors

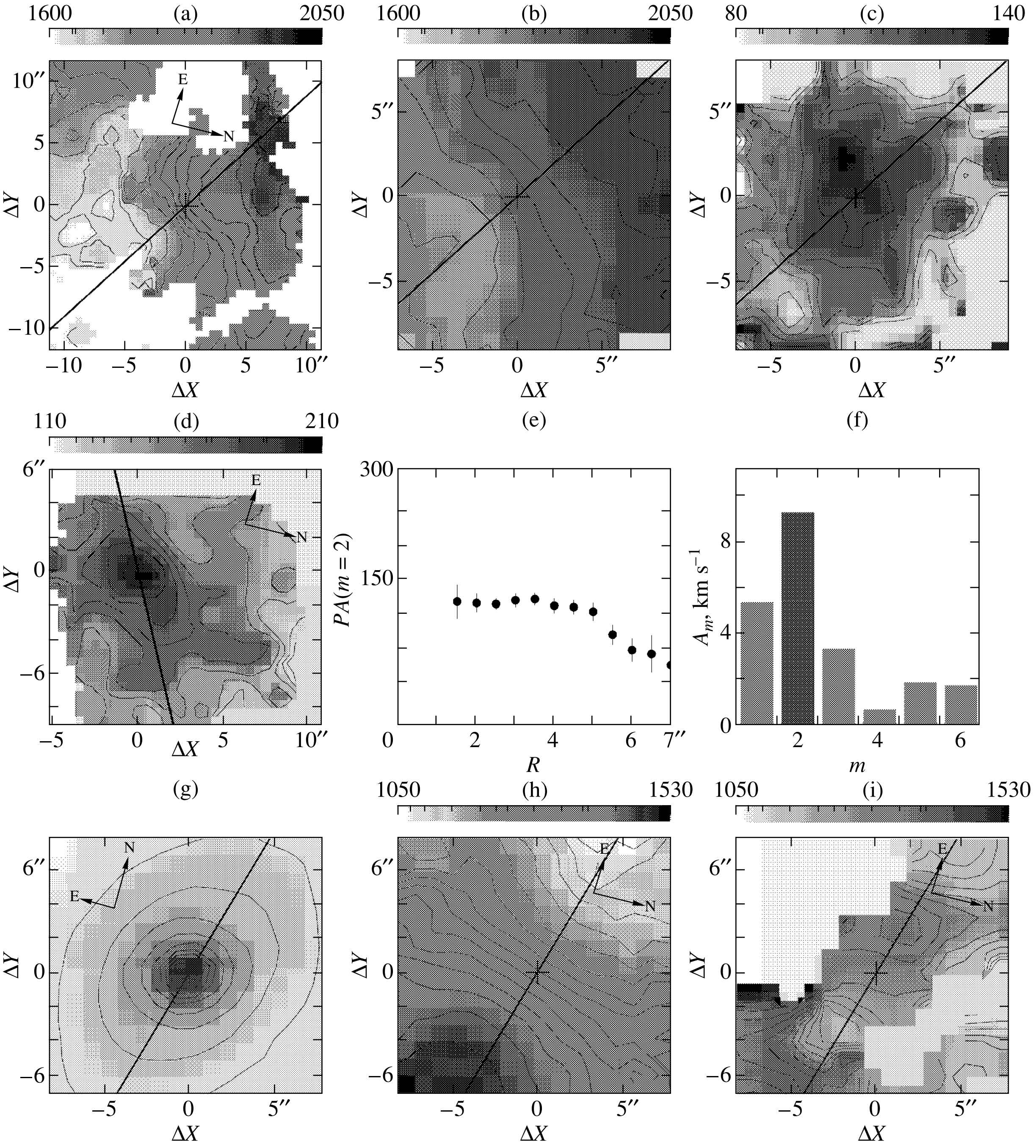

Fig. 3. Results of the observations of three galaxies. The gray scale is velocity in km s^{-1} and the heavy line indicates the orientation of the line of nodes everywhere. NGC 2273: (a) the gas velocity field constructed from Fabry–Perot observations; (b) and (c) the stellar velocity and velocity dispersion fields. NGC 2950: (d) the velocity dispersion field; (e) the radial dependence of the position angle of the maximum of the second harmonic in the Fourier spectrum σ_*; (f) the mean harmonic amplitude in the Fourier spectrum σ_*. NGC 3945: (g) the continuum MPFS image of the center; (h) the stellar velocity field; (i) the velocity field of the gas with counterrotation in the central region.

restrict themselves to measuring σ_* along one or two spectrograph slit directions. The two-dimensional σ_* maps used here are much more informative. Figures 3c and 3d show the isolines of the σ_* distribution that form ellipsoidal, elongated structures asymmetric about the disk line of nodes in the central regions of NGC 2273 and NGC 2950.

To quantitatively describe the deviation of the σ_* distribution from the axisymmetric case, we used the Fourier expansion of the observed velocity dispersion field in terms of position angle PA:

$$\sigma_*(r, PA) = A_0(r) + \sum_{m=1}^{N} A_m(r)\cos(m\,PA + \phi_m(r)), \tag{1}$$

where r is the distance from the center in the plane of the sky; A_m and ϕ_m are the amplitude and phase of the harmonic with number m, respectively; and $N = 6$–8 is the maximum number of harmonics. Our technique is similar to that used by Lyakhovich *et al.* (1997) to analyze the velocity fields but differs from it in that the Fourier expansion is made in terms of PA rather than in terms of the azimuthal angle in the galactic plane. In addition, it was shown in the above paper and in subsequent papers (see, e.g., Fridman *et al.* 2001) that for the velocity field of the gaseous disk in a spiral galaxy, the principal expansion harmonics are related to the spatial velocity vector components. For analysis of the σ_* fields, we cannot yet offer such a clear physical interpretation of the Fourier spectrum, if only because the combined contribution of the bulge and the disk with the bar is observed in the central regions under study. However, since our simulations indicate that the σ_* isolines in the bar form an ellipsoidal structure, this must correspond to a situation where the $m = 2$ harmonic and, possibly, the succeeding even harmonics have a maximum amplitude in (1). The direction of the major axis of this structure corresponds to the line of maximum of the second harmonic: $PA_2 = -\phi_2/2 \pm 180°$.

We broke down the velocity dispersion fields into rings with the center coincident with the photometric center of the continuum image. To provide a sufficient number of points in relation (1), each image element was broken down into four $0.5'' \times 0.5''$ elements. Experiments with analysis of various images show that this procedure introduces no significant distortions into the spectrum of the first harmonics, at least for $m < 4$–5. The position angle of the symmetry axis in the velocity dispersion distribution is defined as the mean value of the r dependence of PA_2, provided that there is a segment with an approximately constant PA_2 and that the second harmonic dominates in the Fourier spectrum at given r. For NGC 2950, this range of radii is $r = 1''$–$5''$ (Figs. 3e, 3f). The succeeding change in PA_2 at large distances stems from the fact that the galaxy does not lie exactly at the center of the MPFS field of view (Fig. 3d). Therefore, there are few pairs of diametrically opposite points in the velocity dispersion field for $r > 5''$, causing the spectrum of the even harmonics to be distorted.

The following three principal isophotal orientations can be distinguished in the image of a double-barred galaxy: the position angle of the disk, PA (disk), and the position angles of the bars, PA (Bar 1) and PA (Bar 2), shown in Fig. 1. According to the above considerations, if there are two dynamically independent bars, then each of these directions must be the symmetry axis in the apparent σ_* distribution on the corresponding distance scale. What actually determines the velocity dispersion distribution in the central region? To answer this question, we considered the relations between the position angle PA_2 of the symmetry axis of the velocity dispersion field and these three directions shown in Fig. 4. This figure shows data only for those seven objects from our sample in which the second harmonic dominates in the Fourier spectrum of the azimuthal σ_* distribution at $r = 1''$–$6''$. We see that in the galaxies under study, the direction PA_2 in the circumnuclear region ($r < 5''$–$6''$) coincides (within the error limits) only with the orientation of the outer bar and correlates neither with the major axis of the inner bar (Fig. 4c) nor with the line of nodes of the disk (Fig. 4a).

Since the central regions in galaxies of mostly early morphological types were observed (see the table), bulge stars must contribute significantly to the velocity dispersion. However, if the bulge is spherical, then it will affect only the amplitude of the zeroth harmonic, because expansion (1) is made in terms of the angle in the plane of the sky. If the bulge is oblate but axisymmetric (spheroidal), then this will cause an increase in the amplitude of the second harmonic. The line of its maximum must coincide with the line of nodes of the disk, because the symmetry of the observed σ_* distribution is similar to the case of a disk with a different apparent axial ratio. However, Fig. 4a shows no correlation between PA_2 and the line of nodes. If, alternatively, the bulge is triaxial, then it will produce an isophotal twist in the central region in projection onto the plane of the sky (Wozniak *et al.* 1995) and will be barely distinguishable from the inner bar. However, Fig. 4c shows no correlation between the symmetry direction of the velocity dispersion and the inner isophotal orientation.

Thus, the location of the line of maximum of the second harmonic in the Fourier expansion of the velocity dispersion field correlates only with the outer bar. This large-scale bar determines the dynamics of the stellar component even in those regions where the isophotal twist attributed to the secondary bar is observed.

3.2. Velocity Fields

We determined the radial dependences of the position angle of the dynamical major axis (the line of maximum line-of-sight velocity gradient) from the velocity field by the method of inclined rings (Begeman 1989). The velocity fields were broken down

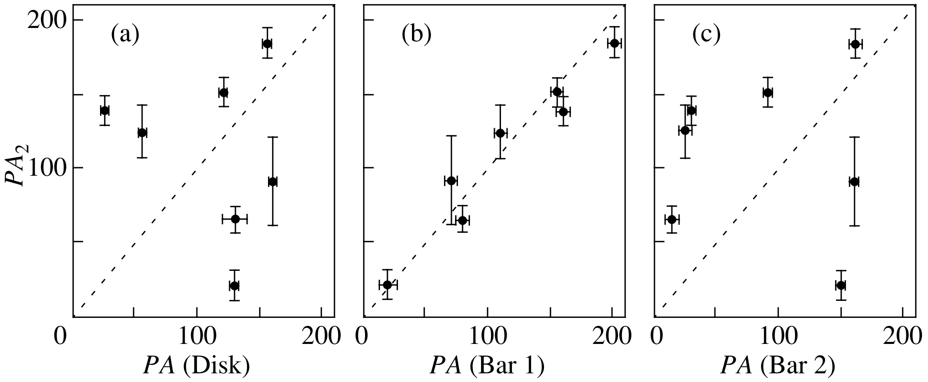

Fig. 4. Relation between the position angle of the second harmonic in the velocity dispersion distribution and the position angle of the disk (a) and the two bars (b) and (c). The dotted line represents a linear relation.

into elliptical rings about 1″ in width aligned with the outer galactic disk. In each ring, we determined the optimum dynamical position angle $PA_{\rm dyn}$ in the approximation of circular rotation (for more details, see Begeman 1989; Moiseev and Mustsevoi 2000).

The gaseous clouds move within the bar in such a way that the observed $PA_{\rm dyn}$ ceases to be aligned with the line of nodes of the disk (Chevalier and Furenlid 1978); the dynamical axis turns in a sense opposite to the line of nodes compared with the position angle of the inner isophotes (Moiseev and Mustsevoĭ 2000). In other words, the lines of equal line-of-sight velocities are elongated along the bar. A similar effect must also be observed in the stellar velocity field, as shown both by numerical simulations (Vauterin and Dejonghe 1997) and analytic calculations of the stellar dynamics in a triaxial gravitational potential (Monnet *et al.* 1992).

Figure 5 shows the radial dependences of the position angles of the dynamical axis and the major axis of the inner isophotes in several objects. We determined the isophotal orientation in NGC 2950 and NGC 3786 using the HST images obtained with the WFPC 2 camera through a F814W filter and with the NICMOS 1 camera through a F160W filter, respectively. The R-band image of NGC 5850 was taken from the digital atlas by Frei *et al.* (1996). In NGC 2950, the isophotal orientation changes by more than 50° (Fig. 5a), but $PA_{\rm dyn}$ for the stellar component is virtually aligned with the line of nodes. Neither the outer bar nor the inner bar have an appreciable effect on the stellar velocity field. This is probably because here, both stellar motions within the bar and the rotation of the bulge, whose contribution in this lenticular galaxy must be significant, are observed along the line of sight. Since the spectral resolution was too low to separate the two dynamical components in the line-of-sight velocity distribution (LOSVD), the mean velocity field corresponds to circular rotation. As was noted in Subsect. 3.1, the stellar component associated with the outer bar in NGC 2950 shows up in the distribution of the velocity dispersion, whose increase points to a broadening of the LOSVD in the bar region.

A similar pattern of stellar motion is observed in NGC 2273, NGC 3945, NGC 5566, NGC 5850, and NGC 5905. In four galaxies (NGC 470, NGC 2681, NGC 4736, and NGC 6951), there are significant (7°–20°) deviations of $PA_{\rm dyn}$ for stars from the line of nodes of the outer disk; these deviations of the dynamical axis are not related to the orientation of the inner bar but are in exactly the opposite direction compared with the isophotes of the outer bar. Here, as with the velocity dispersion, the stellar motions are affected by the outer bar rather than the inner bar, as should be the case for the model of independently rotating bars described in Sect. 1.

In NGC 3786, on the scale of the inner bar ($r < 6''$), $PA_{\rm dyn}$ deviates from the line of nodes by more than 10°; the deviations are in the opposite direction compared with the central isophotes (Fig. 5b). Here, we actually observe a dynamically decoupled central minibar about ~2 kpc in diameter. Its existence was first suspected by Afanasiev and Shapovalova (1981) when studying the gas kinematics in NGC 3786. In this galaxy, however, we cannot speak about a dynamically decoupled secondary bar, because a Fourier analysis of the surface-brightness distribution (Subsect. 3.3) indicates that the two-arm spiral mistaken by Afanasiev *et al.* (1998) for the outer bar is located in NGC 3786 at $r = 7''$–$20''$.

The situation in NGC 3368 is similar. A dynamically decoupled inner bar is observed in this galaxy, but the outer bar described by Jungwiert *et al.* (1997) is actually part of the spiral structure. The paper that describes in detail the structure and dynamics of NGC 3368 is being prepared for publication.

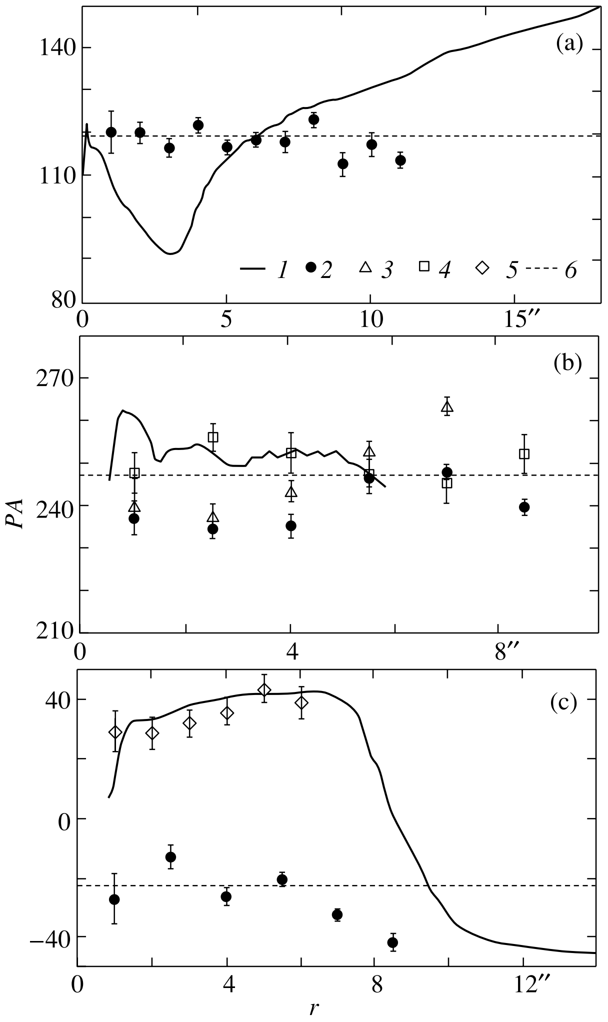

Fig. 5. The radial behavior of the position angle of the inner isophotes (*1*) and of the dynamical axis determined from stars (*2*) and from gas in the Hβ (*3*), [O III] (*4*), and [N II] (*5*) lines for (a) NGC 2950, (b) NGC 3786, and (c) NGC 5850); (*6*) the line of nodes of the outer disk.

The apparent kinematic behaviors of the ionized gas and stars in the objects under study are often different. Moreover, the ionized-gas velocities measured from permitted (Hα, Hβ) and forbidden ([O III], [N II]) lines can differ markedly. In NGC 3786, the dynamical axes in the stellar and gas velocity fields in H$_\beta$ are aligned, while the position angles measured from the velocities in the [O III] line systematically deviate from them (Fig. 5b). A similar effect is also observed in NGC 470, NGC 2273, NGC 5905, and NGC 6951. These deviations may be due to the presence at the bar edges of shock fronts produced when the disk gas interacts with the bar potential. The post-shock gas decelerates and emits in forbidden lines (Afanasiev and Shapovalova 1981). The following alternative explanation is also possible: neglected stellar absorption features distort the Hβ emission profile, which, in turn, introduces systematic errors into the gas line-of-sight velocity measurement. However, in galaxies with relatively intense emission features against the background of low-contrast absorption features, the velocity difference in forbidden and permitted lines in the bar region can be real.

In all the sample galaxies in which intense emission features were observed, the position angle $PA_{\rm dyn}$ measured from the gas is misaligned with the line of nodes of the outer disk, suggesting noncircular motions within the central kiloparsec. In five galaxies, the turn of the dynamical axis is not related to the isophotal twist in the inner bar. At the same time, it is in the opposite direction relative to the isophotes of the outer bar. This implies that the outer bar determines the dynamics of the gas component, while the inner bar is not dynamically decoupled.

The noncircular gas motions in the remaining six galaxies are different in nature. Thus, in NGC 3368 and NGC 3786, they are associated with the central minibar and there is no outer bar here, as was mentioned above. In NGC 6951, the noncircular gas motions are associated with the central minispiral, which is discussed in the next section.

In NGC 470, the dynamical center, defined as the symmetry point of the velocity field, is displaced by 4″–5″ (0.6–0.8 kpc) from the photometric nucleus of the galaxy, which may be due to the peculiar development of the azimuthal $m = 1$ harmonic in the gas velocity field (Emsellem 2002). This asymmetric harmonic can be generated by the tidal interaction with the nearby companion NGC 474, studied by Turnbull *et al.* (1999). The observed displacement of the center can also be explained as resulting from the development of an asymmetric harmonic in the surface-brightness distribution. As was pointed out by Zasov and Khoperskov (2002), this effect can be observed at certain evolutionary stages of barred galaxies.

The most peculiar galaxies (in terms of the gas kinematics) are NGC 3945 and NGC 5850. In the former, the gas line-of-sight velocities within 6″ (0.5 kpc) are close in maximum amplitude to the stellar velocities (80 and 120 km s^{-1}, respectively) but are opposite in sign! At large distances, the sense of rotation of the gas changes sharply and virtually coincides with that of the stars (Figs. 3h, 3i). The latter fact is also confirmed by the line-of-sight velocity measurements of the ionized gas with the FPI in several star-forming regions in the outer ring structure at distances 120″–140″ (10–11 kpc) from the center. It should be noted that such counterrotation of the gas and stars is occasionally observed in an early types galaxies; it is commonly attributed to the absorption of an outer gas cloud (Bertola *et al.* 1992; Kuijken *et al.* 1996).

The dynamical axis of the stars in the circumnuclear region of NGC 5850 is close to the line of nodes, while in the ionized gas, this axis deviates from it by more than 50°–60° (Fig. 5c) and is almost aligned with the position angle of the central isophotes. This behavior is typical of a disk inclined to the galactic plane (Moiseev and Mustsevoĭ 2000). In addition, if we, nevertheless, assume the gas motions to take place in the galactic plane, then it will turn out that they correspond to a radial outflow from the nucleus[1] with velocities 50–70 km s^{-1}. Such features are characteristic of Seyfert galaxies, but the optical spectrum of the galaxy contains no emission lines indicative of an active nucleus, nor are starbursts observed here (Higdon *et al.* 1998). A more reasonable assumption is that the gas moves at $r < 6''{-}7''$ in a plane polar to the galactic disk. In this case, the polar gaseous disk lies almost exactly along the small cross section of the outer bar. In recent years, such polar minidisks associated with a large-scale bar or a triaxial bulge have been detected in the circumnuclear regions of several galaxies, for example, in NGC 2841 (Sil'chenko *et al.* 1997; Afanasiev and Sil'chenko 1999) or NGC 4548 (Sil'chenko 2002). The hypothesis of a polar disk is also supported by the fact that, according to Higdon *et al.* (1998), NGC 5850 has undergone a recent collision with the nearby galaxy NGC 5846. Through their interaction, part of the gas could be transported to polar orbits.

3.3. Inner Minispirals

We used the HST archival images of the galaxies to study the detailed morphology of their circumnuclear regions. The models of mean elliptical isophotes were constructed by the standard technique and were subsequently subtracted from the original images. In five galaxies, the residual brightness distributions obtained in this way within their large-scale bars are in the shape of small spirals $5''{-}15''$ in size. A Fourier analysis of the azimuthal brightness distribution was used to quantitatively describe the detected spirals. The original images at each radius were expanded into the Fourier series (1), with the radius and the azimuthal angle in the galactic disk plane being substituted for r and PA, respectively. The derived Fourier spectrum allows us to determine both the number of arms of the principal spiral harmonic and the location of the line of its maximum amplitude. Examples of spirals, their residual brightnesses, and the mean harmonic amplitudes in three galaxies are shown in Fig. 6.

Three of the minispirals studied have already been described in the literature: the pseudoring in NGC 2273 (Ferruit *et al.* 2000) and the flucculent spirals in NGC 4736 (Elmegreen *et al.* 2002) and NGC 6951 (Pérez *et al.* 2000). Two new circumnuclear spirals were also found: the two-arm spiral in NGC 5566 and the three-arm spiral in NGC 7743. Based on an isophotal analysis of images, several authors (see references in the table) pointed out the existence of a secondary inner bar in these galaxies. Within the bar, the line of the maximum of the principal $m = 2$ azimuthal harmonic must be elongated along the corresponding constant azimuth. In NGC 5566, however, this line is wound into a spiral that runs from almost the very center and coincides with the residual-brightness peak (Fig. 6b); i.e., a minispiral rather than a bar is located here, with its shape resembling the outlines of the spirals within the bars obtained in the model calculations by Englmaier and Shlosman (2000). The minispiral shown in Fig. 6b lies within a large scale bar with a semimajor axis of about $30''$ ($\sim$3 kpc).

In NGC 3786, the line of maximum of the $m = 2$ harmonic at $r < 5''{-}6''$ has a constant azimuthal angle, which is a further confirmation of the existence of a minibar whose dynamical manifestations are described in Subsect. 3.2. Far from the center, this line is wound into a regular spiral that coincides with the global two-arm pattern in the galactic disk at $r = 20''{-}30''$. The Fourier spectrum is dominated by the second harmonic; the $m = 1$ harmonic is similar in amplitude to it (Fig. 6a). Clearly, the large relative amplitude of the first harmonic can be explained in terms of asymmetry in the apparent distribution of the dust lanes, most of which lie on the near side of the NGC 3786 disk. A similar effect was described by Fridman and Khoruzhii (2000) when performing a Fourier analysis of the images for NGC 157. The spirals, defined as the maximum of the $m = 2$ harmonic near the bar ends, change their winding direction (Fig. 6a). According to Fridman and Khoruzhii (2000), this behavior must suggest that the bar is slow (in terms of the angular velocity of rigid rotation). For the nature of the minibar in NGC 3786 to be eventually elucidated, we must have a more detailed gas velocity field than that used here.

Wozniak *et al.* (1995) detected an isophotal twist at $r < 5''{-}6''$ in the ground-based optical images of NGC 6951 within its outer bar $r \approx 60''$ in size, which they interpreted as an inner bar. However, based on near-infrared photometry, Friedli *et al.* (1996) questioned this interpretation by assuming that the isophotal twist could result from a complex distribution of dust and star-forming regions within the central kiloparsec. Indeed, the HST images exhibit a ring of star-forming regions that is elliptical in the

---

[1] Here, we use the suggestion made by Higdon *et al.* (1998) that the disk orientation of the galaxy for which its western half is closest to the observer is most probable.

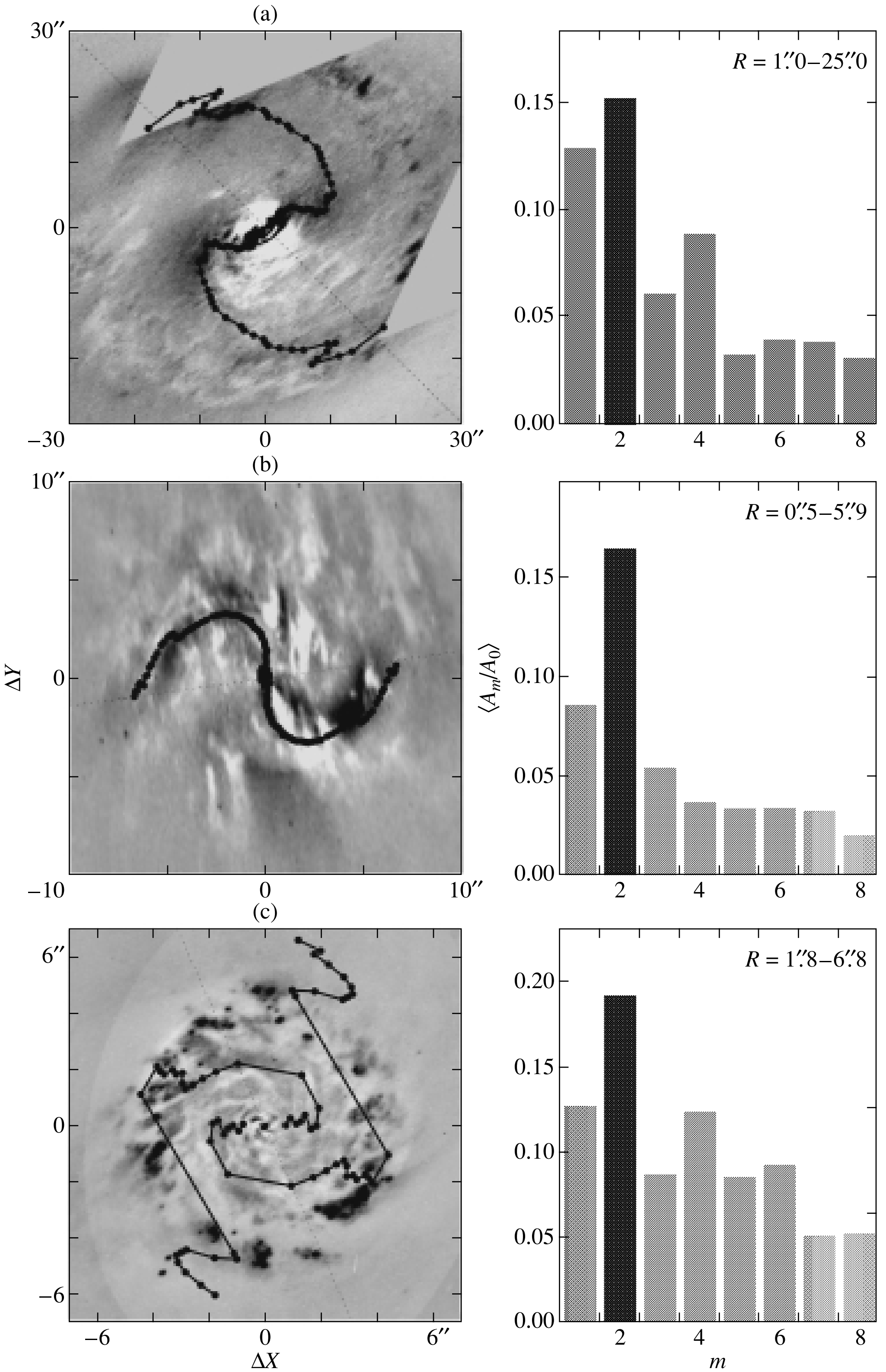

Fig. 6. The spiral patterns seen in the HST images (F606W filter): (a) NGC 3786, (b) NGC 5566, and (c) NGC 6951. The maps of residual brightnesses in the galactic plane with the lines of maximum of the second harmonic in the brightness distribution superimposed on them are shown on the left. The mean harmonic amplitude normalized to A_0 is shown on the right; the range of radii (R) in which the averaging was performed is indicated.

plane of the sky but is almost circular in the galactic plane (the inclination of the galactic plane to the line of sight was assumed to be 42°, in agreement with the data of Pérez *et al.* (2000). These high-resolution images confirm the absence of a bar as an elongated, ellipsoidal structure. The $m = 2$ harmonic dominates in the Fourier spectrum within the ring of star formation, but, in contrast to NGC 3786 and NGC 5566, the line of its maximum consists of separate fragments of the spirals. This is also true for higher harmonics, which, however, have a sufficiently high amplitude (Fig. 6c). If we draw an analogy with the universally accepted classification of large-scale spiral arms, then a grand design is observed in NGC 3786 and NGC 5566 and flocculent spirals are observed in NGC 6951 and NGC 4736. However, the minispiral in NGC 6951 differs from the large-scale spirals in disk galaxies in that the multi-arm spiral seen in the residual-intensity distribution (Fig. 6c) is probably associated only with the distribution of gas and dust rather than with the stellar component. As was shown by Pérez *et al.* (2000), this inner spiral structure clearly seen in the V band completely disappears in the H band, where the effect of dust absorption is much weaker.

Interestingly, the position angle of the dynamical axis constructed from the ionized-gas velocity field in the Hα and [N II] lines at $r = 0''-8''$ deviates by $10°-15°$ from the line of nodes of the outer disk, suggesting a significant role of noncircular motions. Since there is no inner bar here, we can offer the following interpretation of the observed pattern. There is a gas-and-dust disk $6''-8''$ (400–600 pc) in radius within the large-scale bar in which a multi-arm spiral structure perturbing the circumnuclear gas rotation develops. The dynamical decoupling of this disk is also confirmed by a high molecular-gas density (Kohno *et al.* 1999) and by the location of two inner Lindblad resonances of the large-scale bar here[2] (Pérez *et al.* 2000).

Presently, minispirals have been detected in the circumnuclear regions of many galaxies (Carollo *et al.* 1998), but as yet no unequivocal interpretation of the nature of their formation has been offered [see Elmegreen *et al.* (2002) for more details]. One of the reasons why the theoretical interpretations have failed seems to be the scarcity of reliable data on the observed kinematics of such spirals. The papers on this subject are still few in number (Laine *et al.* 2001; Schinnerer *et al.* 2002) and from this point of view, measurements of the gas velocities at the center of NGC 6951 can be of interest in their own right.

4. DISCUSSION

The main motive for this study is the search for any common features in the kinematic manifestations of bar-within-bar structures in an attempt to prove that the secondary bar is dynamically decoupled. A similar attempt has recently been also made by Emsellem *et al.* (2001), who presented the results of their study of stellar motions in four southern-sky galaxies. Using the method of classical spectroscopy, Emsellem *et al.* (2001) concluded that the inner bars were decoupled in three objects based only on the existence of a circumnuclear line-of-sight velocity peak in long-slit cuts. However, such features can also be explained in terms of more natural factors, such as a peculiar mass distribution in the disk and the bulge or noncircular motions in the outer bar, without invoking the hypothesis of a secondary bar. Observations of two-dimensional kinematics, which allow the pattern of noncircular gas and stellar motions to be determined, could give a more definitive answer. The results obtained in this way appear all the more unexpected.

First, the shape of the line-of-sight stellar velocity dispersion distribution (Subsect. 3.1) is determined only by the outer bar and does not depend on the relative position of the inner bar-like structure. Second, either noncircular motions typical of the outer bar or good agreement with circular rotation are observed in the stellar velocity fields; the latter is, probably, explained by the fact that here, the line-of-sight stellar motions in the bar and the bulge are added together (Subsect. 3.2). Finally, the ionized-gas velocity fields everywhere point to the presence of noticeable noncircular motions. However, they either correspond to the outer bar (as suggested by from analysis of the radial behavior of $PA_{\rm dyn}$) or are associated with the inner spiral structure (NGC 6951) or with another individual peculiar features of the galaxy (NGC 470, NGC 3945, and NGC 5850). Thus, it turns out that the secondary inner bar seen in the galaxy images does not affect the observed kinematics of the gas and stellar components in all the sample objects.

This conclusion is in conflict with the popular opinion of a dynamically independent secondary bar, which is based on analysis of isophotal shapes and on model calculations (Sect. 1). Maybe the methods used here and the limited spatial resolution do not allow the kinematic features of the small-scale inner bar to be evaluated. However, this is not the case, because the minibars in NGC 3368 and NGC 3786 do not differ in their apparent sizes from the secondary bars in the remaining galaxies (see the table), but the features of noncircular gas and stellar motions associated with them are clearly detected. In this case, our photometric analysis suggests that there is no outer bar in these two galaxies (Subsects. 3.2 and 3.3).

---

[2] When the paper was submitted for publication, the paper by Rozas *et al.* (2002) appeared. Based on their own FPI observations, these authors reached a similar conclusion regarding the nature of the inner disk in NGC 6951.

The three galaxies with the most peculiar features in the observed gas motions should be considered separately. Although the asymmetric $m = 1$ mode developed within the bar of NGC 470 and the polar gaseous disk in NGC 5850 are rare structures, they, nevertheless, were observed by several authors in other objects as well (see Subsect. 3.2). It was also noted in this subsection that the two galaxies have close massive companions. Therefore, the assumption that the features of their gas kinematics result from the interaction with the companions appears reasonable enough.

According to Kuijken *et al.* (1996), the gaseous disks in lentucular (S0) galaxies exhibit counterrotation relative to the stars in $24 \pm 8\%$ of the cases[3]; i.e., this is a common phenomenon that is, probably, attributable to absorption of the fallen gaseous cloud with the corresponding direction of angular momentum (Bertola *et al.* 1992). Against this background, the gas counterrotation at the center of NGC 3945, one of the four S0 galaxies in our sample (table) with gaseous disks observed in three of them (NGC 2681, NGC 3945, and NGC 7743), comes as no surprise.

The presence of minispirals in some galaxies is not surprising either. Thus, Erwin and Sparke (2002) found that their sample of early-type (S0–Sa) barred galaxies contained $24 \pm 7\%$ of objects with circumnuclear minispirals, which is slightly less than the $39 \pm 14\%$ (5 of 13) in the sample under study. Although the difference between the frequencies of occurrence of minispirals is within the error limits, it can be easily explained in terms of the selection effect in the sample of galaxies with inner isophotal twists. The inner spirals distort the central isophotes, which may lead to the wrong conclusion that there is a secondary bar.

Having studied the detailed kinematics of the gas and stars in the galaxies from our sample, we may conclude that the so-called double-barred galaxies are not a separate type of galaxy but are a combination of objects with distinctly different structures of their circumnuclear regions. The formal use of isophotal analysis of images to study galaxies without invoking kinematic data can lead to erroneous conclusions. We think that the double-barred galaxies described in the literature can be arbitrarily divided into two basic classes. The first class includes early-type (S0–Sa) galaxies. Here, the illusion of a secondary bar results from the triaxial bulge shape. In contrast to the bar, the triaxial bulge has virtually no effect on the disk dynamics in the circumnuclear region; a characteristic example is NGC 2950. The second class includes galaxies of later types. Here, decoupled gas-and-dust disks with a minispiral structure distorting the isophotal shape can be observed within large-scale bars; a characteristic example is NGC 6951. There is also a third possibility: the so-called x_2 family of stable orbits oriented perpendicular to the bar major axis can exist within a large-scale bar (Contopouls and Grosbol 1989). A bar-like structure that is exactly perpendicular to the primary bar and that correspondingly distorts the observed isophotes can be formed on the basis of these orbits. Such a model was proposed for NGC 2273 (Petitpas and Wilson 2002). In this case, however, there is no decoupled secondary bar, but there is a feature in the inner structure of the major bar that rotates with it as a whole.

5. CONCLUSIONS

A number of contradictions between existing models of nested bars and observations can be resolved by abandoning the popular view of dynamically independent double bars, which we propose here. Many models suggest that the secondary bar is a short-lived structure, which, in turn, is in conflict with common observations of inner isophotal twists [see Erwin and Sparke (2002) for more details]. However, everything falls into place if these twists are not associated with the secondary bars, at least in most of these galaxies. On the other hand, the fact that, according to statistical data, the photometric secondary bar is in no way associated with the presence of an active nucleus in the galaxy can be explained (Laine *et al.* 2002; Erwin and Sparke 2002), although it is clear from theoretical considerations that the correlation here must be much closer than that for single bars. The reason is that the secondary bar traceable by isophotal twists is not a dynamically decoupled structure in the galaxy at all.

ACKNOWLEDGMENTS

I wish to thank V.L. Afanasiev for interest and helpful discussions and N.V. Orlova for help in preparing this article. This study is based on observational data obtained with the 6-m Special Astrophysical Observatory telescope financed by the Ministry of Science of Russia (registration no. 01-43) and on HST NASA/ESA data taken from the archive of the Space Science Telescope Institute operated by the Association of Universities for Research in Astronomy under a contract with NASA (NAS 5-26555). In the work, was used the NASA/IPAC (NED) Extragalactic Database operated by the Jet Propulsion Laboratory of the California Institute of Technology under a contact with the National Aeronautics and Space Administration (USA) and

---

[3] In what follows, the errors are given at a 1σ level of the binomial distribution.

the HYPERCAT database (France). The study was supported by the Russian Foundation for Basic Research (project nos. 01-02-17597 and 02-02-06048mas) and the Federal Program "Astronomy" (project no. 1.2.3.1).

REFERENCES

1. V. L. Afanasiev and A. I. Shapovalova, Astrofizika **17**, 403 (1981).
2. V. L. Afanasiev and O. K. Sil'chenko, Astron. J. **117**, 1725 (1999).
3. V. L. Afanasiev, V. P. Mikhailov, and A. I. Shapovalova, Astron. Astrophys. Trans. **16**, 257 (1998).
4. V. L. Afanasiev, S. N. Dodonov, and A. V. Moiseev, in *Stellar Dynamics: From Classic to Modern,* Ed. by L. P. Osipov and I. I. Nikiforov (St. Petersburg, 2001), p. 103.
5. K. G. Begeman, Astron. Astrophys. **223**, 47 (1989).
6. F. Bertola, L. M. Buson, and W. W. Zeilinger, Astrophys. J. Lett. **401**, L79 (1992).
7. R. Buta and D. A. Crocker, Astron. J. **105**, 1344 (1993).
8. C. M. Carollo, M. Stiavelli, and J. Mack, Astron. J. **116**, 68 (1998).
9. R. A. Chevalier and I. Furenlid, Astrophys. J. **225**, 67 (1978).
10. F. Combes, in *Advanced Lectures on the Starburst-AGN Connection,* Ed. by I. Aretxaga, D. Kunth, and R. Mejica (World Scientific, Singapore, 2001), p. 223; astro-ph/0010570.
11. G. Contopouls and P. Grosbol, Astron. Astrophys. Rev. **1**, 261 (1989).
12. G. de Vaucouleurs, Astrophys. J., Suppl. Ser. **29**, 193 (1975).
13. M. F. Duval and G. Monnet, Astron. Astrophys., Suppl. Ser. **61**, 141 (1985).
14. D. M. Elmegreen, B. G. Elmegreen, and K. S. Eberwein, Astrophys. J. **564**, 234 (2002).
15. E. Emsellem, astro-ph/0202522 (2002).
16. E. Emsellem, D. Greusard, F. Combes, *et al.*, Astron. Astrophys. **368**, 52 (2001).
17. P. Englmaier and I. Shlosman, Astrophys. J. **528**, 677 (2000).
18. P. Erwin and L. S. Sparke, Astrophys. J. Lett. **521**, L37 (1999).
19. P. Erwin and L. S. Sparke, Astrophys. J. (2002) (in press); astro-ph/0203514.
20. P. Ferruit, A. S. Wilson, and J. Mulchaey, Astrophys. J., Suppl. Ser. **128**, 139 (2000).
21. Z. Frei, P. Guhathakirta, J. E. Gunn, and J. A. Tyson, Astron. J. **111**, 174 (1996).
22. A. M. Fridman and O. V. Khoruzhii, Phys. Lett. A **276**, 199 (2000).
23. A. M. Fridman, O. V. Khoruzhii, E. V. Polyachenko, *et al.*, Mon. Not. R. Astron. Soc. **323**, 651 (2001).
24. D. Friedli and L. Martinet, Astron. Astrophys. **277**, 27 (1993).
25. D. Friedli, H. Wozniak, and M. Rieke, Astron. Astrophys., Suppl. Ser. **118**, 461 (1996).
26. C. Heller, I. Chlosman, and P. Englmaier, Astrophys. J. **553**, 661 (2001).
27. J. Higdon, R. Buta, and G. B. Purcel, Astron. J. **115**, 80 (1998).
28. B. Jungwiert, F. Combes, and D. J. Axon, Astron. Astrophys., Suppl. Ser. **125**, 479 (1997).
29. A. V. Khoperskov, A. V. Zasov, and N. V. Tyurina, Astron. Zh. **78**, 213 (2001) [Astron. Rep. **45**, 180 (2001)].
30. A. V. Khoperskov, A. V. Moiseev, and E. A. Chulanova, Bull. Spec. Astrophys. Obs. **52**, 135 (2002b).
31. J. H. Knapen, I. Shlosman, C. H. Heller, *et al.*, Astrophys. J. **528**, 219 (2000a).
32. J. H. Knapen, I. Shlosman, and R. F. Peletier, Astrophys. J. **529**, 93 (2000b).
33. K. Kohno, R. Kawabe, and B. Vila-Vilaro, Astrophys. J. **511**, 157 (1999).
34. J. Kormendy, Astrophys. J. **257**, 75 (1982).
35. J. Kormendy, Astrophys. J. **275**, 529 (1983).
36. K. Kuijken, D. Fisher, and M. R. Merrifield, Mon. Not. R. Astron. Soc. **283**, 543 (1996).
37. S. Laine, J. H. Knapen, D. Pérez-Ramírez, *et al.*, Mon. Not. R. Astron. Soc. **324**, 891 (2001).
38. S. Laine, I. Shlosman, J. H. Knapen, and R. F. Peletier, Astrophys. J. **567**, 97 (2002).
39. P. O. Lindblad, Astron. Astrophys. Rev. **9**, 221 (1999).
40. V. V. Lyakhovich, A. M. Fridman, O. V. Khoruzhiĭ, and A. I. Pavlov, Astron. Zh. **74**, 509 (1997) [Astron. Rep. **41**, 447 (1997)].
41. W. Maciejewski and L. S. Sparke, Mon. Not. R. Astron. Soc. **313**, 745 (2000).
42. W. Maciejewski, J. Teuben, L. S. Sparke, and J. M. Stone, Mon. Not. R. Astron. Soc. **329**, 502 (2002).
43. R. H. Miller and B. F. Smith, Astrophys. J. **227**, 785 (1979).
44. A. V. Moiseev, Bull. Spec. Astrophys. Obs. **51**, 11 (2001a); astro-ph/0111219.
45. A. V. Moiseev, Bull. Spec. Astrophys. Obs. **51**, 140 (2001b); astro-ph/0111219.
46. A. V. Moiseev, Preprint No. 166, SAO RAN (Special Astrophysical Observatory, Russian Academy of Sciences, Nizhni Arkhyz, 2002).
47. A. V. Moiseev and V. V. Mustsevoĭ, Pis'ma Astron. Zh. **26**, 657 (2000) [Astron. Lett. **26**, 565 (2000)].
48. A. V. Moiseev, J. R. Valdes, and V. O. Chavushyan, Preprint No. 171, SAO RAN (Special Astrophysical Observatory, Russian Academy of Sciences, Nizhni Arkhyz, 2002).
49. G. Monnet, R. Bacon, and E. Emsellem, Astron. Astrophys. **253**, 366 (1992).
50. J. S. Mulchaey, M. W. Regan, and A. Kundu, Astrophys. J., Suppl. Ser. **110**, 299 (1997).
51. E. Pérez, I. Márquez, F. Durret, *et al.*, Astron. Astrophys. **353**, 893 (2000).
52. G. R. Petitpas and C. D. Wilson, Astrophys. J. (2002) (in press); astro-ph/0204413.
53. D. Pfenninger and C. A. Norman, Astrophys. J. **363**, 391 (1990).

54. M. Rozas, M. Relano, A. Zurita, and J. E. Beckman, Astron. Astrophys. **386**, 42 (2002).
55. K. Sakamoto, S. K. Okumura, S. Ishizuki, and N. Z. Scoville, Astrophys. J. **525**, 691 (1999).
56. E. Schinnerer, W. Maciejewski, N. Scoville, and L. A. Moustakas, Astrophys. J. (2002) (in press); astro-ph/0204133.
57. J. A. Selwood and A. Wilkinson, Rep. Prog. Phys. **56**, 173 (1993).
58. M. A. Shaw, F. Combes, D. J. Axon, and G. S. Wright, Astron. Astrophys. **173**, 31 (1993).
59. I. Shlosman and C. Heller, Astrophys. J. **565**, 921 (2002).
60. I. Shlosman, J. Frank, and M. C. Begeman, Nature **338**, 45 (1989).
61. O. K. Sil'chenko, A. N. Burenkov, and V. V. Vlasyuk, Astron. Astrophys. **326**, 941 (1997).
62. O. K. Sil'chenko, Pis'ma Astron. Zh. **28**, 243 (2002) [Astron. Lett. **28**, 207 (2002)].
63. A. J. Turnbull, A. J. Bridges, and D. Carter, Mon. Not. R. Astron. Soc. **307**, 967 (1999).
64. P. Vauterin and H. Dejonghe, Mon. Not. R. Astron. Soc. **286**, 812 (1997).
65. H. Woznik, D. Friedli, L. Martinet, *et al.*, Astron. Astrophys., Suppl. Ser. **111**, 115 (1995).
66. A. V. Zasov and A. V. Khoperskov, Astron. Zh. **79**, 195 (2002) [Astron. Rep. **46**, 173 (2002)].

Translated by V. Astakhov

Astronomy Letters, Vol. 28, No. 11, 2002, pp. 769–772. Translated from Pis'ma v Astronomicheskiĭ Zhurnal, Vol. 28, No. 11, 2002, pp. 855–858.
Original Russian Text Copyright © 2002 by Sibgatullin, Doroshenko.

Pulsar Magnetic Field for an Infinitely Conductive Accretion Disk

N. R. Sibgatullin* **and T. A. Doroshenko**

Moscow State University, Vorob'evy gory, Moscow, 119899 Russia

Received April 1, 2002

Abstract—The magnetic-field distribution outside a flat, infinitely conductive unbounded disk in the field of a point magnetic dipole is determined. A relationship is established between the problem of magnetic-field determination and the problem of the flow of an ideal incompressible fluid around an infinitely thin disk.

Key words: *magnetic dipole, disk accretion.*

INTRODUCTION

Here, we determine the magnetic-field distribution outside a flat, infinitely conductive disk in the field of a point magnetic dipole. This problem is of astrophysical interest (Lipunov 1987). Previously, it was solved in the two-dimensional case by Lipunov and Shakura (1980). Aly (1980) obtained a solution in the more complex three-dimensional case. Kundt and Robnik (1980) considered both these solutions and illustrated magnetic field lines in various cases for various parameters. We propose a new method of solution that can be generalized to compact magnetospheres and that yields the result previously obtained by Aly (1980) in the special case of flat, infinitely thin disks. We establish a relationship between the problem of magnetic-field determination and the problem of the flow of an ideal incompressible fluid around an infinitely thin disk.

THE HYDRODYNAMIC PROBLEM OF THE FLOW AROUND A CIRCULAR DISK

The problem of a magnetic dipole surrounded by a perfectly conducting accretion disk can be solved by using the classical problem of the flow of an ideal fluid around an infinitely thin circular disk.

Recall the solution of the problem of the flow around a disk (Lamb 1932). The disk is assumed to be infinitely thin. Hence, it has virtually no effect on the motion of an ideal fluid in the case of horizontal flow. Therefore, it will suffice to consider only the flow of fluid perpendicular to the plane of the circular disk:

$$\varphi_1 \approx Ur\cos\gamma, \quad r \to \infty. \tag{1}$$

Let a circular disk lie in the $z = 0$ plane and be defined by the equation $x^2 + y^2 = R^2$. We solve this problem by switching to the limit from the problem of the flow around an ellipsoid with the equation

$$\frac{x^2}{a^2} + \frac{y^2}{b^2} + \frac{z^2}{c^2} = 1. \tag{2}$$

Without loss of generality, we assume that $c > b > a$.

Let us introduce an ellipsoidal coordinate system in which the coordinates are the roots of the (Jacoby) equation

$$\frac{x^2}{a^2+\theta} + \frac{y^2}{b^2+\theta} + \frac{z^2}{c^2+\theta} = 1. \tag{3}$$

They are denoted by λ, μ, and ν, where $\lambda > \mu > \nu$.

The $\lambda = \text{const}$, $\mu = \text{const}$, and $\nu = \text{const}$ families are the families of confocal ellipsoids, one-sheet hyperboloids, and two-sheet hyperboloids, respectively.

From the definition (3) of the curvilinear system of λ, μ, ν coordinates, we can obtain

$$2\frac{\partial x}{\partial\lambda} = \frac{x}{a^2+\lambda}, \quad 2\frac{\partial y}{\partial\lambda} = \frac{y}{b^2+\lambda}, \quad 2\frac{\partial z}{\partial\lambda} = \frac{z}{c^2+\lambda}, \ \ldots. \tag{4}$$

The expressions for the metric components in the λ, μ, ν coordinate system follow from relations (4):

$$g_{\lambda\lambda} = \frac{(\lambda-\mu)(\lambda-\nu)}{4D(\lambda)}; \quad g_{\mu\mu} = \frac{(\lambda-\mu)(\mu-\nu)}{4D(\mu)}; \tag{5}$$

$$g_{\nu\nu} = \frac{(\mu-\nu)(\lambda-\nu)}{4D(\nu)}; \qquad g_{ij} = 0, \quad i \neq j,$$

where $D(\theta) \equiv (a^2+\theta)(b^2+\theta)(c^2+\theta)$.

---

[*] E-mail: `sibgat@mech.math.msu.su`

Let us write the Laplace equation $\Delta\varphi = 0$ in the curvilinear system of λ, μ, ν coordinates:

$$\Delta\varphi = \frac{1}{\sqrt{g}}\frac{\partial}{\partial y^i}\left(\sqrt{g}g^{ij}\frac{\partial\varphi}{\partial y^j}\right) = 0; \qquad (6)$$

$$y^1 = \lambda, \quad y^2 = \mu, \quad y^3 = \nu.$$

We seek the required solution to the Laplace equation in the form (Lamb 1932)

$$\varphi_1 = z\chi(\lambda). \qquad (7)$$

Thus,

$$\Delta(z\chi) = z\Delta\chi + 2\frac{\partial\chi}{\partial z} = z\Delta\chi(\lambda) + 2\frac{\partial\chi}{\partial\lambda}\frac{\partial\lambda}{\partial z} = 0. \qquad (6')$$

Using expressions (4) and (5), we can derive

$$\frac{\partial\lambda}{\partial z} = \frac{\partial z}{\partial\lambda}g^{\lambda\lambda} = \frac{z}{2(c^2+\lambda)}\frac{4D(\lambda)}{(\lambda-\mu)(\lambda-\nu)}. \qquad (8)$$

Equation (6′) can then be reduced to

$$\frac{1}{c^2+\lambda} + \frac{1}{\sqrt{D(\lambda)}\frac{d\chi}{d\lambda}}\frac{d}{d\lambda}\left(\sqrt{D(\lambda)}\frac{d\chi}{d\lambda}\right) = 0. \qquad (9)$$

Multiplying (9) by $d\lambda$ and integrating it over λ (in the sense of indefinite integrals) yields

$$\frac{d\chi}{d\lambda} = \frac{c_0}{(c^2+\lambda)\sqrt{D(\lambda)}}. \qquad (10)$$

Let us integrate Eq. (10) by setting $\chi|_\infty = 0$:

$$\chi = -c_0\int\limits_\lambda^\infty \frac{d\lambda}{(c^2+\lambda)\sqrt{D(\lambda)}}. \qquad (11)$$

It remains to determine the constant c_0.

The normal to the ellipsoid (2) has the components

$$\mathbf{n} = \frac{1}{\sqrt{g_{\lambda\lambda}}}\left(\frac{\partial x}{\partial\lambda}, \frac{\partial y}{\partial\lambda}, \frac{\partial z}{\partial\lambda}\right)\Bigg|_{\lambda=0}. \qquad (12)$$

For the fluid potential φ_0 in the frame of reference associated with the moving ellipsoid, we have the boundary condition $\partial\varphi_0/\partial n = 0$ at $\lambda = 0$. Let the flow velocity at infinity in this frame of reference be U. The fluid potential φ_1 in the frame of reference where the fluid at infinity is at rest is related to the potential φ_0 by $\varphi_1 = z\cos\gamma U + \varphi_0$. Therefore,

$$\frac{\partial\varphi_1}{\partial n} = U\cos\gamma\frac{\partial z}{\partial n} = \frac{U\cos\gamma}{\sqrt{g_{\lambda\lambda}}}\frac{\partial z}{\partial\lambda}. \qquad (13)$$

On the other hand, it follows from Eq. (7) that

$$\frac{\partial\varphi_1}{\partial n} = \frac{\partial}{\partial n}(z\chi) = \frac{1}{\sqrt{g_{\lambda\lambda}}}\frac{\partial}{\partial\lambda}(z\chi). \qquad (14)$$

Thus,

$$\frac{z\chi}{2c^2} + z\frac{d\chi}{d\lambda}\Bigg|_{\lambda=0} = \frac{U\cos\gamma z}{2c^2}. \qquad (15)$$

Hence, using Eqs. (10) and (11), we obtain

$$c_0 = \frac{U\cos\gamma}{\frac{2}{abc} - \int\limits_0^\infty \frac{d\lambda}{(c^2+\lambda)\sqrt{D(\lambda)}}}. \qquad (16)$$

For a circular disk, $a = b = R$, we must switch to the limit $c \to 0$ to obtain

$$c_0 = \frac{UR^3\cos\gamma}{\pi}. \qquad (17)$$

Thus, we finally obtain

$$\chi(\lambda) = -\frac{UR^3\cos\gamma}{\pi}\int\limits_\lambda^\infty \frac{d\lambda}{\lambda\sqrt{\lambda}(R^2+\lambda)} \qquad (18)$$

$$= U\left(1 - \frac{2R}{\pi\sqrt{\lambda}} - \frac{2}{\pi}\arctan\frac{\sqrt{\lambda}}{R}\right).$$

Let us make the substitution (Thomson)

$$r' = \frac{R^2}{r}. \qquad (19)$$

A circular disk of radius R then transforms into a plane with a circumference of radius R cut out at the coordinate origin.

Let us verify that if φ_1 is a solution to the Laplace equation, then the function φ_1' defined by the equality

$$\varphi_1' = \frac{\varphi_1}{r'}, \qquad (20)$$

is also a solution to the Laplace equation.

Let us write the Laplace equation in spherical coordinates r, α, β:

$$\Delta\varphi = \frac{1}{r^2}\frac{\partial}{\partial r}\left(r^2\frac{\partial\varphi}{\partial r}\right) \qquad (21)$$

$$+ \frac{1}{r^2}\left(\frac{1}{\sin\alpha}\frac{\partial}{\partial\alpha}\left(\sin\alpha\frac{\partial\varphi}{\partial\alpha}\right) + \frac{1}{\sin^2\alpha}\frac{\partial^2\varphi}{\partial\beta^2}\right) = 0.$$

Denote $\tilde{\Delta} \equiv \frac{1}{\sin\alpha}\frac{\partial}{\partial\alpha}\left(\sin\alpha\frac{\partial\varphi}{\partial\alpha}\right) + \frac{1}{\sin^2\alpha}\frac{\partial^2\varphi}{\partial\beta^2}$.

After the substitutions (19) and (20), the Laplace equation takes the form

$$\frac{\partial^2\varphi}{\partial r'^2} + \frac{1}{r'^2}\tilde{\Delta}\varphi = 0. \qquad (22)$$

Hence, substituting $\varphi = r'\varphi'$ yields

$$r'\frac{\partial^2\varphi'}{\partial r'^2} + 2\frac{\partial\varphi'}{\partial r'} + \frac{1}{r'^2}r'\tilde{\Delta}\varphi' = 0. \qquad (23)$$

Thus, φ' is also a solution to the Laplace equation:

$$\frac{1}{r'^2}\frac{\partial}{\partial r'}\left(r'^2\frac{\partial}{\partial r'}\varphi'\right)+\frac{1}{r'^2}\tilde{\Delta}\varphi'=0. \qquad (22')$$

Using Eqs. (7), (18), and (20), we therefore obtain

$$\varphi_1'=\frac{UR^2\cos\gamma\cos\alpha}{r'^2}\left(1-\frac{2R}{\sqrt{\lambda}\pi}-\frac{2}{\pi}\arctan\frac{\sqrt{\lambda}}{R}\right). \qquad (24)$$

Consider the λ-dependent family of spheroids in a Cartesian coordinate system:

$$\frac{x^2+y^2}{R^2+\lambda}+\frac{z^2}{\lambda}=1. \qquad (25)$$

Solving Eq. (25) for λ in spherical coordinates

$$x=r\cos\beta\sin\alpha, \quad y=r\sin\beta\sin\alpha, \quad z=r\cos\alpha,$$

yields

$$\lambda_{1,2}=\frac{R^4}{2r'^2}\left(1-\frac{r'^2}{R^2}\pm\sqrt{\left(1-\frac{r'^2}{R^2}\right)^2+4\frac{r'^2}{R^2}\cos^2\alpha}\right). \qquad (26)$$

Let us introduce the dimensionless variable $\tilde{r}=\frac{r'}{R}$. For the asymptotic approach to the disk, $|\cos\alpha|\ll 1$; therefore, for $r'>R$ (if the "+" sign is taken in front of the radical),

$$\lambda\approx\frac{R^2\cos^2\alpha}{\tilde{r}^2-1}. \qquad (26')$$

Substituting expression (26′) derived for λ into Eq. (24) then yields near the disk

$$\varphi_1'\approx\frac{U\cos\gamma\cos\alpha}{\tilde{r}^2}\times\left[1-\frac{2}{\pi}\frac{\sqrt{\tilde{r}^2-1}}{|\cos\alpha|}-\frac{2}{\pi}\arctan\left(\frac{|\cos\alpha|}{\sqrt{\tilde{r}^2-1}}\right)\right].$$

When an ideal fluid flows around an infinitely thin disk parallel to its plane along the X axis, the potential is

$$\varphi_2=U\sin\gamma x=U\sin\gamma\sin\alpha\cos\beta r. \qquad (27)$$

After the substitutions of (19) and (20), we then obtain

$$\varphi_2'=\frac{UR^2\sin\gamma\sin\alpha\cos\beta}{r'},$$

$$\varphi_2'=\frac{UR^2\sin\gamma\sin\alpha\cos\beta}{r'^2}=\frac{U\sin\gamma\sin\alpha\cos\beta}{\tilde{r}^2}.$$

The potential of the flow around a circular disk inclined to the disk plane is given by $\varphi_1+\varphi_2$.

THE MAGNETIC-FIELD POTENTIAL

Applying the inversion transformation (19) and (20) to the potential $\varphi_1+\varphi_2$ yields

$$\varphi'=\frac{U\cos\gamma\cos\alpha}{\tilde{r}^2}\left[1-\frac{2}{\pi}\frac{\sqrt{\tilde{r}^2-1}}{|\cos\alpha|}-\frac{2}{\pi}\arctan\left(\frac{|\cos\alpha|}{\sqrt{\tilde{r}^2-1}}\right)\right]+\frac{U\sin\gamma\sin\alpha\cos\beta}{\tilde{r}^2}. \qquad (28)$$

Equation (28) gives the sought-for expression for the potential of the magnetic field produced by a dipole at the center of a circular hole in an infinitely conductive accretion disk.

THE PULSAR MAGNETIC-FIELD PRESSURE

It can be easily verified that

$$\varphi_{1+}'=-\varphi_{1-}',$$
$$\varphi_{2+}'=\varphi_{2-}'.$$

The following total magnetic-field pressure acts on the accretion-disk surface from above and from below (Aly 1980):

$$P=\frac{1}{2\pi}\left[\frac{\partial}{\partial\tilde{r}}(\varphi_{1+}')\frac{\partial}{\partial\tilde{r}}(\varphi_{2+}')+\frac{1}{\tilde{r}^2}\frac{\partial}{\partial\alpha}(\varphi_{1+}')\frac{\partial}{\partial\alpha}(\varphi_{2+}')\right]\Bigg|_{\alpha\to\frac{\pi}{2}}. \qquad (29)$$

After some transformations, we derive the following expression for the normal component of the force density:

$$P=2\frac{U^2\cos\beta\sin2\gamma}{\pi}\frac{8-4\tilde{r}^2}{\tilde{r}^6\sqrt{\tilde{r}^2-1}}. \qquad (29')$$

The magnetic-field pressure tends to infinity near the inner edge of the disk. If the pulsar spin axis is perpendicular to the disk plane, then the magnetic-field direction precesses with the pulsar angular velocity. When substituted in the equations of motion for the accreted matter with an allowance made for accretion-disk elasticity, the forces calculated here will generate transverse waves in the disk.

Let us assume that the magnetic dipole rotates about an axis perpendicular to the plane of the unperturbed disk with angular velocity ω . The disk is deformed in the field of forces (29). If a Keplerian orbit is taken out of the unperturbed plane, then decomposing the gravitational force per unit mass (from the central body) into the normal and tangential components yields

$$F_{gr}=-\frac{GM}{r^3}w,$$

where w is the vertical displacement of the deformed disk and M is the mass of the central body. Therefore, the Newton equation for the normal component of the equations of motion can be written as

$$\sigma\frac{\partial^2 w}{\partial t^2} = -\sigma\frac{GM}{r^3}w + P, \qquad (30)$$

where σ is the disk surface density. We use expression (29) for P, where $\varphi - \omega t$ should be substituted for φ because of dipole rotation.

We seek a solution to Eq. (30) for w in the form

$$w = W(r)\cos(\varphi - \omega t).$$

We then derive from Eq. (30)

$$w = \frac{P(r)}{\sigma(\Omega^2_{\text{kep}} - \omega^2)}; \quad \Omega^2_{\text{kep}} \equiv \frac{GM}{r^3}. \qquad (31)$$

Therefore, the closer is the disk edge $r = R$, the larger is the disk deformation. This, probably, leads to the growth of instabilities near the disk edge.

Equation (30) disregards viscous forces and nonlinear deviations from the unperturbed plane. Therefore, the solution for w at $\Omega_{\text{kep}} = \omega$ is actually bounded. According to Eq. (31), the vertical deviations and velocities are largest when $\Omega_{\text{kep}} = \omega$ at the disk edge. In this case, a vertical jet that precesses with the angular velocity of the magnetic dipole can be formed.

CONCLUSIONS

We have shown that the problem of magnetic-field determination outside an infinitely conductive plane with a circular hole which has a point magnetic dipole located at its center is equivalent to the problem of the flow of an ideal incompressible fluid around an infinitely thin disk. This analogy also applies to the case where infinitely conductive portions alternate with nonconductive portions.

REFERENCES

1. J. J. Aly, Astron. Astrophys. **86**, 192 (1980).
2. W. Kundt and M. Robnik, Astron. Astrophys. **91**, 305 (1980).
3. H. Lamb, *Hydrodynamics* (Cambridge Univ. Press, Cambridge, 1932; Gostekhizdat, Moscow, 1947).
4. V. M. Lipunov, *Astrophysics of Neutron Stars* (Nauka, Moscow, 1987).
5. V. M. Lipunov and N. I. Shakura, Pis'ma Astron. Zh. **6**, 28 (1980) [Sov. Astron. Lett. **6**, 14 (1980)].

Translated by A. Dambis

Astronomy Letters, Vol. 28, No. 11, 2002, pp. 773–777. Translated from Pis'ma v Astronomicheskiĭ Zhurnal, Vol. 28, No. 11, 2002, pp. 859–863.
Original Russian Text Copyright © 2002 by Balega, Tokovinin, Pluzhnik, Weigelt.

The Spectroscopic and Interferometric Orbit of Gliese 150.2

Yu. Yu. Balega[1]*, A. A. Tokovinin[2,3], E. A. Pluzhnik[1], and G. Weigelt[4]

[1] *Special Astrophysical Observatory, Russian Academy of Sciences,*
Nizhni Arkhyz, Karachai-Cherkessian Republic, 357147 Russia
[2] *Cerro Tololo Inter-American Observatory, Casilla 603, La Serena, Chile*
[3] *Sternberg Astronomical Institute, Moscow University, Universitetskiĭ pr. 13, Moscow, 119992 Russia*
[4] *Max-Planck-Institut für Radioastronomie, Auf dem Hügel 69, Bonn, 53121 Germany*

Received June 14, 2002

Abstract—We determined the spectroscopic–interferometric orbit of the binary red dwarf Gliese 150.2 with a period of 13.84 yr and a semimajor axis of 0.257 arcsec. Based on the orbital elements and on accurate measurements of the magnitude difference at several wavelengths, we estimated the spectral types and masses of the components (K0 V and M0 V, 0.79 and 0.55 $M_{\odot}$) and the dynamical parallax of the binary (40.4 mas). *© 2002 MAIK "Nauka/Interperiodica".*

Key words: *stars—properties, classification; binary stars, orbits.*

INTRODUCTION

Determining the accurate masses and luminosities of low-mass main-sequence stars is still of current interest. The mass–luminosity relation has a significant scatter in the range of low masses, which may be related to such parameters as the age, chemical composition, and chromospheric activity. For observations to be compared with current theories, the masses must be measured with an accuracy of the order of 1%. This accuracy can be achieved when determining the masses from the combined spectroscopic–interferometric orbits derived from high-quality observations (see, e.g., Forveille *et al.* 1999).

The nearby red dwarf Gliese 150.2 (2000: $3^{\rm h}44^{\rm m}49^{\rm s} + 46°02'09''$) is also designated as HD 23140 and HIP 17941. Its parallax, measured by Hipparcos (ESA 1997) is 37.6 mas; i.e., its distance from the Sun slightly exceeds the 25-pc limit adopted in the Catalogue of Nearby Stars (Gliese and Jahreiss 1991). Below, we show that Gl 150.2 is actually 24.5 pc away and it may be rightly considered to be a close neighbor of the Sun. According to the SIMBAD database, the spectral type of Gl 150.2 is K2 V, $V = 7\overset{\rm m}{.}71$, and $B{-}V = 0\overset{\rm m}{.}86$.

Since 1986, the object has been observed with a correlation radial-velocity meter (RVM) (Tokovinin 1987) as part of the survey of low-mass dwarfs in the solar neighborhood. From the results of the first five years of observations (Tokovinin 1992a), the star was not classified as a spectroscopic binary, because the first measurement was deemed to be, probably, erroneous. Subsequent measurements clearly showed the star to be a spectroscopic binary. Its radial velocities were measured using different telescopes with apertures from 0.6 to 1.25 m located in Crimea, Moscow, Abastumani, and at Mt. Maidanak. Spectroscopic binarity was also independently discovered by astronomers at the Geneva Observatory (Mayor 1991).

In 1993, Balega *et al.* (1997) performed the first speckle-interferometric measurement of Gl 150.2 with the 6-m (BTA) telescope. Seven interferometric observations have been obtained to date. Apart from the radial velocities covering the complete orbital period, these data allow the combined spectroscopic–interferometric orbit to be computed. This is the goal of this study.

THE ORBIT

The input data needed to compute the orbit are given in Tables 1 and 2. Table 1 contains heliocentric Julian dates JD, radial velocities, their formal errors determined by fitting the correlation profile with a Gaussian, and residuals to the orbit ($O{-}C$). The formal errors do not include the additional instrumental error of the RVM, which is about 0.3 km s^{-1} (Tokovinin 1992a).

Our interferometric observations were obtained with the 6-m Special Astrophysical Observatory (BTA) telescope using the instrumentation and techniques described by Balega *et al.* (2002). In 1996,

---

*E-mail: `balega@sao.ru`

Table 1. Radial velocities and residuals to the orbit

JD 2 400 000+	V, km s^{-1}	σ_V, km s^{-1}	$O-C$, km s^{-1}
46726.595	22.59	0.23	−0.70
47560.193	27.08	0.31	0.22
47755.579	27.48	0.14	−0.01
47791.493	28.26	0.20	0.68
47882.392	28.21	0.22	0.45
48166.511	29.36	0.24	1.70 :
48841.550	21.78	0.20	0.36
49017.172	19.85	0.13	0.37
49223.561	17.83	0.14	−0.03
49238.578	17.90	0.11	0.12
49389.276	16.80	0.19	−0.31
49649.441	15.90	0.16	−0.77 :
49705.278	16.84	0.29	0.18
49975.547	17.02	0.15	0.09
50324.575	18.45	0.14	0.69 :
50482.205	18.38	0.38	0.15
50758.391	19.60	0.25	0.44
50803.351	19.45	0.19	0.13
51057.561	20.06	0.21	−0.21
51428.581	21.35	0.08	−0.41
51445.556	21.99	0.10	0.16
51876.441	23.39	0.18	−0.28
51929.231	23.69	0.23	−0.21
51929.225	23.43	0.23	−0.47
52163.569	24.34	0.11	−0.60
52184.530	25.03	0.16	0.00
52197.566	25.26	0.18	0.17

Gl 150.2 was measured in the infrared with the speckle camera of the Institut für Radioastronomie in Bonn (Balega *et al.* 2001). Table 2 contains epochs of observations, position angles with their errors, separations between the components with their errors, and residuals to the orbit in angle and distance. The next columns give the mean wavelengths and FWHMs of the spectral bands, measured magnitude differences with their errors, and, finally, bibliographic references. The 2000–2001 measurements are published for the first time.

We computed preliminary orbital elements in 1999 and gradually improved them as new observations became available. The final values the nine elements for the combined orbit (Table 3) were obtained by least-squares fitting with weights inversely proportional to the squares of the observational errors (Tokovinin 1992b). We give the position angle of the ascending node, Ω (equinox 2000), and the periastron longitude, ω, for the primary component A rather than for the secondary, as is commonly done for visual orbits. The resulting weighted mean residuals correspond to the errors in of the input data: 0.34 km s^{-1}, 0°.32, and 1 mas in radial velocity, position angle, and separation, respectively. Three of the 27 radial-velocity measurements (marked by a colon in Table 1 and by circles in Fig. 1) were rejected, because their residuals are appreciably larger than their formal errors. Figure 1 presents the radial-velocity curve; Fig. 2 shows the visual orbit and interferometric data.

PARAMETERS OF THE COMPONENTS

The elements of the combined spectroscopic–interferometric orbit allow the component masses and the parallax to be determined without any additional assumptions. However, this requires knowledge of the radial-velocity half-amplitudes for both components. No secondary lines were observed in Gl 150.2, because they are weak and cannot be separated from primary lines (the FWHM of the RVM instrumental profile is 14 km s^{-1}).

Given the orbital elements and the trigonometric parallax (37.6 mas), the sum of the component masses can be easily calculated: 1.7 $M_\odot$. This value is in poor agreement with the spectral type K2 V. Judging by the orbit (Fig. 2), there was nonlinear orbital motion during the Hipparcos measurements (1989–1992) that was disregarded in the data reduction and could affect the measured parallax. Similar cases were pointed out by Shatskiĭ and Tokovinin (1998). The Hipparcos measured proper motion in right ascension, 287 mas per year, significantly differs from the AGK3 parallax, 322 ± 8 mas per year, because in 1991 the system's photocenter was displaced westward due to its orbital motion. Thus, the Hipparcos data for Gl 150.2 are not accurate enough for an absolute determination of the sum of masses. A new astrometric solution that explicitly takes into account the orbital elements (Söderhjelm 1999) will bridge this gap. For the time being, however, we rely on the standard relations for dwarf stars and choose the component parameters that are in best agreement with all of the data.

As the first approximation, we take the component masses to be 0.7 $M_\odot$ and 0.5 $M_\odot$ and calculate the dynamical parallax, 42 mas. This gives an estimate

Table 2. Speckle data

Epoch	θ, deg	ρ, mas	$\Delta\theta$, deg	$\Delta\rho$, mas	$\lambda/\Delta\lambda$, nm	Δm	References
1993.8418	$106\overset{\circ}{.}9 \pm 1.0$	186 ± 4	$-1\overset{\circ}{.}0$	−4	667/20	2.2	1
1994.7130	102.2 1.0	249 1	0.1	0	656/30	2.49	1
1996.7500	92.2 1.0	244 1	−0.1	1	1238/276	1.67 ± 0.12	2
1998.7746	71.6 1.5	125 4	0.2	1	545/30	2.69 0.11	3
1999.8212	25.7 1.4	67 2	−0.3	1	545/30	2.64 0.08	3
2000.8649	320.2 1.1	96 2	0.3	0	610/20	2.55 0.08	4
2001.7582	299.9 0.8	157 2	−0.3	2	545/30	2.70 0.06	4
	300.0 0.6	156 2	–	–	600/30	2.67 0.04	–
	300.2 0.4	155 1	–	–	750/35	2.08 0.04	–
	300.4 0.4	155 1	–	–	850/75	1.86 0.04	–

References: 1, Balega *et al.* (1997); 2, Balega *et al.* (2001); 3, Balega *et al.* (2002); 4, this paper.

of the absolute magnitude for the primary component that better corresponds to a K0 V dwarf with a mass of 0.79 $M_\odot$. Given the spectroscopic orbital parameters and inclination, the corresponding mass of the secondary component is found to be 0.55 $M_\odot$. Thus, the spectral type of the secondary is close to M0 V. With the improved sum of the masses, the dynamical parallax is found to be 40.4 ± 0.7 mas (the error is almost exclusively determined by the accuracy of measuring the semimajor axis).

The model of the binary Gl 150.2 is based on the normal luminosities and colors of a pair of K0 V and M0 V dwarfs, according to the tables from Lang (1992) and Straizys (1977). The photometric parameters of this model are compared with observations in Table 4. There is reasonable agreement between the measured and model magnitude differences, which independently confirms the model.

Table 3. Orbital elements

Element	Value	Error
P, yr	13.877	0.016
T	1992.092	0.016
e	0.2764	0.0034
a''	0.2574	0.0046
Ω, deg (A)	281.1	1.0
ω, deg (A)	74.85	0.25
i, deg	101.37	0.12
K_1, km s^{-1}	5.60	0.12
V_0, km s^{-1}	21.86	0.07
σ_θ, deg	0.32	–
σ''_ρ	0.001	–
σ_V, km s^{-1}	0.34	–

Let us estimate the effect of the secondary component on the measured radial velocities. The RVM correlation profile is a blend of the component profiles displaced in opposite directions. The maximum radial-velocity difference (i.e., the sum of the half-amplitudes) can be reliably estimated from the formula

$$K_1 + K_2 = 29.8 \sin i (1 - e^2)^{-1/2} (M/P)^{1/3}$$
$$= 14.0 \text{ km s}^{-1},$$

where M is the sum of the component masses in $M_\odot$ and P is the period in years. Therefore, the profiles are

Table 4. A model of the binary Gl 150.2 (the parallax is 40.4 mas)

Parameter	Component		A+B Model (observations)	B−A Model (observations)
	A	B		
Spectral type	K0 V	M0 V	– (K2 V)	–
Mass, $M_\odot$	0.79	0.55	1.33	–
V	7.87	10.77	7.80 (7.71)	2.90 (2.65)
$B{-}V$	0.82	1.44	0.85 (0.86)	–
R	7.23	9.62	7.12	2.39 (2.29)
J	6.49	8.06	6.26	1.57 (1.67)

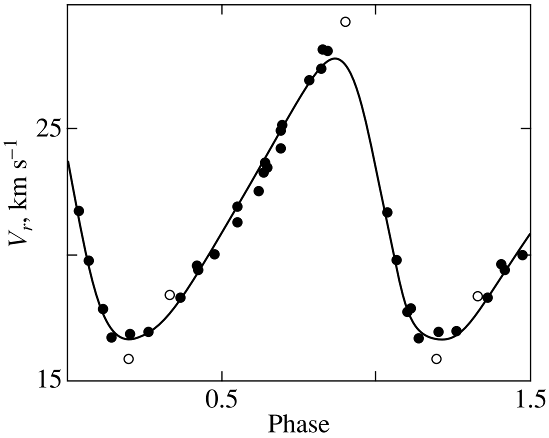

Fig. 1. The radial-velocity curve for Gl 150.2. The open circles represent the observations rejected when improving the orbit.

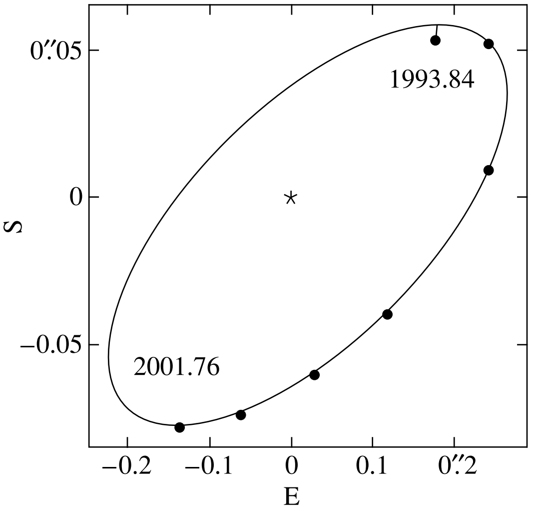

Fig. 2. The orbit of Gl 150.2 (solid line) and the speckle-interferometric observations (circles). The epochs of the first and last measurements are marked. The primary component is marked by an asterisk.

actually unresolvable with the RVM. In this case, the effect of the secondary reduces to a decrease in the radial-velocity amplitude by a factor of $(1-\alpha)/(1+\alpha)$, where $\alpha = E_2/E_1$ is the ratio of the equivalent widths for the component correlation profiles.

Using the relation between the equivalent width of the RVM correlation profile and the $B-V$ color (Tokovinin 1990) as well as the model parameters of the components, we estimated the initial (as for single stars) equivalent widths of the components: $E_{01} = 3.36$ km s^{-1} and $E_{02} = 2.70$ km s^{-1}. Given the magnitude difference $\Delta V = 2.65$, the equivalent widths in the combined spectrum are $E_1 = 3.09$ km s^{-1} and $E_2 = 0.21$ km s^{-1}. Their sum is in satisfactory agreement with the measured equivalent width of 3.21 ± 0.03 km s^{-1}. Thus, the model corresponds to $\alpha = 0.07$, and the true radial-velocity half-amplitude of the primary component must have been $K_1 = 6.43$ km s^{-1}. In this case, however, the amplitude of the secondary, $K_2 = 14 - 6.43 = 7.57$ km s^{-1}, leads to an implausibly high mass ratio, $q = K_1/K_2 = 0.85$, while our model corresponds to $q = 0.70$.

Our analysis shows that the measured radial-velocity half-amplitude is, probably, unaffected by secondary lines. This can be the case, for example, when the secondary has rapid axial rotation (>20 km s^{-1}) and its weak lines have absolutely no effect on the combined correlation profile. The width of the primary profile corresponds to axial rotation with $v \sin i = 3.6 \pm 0.3$ km s^{-1}.

CONCLUSIONS

We computed a combined spectroscopic–interferometric orbit for a nearby pair of red dwarfs G1. Although the binary itself was discovered recently and its orbit was determined for the first time, the accuracy of the orbital elements is comparatively high. This was achieved through the high accuracy of speckle interferometry and by combining it with radial velocities.

The available observations are still too few in number to accurately measure the component masses. The most direct method of mass determination consists in high-precision radial-velocity measurements for both components. This requires a spectral resolution of at least 50 000 and a high signal-to-noise ratio. This would allow the lines of the secondary component to be identified unless the rapid rotation of the latter hinders this identification. It is best to carry out observations in the infrared, where the magnitude difference between the components is smaller than that in the optical range. The new orbit will help in planning such observations. The second, less reliable method of mass determination is to reprocess the Hipparcos data and to improve the parallax using the new orbit.

ACKNOWLEDGMENTS

This study was supported by the Russian Foundation for Basic Research (project no. 01-02-16563). We are grateful to N. Gorynya for the radial-velocity observations in 1999–2001.

REFERENCES

1. I. I. Balega, Yu. Yu. Balega, H. Falcke, *et al.*, Pis'ma Astron. Zh. **23**, 199 (1997) [Astron. Lett. **23**, 172 (1997)].
2. I. I. Balega, Yu. Yu. Balega, K.-H. Hofmann, and G. Weigelt, Pis'ma Astron. Zh. **27**, 117 (2001) [Astron. Lett. **27**, 95 (2001)].
3. I. I. Balega, Y. Y. Balega, K.-H. Hofmann, *et al.*, Astron. Astrophys. **385**, 87 (2002).
4. ESA, *The Hipparcos and Tycho Catalogues* (European Space Agency, 1997), ESA SP 1200.
5. T. Forveille, J.-L. Beuzit, X. Delfosse, *et al.*, Astron. Astrophys. **351**, 619 (1999).
6. W. Gliese and H. Jahreiss, *Catalogue of Nearby Stars* (Astronomisches Rechen-Institut, Heidelberg, 1991).
7. K. R. Lang, *Astrophysical Data: Planets and Stars* (Springer-Verlag, New York, 1992).
8. M. Mayor, private communication (1991).
9. N. I. Shatskiĭ and A. A. Tokovinin, Pis'ma Astron. Zh. **24**, 780 (1998) [Astron. Lett. **24**, 673 (1998)].
10. S. Söderhjelm, Astron. Astrophys. **341**, 121 (1999).
11. V. Straizys, *Multicolor Stellar Photometry* (Mokslas, Vil'nyus, 1977; Pachart Publ. House, Tucson, 1992).
12. A. A. Tokovinin, Astron. Zh. **64**, 196 (1987) [Sov. Astron. **31**, 98 (1987)].
13. A. A. Tokovinin, Pis'ma Astron. Zh. **16**, 52 (1990) [Sov. Astron. Lett. **16**, 24 (1990)].
14. A. A. Tokovinin, Astron. Astrophys. **256**, 121 (1992a).
15. A. A. Tokovinin, Astron. Soc. Pac. Conf. Ser. **32**, 573 (1992b).

Translated by N. Samus'

Astronomy Letters, Vol. 28, No. 11, 2002, pp. 778–782. Translated from Pis'ma v Astronomicheskiĭ Zhurnal, Vol. 28, No. 11, 2002, pp. 864–8869.
Original Russian Text Copyright © 2002 by Arkhipova, Ikonnikova, Komissarova, Esipov.

Haro's Star (PG 1444+236): A Hot Subdwarf of the Galactic Halo?

V. P. Arkhipova[*], **N. P. Ikonnikova**, **G. V. Komissarova**, and **V. F. Esipov**

Sternberg Astronomical Institute, Universitetskiĭ pr. 13, Moscow, 119992 Russia

Received June 10, 2002

Abstract—We present our photometric and spectroscopic observations of the hot emission-line high-latitude ($b = +64°$) star discovered by Haro. The star exhibited no light variability during 1993–2001. Based on our observations and on the detailed study of the star by Herbig (1992), we improved its parameters, $T = 22\,000$ K and $\log g = 4.2$, and inferred its evolutionary status. We show that Haro's star does not belong to the class of protoplanetary objects but is most likely a hot subdwarf of the Galactic halo with an emission-line spectrum formed in the outer layers of the star or in its stellar wind. *© 2002 MAIK "Nauka/Interperiodica".*

Key words: *stars, subdwarfs, evolution.*

INTRODUCTION

The emission-line star with the coordinates $\alpha = 14^{\rm h}47^{\rm m}08\overset{\rm s}{.}2$ and $\delta = +23°21'38''$ (2000) that was discovered by Haro during an Hα sky survey belongs to a group of poorly studied hot stars. Its magnitude is $V = 13\overset{m}{.}1$ and it is located at the latitude $b = +64°$. Herbig (1992) carried out the only detailed study of this star. UBV photometry and spectroscopy led him to conclude that the star most likely belongs to the group of objects in the transition stage from the asymptotic giant branch (AGB) to the central stars of planetary nebulae. However, the star was not detected as an IR source in the IRAS sky survey. Herbig (1992) also discussed another possible interpretation of the status of Haro's star: its belonging to the group of horizontal-branch subdwarfs, i.e., to the stars of the Galactic halo.

Apart from the Hα survey, the star was detected during a survey of faint blue stars at high Galactic latitudes (Green *et al.* 1986) and was designated PG 1444+236; the authors of the PG catalog classified it as "sd."

Wesemael *et al.* (1992) performed photometry of the star in Strömgren's system and gave the following estimates: $y = 13\overset{m}{.}136$, $b{-}y = -0.043$, $u{-}b = -0.207$, and $m_1 = +0.056$.

In 1993, we included Haro's star in our program of photometric and spectroscopic monitoring of candidates for protoplanetary objects. The objective of our study is to search for nonstationary and evolutionary effects in the program objects. Our program covers mostly supergiant stars with large IR excesses (IRAS sources) but also includes a few emission-line stars at high Galactic latitudes. Haro's star is from precisely this group.

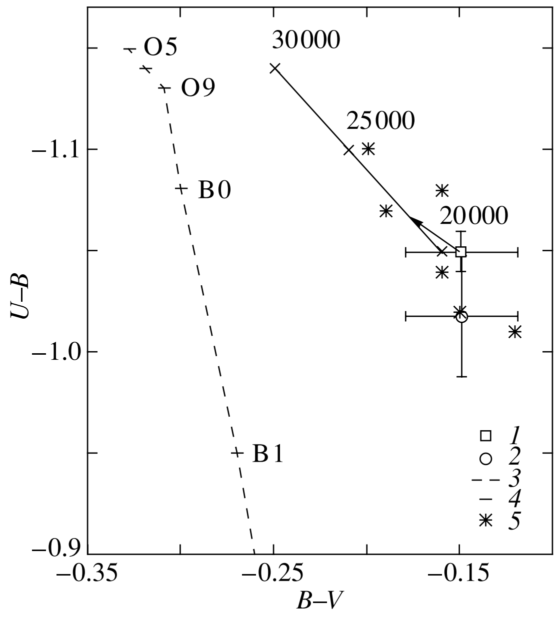

Fig. 1. The two-color $U{-}B$, $B{-}V$ diagram: the mean color indices of Haro's star determined by Smak (Herbig 1992) (*1*) and by us (*2*) with their dispersions; the arrow moves Smak's data along the reddening line by $E(B{-}V) = 0.03$; (*3*) the main sequence; (*4*) the sequence of blackbody radiation with T = 20 000, 25 000, and 30 000 K; (*5*) objects from the PG catalog (Green *et al.* 1986).

---

[*] E-mail: `vera@sai.msu.ru`

1063-7737/02/2811-0778$22.00 © 2002 MAIK "Nauka/Interperiodica"

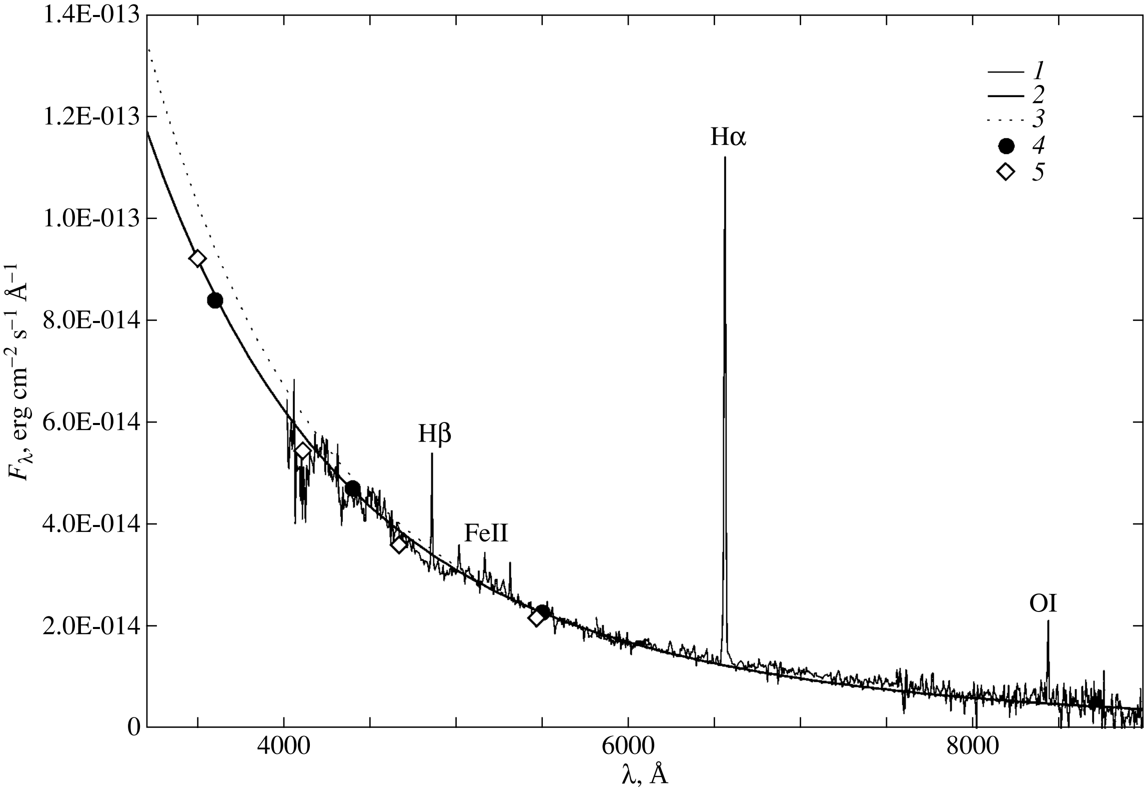

Fig. 2. The absolute spectral energy distribution of Haro's star obtained on May 17, 2001 (*1*). Blackbody radiation spectra: $T = 22\,000$ K (*2*) and $T = 28\,000$ K (*3*); the UBV (*4*) and $uvby$ (*5*) fluxes reduced to the absolute scale. The observations were corrected for interstellar extinction with $E(B{-}V) = 0.03$.

UBV PHOTOMETRY

We carried out our photoelectric observations of Haro's star with the aim of searching for its possible variability from 1993 until 2001 at the Crimean Station of the Sternberg Astronomical Institute (SAI) using a 60-cm reflector equipped with a UBV photometer. The comparison star was HD 130384; we determined its magnitudes ($V = 8\overset{m}{.}56$, $B = 8\overset{m}{.}79$, $U = 8\overset{m}{.}97$) by tying it into the photometric standard BD+26°2606 from the catalog by Blanco *et al.* (1968). A total of 30 magnitude estimates were obtained for Haro's star, with the mean magnitudes being $\langle V\rangle = 13\overset{m}{.}12 \pm 0\overset{m}{.}04$, $\langle B\rangle = 12\overset{m}{.}97 \pm 0\overset{m}{.}04$, and $\langle U\rangle = 11\overset{m}{.}96 \pm 0\overset{m}{.}05$. The error in the UBV magnitudes is estimated to be $\pm 0\overset{m}{.}03$. Taking into account this error, we may assume the scatter of magnitudes within each season and between observing seasons to be random and the star's brightness to be constant. The photometric observations of the star during six nights in April–June 1962 performed by Smak (Herbig 1992) revealed no light variations on a short time scale; his UBV magnitudes ($V = 13\overset{m}{.}11 \pm 0\overset{m}{.}03$, $B{-}V = -0.15 \pm 0.03$, and $U{-}B = -1.05 \pm 0.01$) match our mean magnitudes, with the limits of the observational errors. Therefore, the star's mean brightness has not changed in ~40 years.

The interstellar extinction toward Haro's star is low. According to Herbig (1992), it does not exceed 0.03 in the color excess $E(B{-}V)$.

The position of Haro's star in the two-color $U{-}B$, $B{-}V$ diagram is shown in Fig. 1. Also shown in the same figure are several sdB PG subdwarfs with UBV photometry from the PG survey (Green *et al.* 1986). They have color excesses similar to that of Haro's star. Figure 1 also shows the main sequence (dashed line) and the sequence of color indices (solid line) for a blackbody with temperatures of 20 000, 25 000, and 30 000 K. Note that the color indices of Haro's star disagree with those of main-sequence stars but are closest to the colors of a blackbody with a temperature between 20 000 and 22 000 K. In the two-color diagram, the sdB subdwarfs also lie closer to the blackbody line than to the main sequence.

SPECTROSCOPIC OBSERVATIONS

During 2000–2001, we obtained four low-resolution spectrograms for Haro's star in the range λ4000–9000 Å. Our observations were carried out

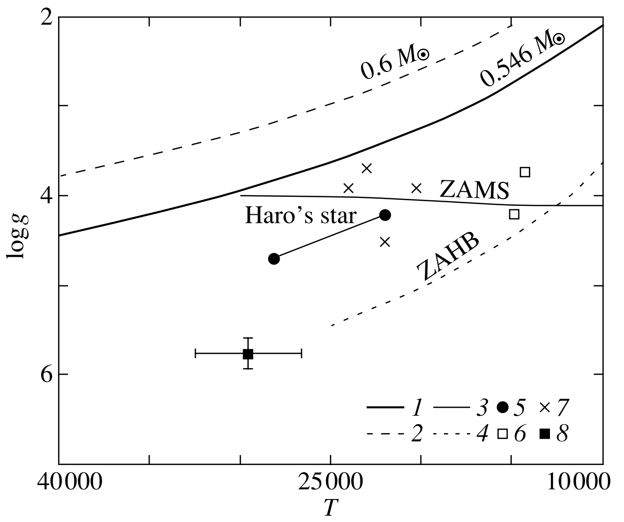

Fig. 3. A (T, $\log g$) diagram: the tracks of post-AGB stars with $M = 0.546\ M_\odot$ (*1*) and $M = 0.6\ M_\odot$ (*2*); (*3*) the zero-age main sequence (ZAMS); (*4*) the zero-age horizontal branch (ZAHB); (*5*) Haro's star with our parameters and with the parameters from Herbig (1992); (*6*) emission-line stars from the PG catalog (Green *et al.* 1986); (*7*) blue subdwarfs — low-mass evolved stars from the sample by Hambly *et al.* (1997); (*8*) the mean parameters and their dispersions for 28 classical sdB subdwarfs from the sample by Saffer *et al.* (1994).

with the 125-cm reflector at the Crimean Station of the SAI using a fast spectrograph. The detector was an SBIG ST-6I 274 × 375-pixel CCD array, which gives a resolution of $\sim$5.5 Å mm^{-1} with a 600 lines mm^{-1} grating. The comparison star was 50 Boo (B9 V); its absolute spectral energy distribution was taken from Voloshina *et al.* (1982). The spectral classification of the star cannot be made using the absorption lines because of the low spectral resolution. The Hα line is strongest in the λ4000–9000 Å emission-line spectrum. The Hβ and Hγ emission lines are observed against the background of broad absorption features of the star, which prevents a reliable measurement of the Balmer decrement. The emission-line spectrum also exhibits numerous Fe II lines that belong to the 21, 22, 37, 38, 39, 40, 42, 49, 73, and 74 multiplets, as well as strong O I λ7772 and λ8446 Å lines. Equivalent widths of the strongest lines are given in Table 1.

Figure 2 shows the spectral energy distribution of the star corrected for interstellar extinction with $E(B{-}V) = 0.03$. Also shown in the figure are the UBV fluxes reduced to an absolute scale; data from Straizys (1977) were used for their calibration.

As was mentioned above, the magnitude of Haro's star was measured in the four Strömgren bands (Wesemael *et al.* 1992). Using the absolute calibration of the Strömgren system (Heber *et al.* 1984), we transformed the narrow-band magnitudes into absolute fluxes and corrected them for interstellar extinction. They are also shown in Fig. 2. We see that the agreement with our UBV data and with spectrophotometry is good. Figure 2 shows the energy distribution for a blackbody with a temperature of 22 000 K; it is in agreement with the photometric and spectroscopic data in the range λ3500–9000 Å.

Thus, we take the temperature of Haro's star to be $\sim$22 000 K. This is in contrast to Herbig (1992), who assigned it a temperature of 28 200 K, in accordance with its spectral type (B0–B1).

THE EVOLUTIONARY STATUS OF HARO'S STAR

Can Haro's star belong to protoplanetary objects with a minimum mass at the post-AGB evolutionary stage, which evolve very slowly along the horizontal track and which approach the ionization stage of a planetary nebula? Its low-excitation emission-line spectrum allows us to consider this possibility. However, it should be borne in mind that there is no IR excess characteristic of the protoplanetary stage in Haro's star. Nevertheless, we could assume that, through the very slow evolution typical of postAGB stars with masses $\sim$0.55 $M_\odot$, its dust envelope could have dispersed by the time the star became hot and began to ionize the remnants of its gaseous envelope. According to the calculations by Bloecker (1995) and Schoenberner and Weidemann (1983) and from comparison of the theory with observations, the minimum observed mass of the planetary-nebula nucleus is currently estimated to be 0.55 $M_\odot$. The relationship between the luminosity and mass of a protoplanetary object in the horizontal part of its evolutionary track that we derived by fitting the numerical data from Bloecker (1995) within the mass range 0.94 to 0.546 $M_\odot$ is $L/L_\odot = 42838\ln(1.9M/M_\odot)$. On the other hand, $L = 4\pi R^2\sigma T^4$, $g = GM/R^2$, and, eliminating R from the equations yields the following relation between g, T, and M:

$$g/g_\odot = M/M_\odot(T_\odot/T)^4/42838\ln(1.9M/M_\odot). \quad (1)$$

Herbig (1992) estimated the star's spectral type from spectroscopic data to be B0–B1 and assigned it the effective temperature $T = 28\,200$ K. Based on this value, he obtained $\log g = 4.7$ from the full width of the Hβ absorption line. With these parameters, the star's mass is outside the theoretical mass range for the nuclei of planetary nebulae.

However, in our view, the parameters from Herbig (1992) should be revised. According to our results, the temperature of Haro's star is definitely lower, being about 22 000 K. Using the technique

Table 1. The equivalent widths of emission lines in the spectrum of Haro's star

λ, Å	Species	$\langle W\lambda\rangle$, Å	σ, Å	N
6562.8	H I	95.1	2.3	4
5018.4	Fe II	1.5	0.4	3
5169.0	Fe II	1.8	0.2	4
5197.6	Fe II	1.3	0.4	4
5234.6	Fe II	1.3	0.7	4
5276.0	Fe II	2.5	0.4	4
5316.6	Fe II	2.6	0.7	4
7711.7	Fe II	3.8	0.1	4
7772.0 7774.2 7775.4	O I	7.6	0.8	2
8446.4	O I	22.4	3.5	2

from Herbig (1992), we then obtain $\log g = 4.2$.[1] Such gravity is also inconsistent with the assumption that Haro's star belongs to protoplanetary objects, because the maximum possible value of $\log g$ for a protoplanetary object with a mass of $0.55 M_\odot$ and a temperature of 22 000 K calculated using Eq. (1) is 3.59.

The parameters of Haro's star are compared with the atmospheric parameters of hot subdwarfs and some other stars at high Galactic latitudes in Fig. 3, which shows a $(T, \log g)$ diagram. The postAGB evolutionary tracks of stars with masses of $0.546\ M_\odot$ and $0.6\ M_\odot$, as inferred by Bloecker (1995), the zero-age main sequence (Allen 1973), and the zero-age horizontal branch from Saffer *et al.* (1997) are plotted in this diagram. The figure shows Herbig's parameters of Haro's star ($T = 28\,200$ K, $\log g = 4.7$) and our parameters ($T = 22\,000$ K, $\log g = 4.2$). For comparison with Haro's star, the diagram also displays two emission-line objects from the PG catalog and blue subdwarfs, low-mass evolved stars from the sample by Hambly *et al.* (1997) with atmospheric parameters similar to those of Haro's star. Table 2 gives data for these objects. The diagram also shows the mean parameters and their dispersions for 28 classical sdB subdwarfs from the sample by Saffer *et al.* (1994).

Table 2. Parameters of Haro's star (PG 1444+236) and several stars from the PG catalog

PG	T, K	$\log g$	sp	b, deg	PG class
0914+001	14 297	3.72	Be	+32	sdB
1002+506	14 900	4.2	B5Ve	+51	CV
1213+456	22 000	4.5	–	+70	HBB
1243+275	24 000	3.9	–	+89	HBB
0833+699	20 200	3.9	–	+34.5	sdOA
0832+676	23 000	3.7	–	+35	sdOA
1444+236	22 000	4.2	B0–B1e	+64	sd

As we see from Fig. 3, Haro's star lies in the $(T, \log g)$ diagram much lower than the track for postAGB objects with a minimum mass of $0.546\ M_\odot$. Therefore, it does not belong to postAGB stars.

One might think that the object is a main-sequence Be star. Haro's star is one of the three B stars from the PG catalog (Green *et al.* 1986) with emission lines in their spectra. According to Ringwald *et al.* (1997), the object PG 1002+506 is definitely a young, massive ($M = 4.2\ M_\odot$), rapidly rotating ($v \sin i = 340 \pm 50$ km s^{-1}) star at the distance $z = +10.8$ kpc from the Galactic plane. Another star, PG 0914+001 (Saffer *et al.* 1997), with its parameters T and $\log g$ can also be on the main sequence. As for Haro's star, it is much hotter than the above two stars and if its spectral type, as estimated by Herbig (1992), is B0–B1, then it must be a massive ($M > 10\ M_\odot$) star at $z = 19.7$ kpc. According to our temperature estimates, its spectral type is most likely B2, and then $z = 7.2$ kpc, but this is unlikely for a B2 Ve star of mass $M \sim 7 M_\odot$. Its UBV data are also atypical of a main-sequence B star. Thus, we, like Herbig (1992), rule out the possibility that Haro's star belongs to the class of ordinary Be stars, although, for greater confidence, high-resolution spectroscopic observations are needed to study the line profiles.

With its parameters T and $\log g$, Haro's star can be a representative of the hot horizontal-branch stars or can belong to the Galactic thick-disk population. However, as was pointed out by Herbig (1992), typical horizontal-branch stars show no emission features in their spectra. Therefore, the low-excitation emission-line spectrum of Haro's star is unusual for this type of star. It would be reasonable to assume that the emission-line spectrum could belong to the remnant of the star's gaseous envelope ejected during a preceding evolutionary stage. However, the absence of the low-excitation forbidden lines (N II, O II, S II) characteristic of a low-density gas most likely makes this explanation implausible. The intensity ratio of

---

[1] The determination of $\log g$ is based on comparison of the observed and theoretical full-widths of the Hβ line profile as a function of the temperature and $\log g$ in the model of a purely hydrogen atmosphere by Wesemael *et al.* (1980). According to Herbig (1992), the observed full width of the Hβ line at 0.9 of the continuum level is 19 Å.

the Hα and Hβ emission lines is significantly distorted by their superposition on the star's hydrogen absorption-line spectrum, which prevents the Balmer decrement from being used as a criterion for the nebular origin of the emission-line spectrum. The absence of the forbidden Fe II lines can also point to a nonradiative excitation of the permitted Fe II lines. In addition, the measured width of the emission features in the hydrogen lines [about 15 Å, as obtained by Herbig (1992)] is too large for these lines to originate in the remnant of the nebular envelope.

The emission-line spectrum of Haro's star is most likely related to the star itself and originates in its outer layers with a high gas density dissimilar to the typical density of nebular shells. It is also possible that the star possesses a noticeable stellar wind and the emission-line spectrum is formed in it. The expansion of the emission-line formation region is suggested by the two-component structure of the Fe II lines found by Herbig (1992).

CONCLUSIONS

We have carried out a photometric and spectroscopic analysis of Haro's poorly studied emission-line star located at a high Galactic latitude. We detected no light variability of the star with an amplitude larger than $0\overset{m}{.}05$ over the observing period from 1993 until 2001. The star's brightness was, probably, constant in the last several decades. We determined the atmospheric parameters of the star: $T = 22\,000$ K and $\log g = 4.2$.

The question as to the nature of Haro's star is yet to be clarified. In our view, the star is most likely an evolved object whose mass is near the lower mass limit for post-AGB stars. The star may possess a noticeable stellar wind.

By the suggestion of the referee, we compared the parameters of Haro's star with the evolutionary tracks of helium stars from Dorman *et al.* (1993). The comparison indicates that Haro's star could be an evolved helium star at the relatively short stage of transition from the horizontal branch to white dwarfs. In any case, the parameters of Haro's star are not typical of young subdwarfs.

ACKNOWLEDGMENTS

We are very grateful to the Russian Foundation for Basic Research for financial support (project no. 01-02-16530).

REFERENCES

1. C. W. Allen, *Astrophysical Quantities* (Athlone Press, London, 1973; Mir, Moscow, 1977).
2. V. M. Blanco, S. Demers, G. G. Douglass, and M. P. Fitzgerald, *Photoelectric Catalogue, Magnitudes and Colors of Stars in the UBV and UCBV System* (USNO, Washington, DC, 1968), Publ. US Naval Obs., Second Series, 21.
3. T. Bloecker, Astron. Astrophys. **299**, 755 (1995).
4. B. Dorman, R. T. Rood, and R. W. O'Connell, Astrophys. J. **419**, 596 (1993).
5. R. F. Green, M. Schmidt, and J. Liebert, Astrophys. J., Suppl. Ser. **61**, 305 (1986).
6. N. C. Hambly, W. R. J. Rolleston, and F. P. Keenan, Astrophys. J., Suppl. Ser. **111**, 419 (1997).
7. U. Heber, K. Hunger, G. Jonas, and R. P. Kudritzki, Astron. Astrophys. **130**, 119 (1984).
8. G. H. Herbig, Rev. Mex. Astron. Astrofis. **24**, 187 (1992).
9. F. A. Ringwald, W. R. J. Rolleston, R. A. Saffer, and J. R. Thorstensen, Astrophys. J. **497**, 717 (1998).

11\. R. A. Saffer, P. Bergerot, D. Koester, and J. Liebert, Astrophys. J. **432**, 351 (1994).

11\. R. A. Saffer, F. P. Keenan, and N. C. Hambly, Astrophys. J. **491**, 172 (1997).

12\. D. Schoenberner and V. Weidemann, in *Proceedings of the IAU Symposium No. 103,* Ed. by D. R. Flower (D. Reidel, Dordrecht, 1983), p. 359.

13\. V. Straizys, *Multicolor Stellar Photometry* (Mokslas, Vil'nyus, 1977; Pachart Publ. House, Tucson, 1992).

14\. I. B. Voloshina, I. N. Glushneva, and V. T. Doroshenko, *Spectrophotometry of Bright Stars* (Nauka, Moscow, 1982).

15\. F. Wesemael, L. M. van Horn, M. P. Savedoff, and L. H. Auer, Astrophys. J., Suppl. Ser. **43**, 159 (1980).

16\. F. Wesemael, G. Fontaine, P. Bergeron, and R. Lamontagne, Astron. J. **104**, 203 (1992).

Translated by N. Samus'

Astronomy Letters, Vol. 28, No. 11, 2002, pp. 783–791. Translated from Pis'ma v Astronomicheskiĭ Zhurnal, Vol. 28, No. 11, 2002, pp. 870–879.
Original Russian Text Copyright © 2002 by Kopylova, Stepanov, Tsap.

Radial Oscillations of Coronal Loops and Microwave Radiation from Solar Flares

Yu. G. Kopylova[1*], **A. V. Stepanov**[1], and **Yu. T. Tsap**[2]

[1]*Pulkovo Astronomical Observatory, Russian Academy of Sciences,*
Pulkovskoe sh. 65, St. Petersburg, 196140 Russia
[2]*Crimean Astrophysical Observatory, p/o Nauchnyi, Crimea, 334413 Ukraine*

Received April 11, 2002

Abstract—We consider the damping mechanisms for the radial oscillations of solar coronal loops in the approximation of a thin magnetic flux tube. We show that the free tube oscillations can have a high Q if the plasma density inside the magnetic flux tube is much higher than the density outside. We analyze the effect of radial coronal-loop magnetic-field oscillations on the modulation of the microwave radiation from solar flares. In the case of a nonthermal gyrosynchrotron mechanism, the fluxes from optically thin and optically thick sources are modulated in antiphase. Based on our model, we diagnose the flare plasma. For the event of May 23, 1990, we estimate the spectral index for accelerated electrons, $\alpha \approx 4.4$, and the magnetic-field strength in the region of energy release, $B \approx 190$ G. *© 2002 MAIK "Nauka/Interperiodica".*

Key words: *Sun, coronal loops, radial oscillations, damping, gyrosynchrotron radiation.*

INTRODUCTION

It follows from solar-flare observations that the radiation is often modulated quasi-periodically with a characteristic period $T_{\mathrm{p}} \sim 1$–10 s (Aschwanden 1987; Aschwanden *et al.* 1999). The modulation can be observed at various flare phases and, in general, its depth does not exceed 10–30%. In some cases, the flux time profiles in the hard X-ray range (Kane *et al.* 1983; Kaufmann *et al.* 2000) or in the $H\alpha$ line (Wulser and Kampfer 1987) correlate with microwave radiation, suggesting a common nature of the phenomenon under consideration.

The observed second radiation pulsations are attributed to the following mechanisms: (1) magnetohydrodynamic (MHD) coronal-loop oscillations (Rosenberg 1970; Meerson *et al.* 1978; Zaĭtsev and Stepanov 1982a, 1989; Edwin and Roberts 1983; Roberts *et al.* 1984; Qin *et al.* 1996); (2) quasi-periodic magnetic reconnection (Zarro *et al.* 1987; Kliem *et al.* 2000); (3) electric-current modulation in flare loops (Stepanov and Tsap 1993; Zaitsev *et al.* 1998); and (4) periodicity in nonlinear wave–wave or wave–particle interactions [see Aschwanden (1987) for a review]. The available observational data are too scarce to favor a particular mechanism. Nevertheless, ample evidence has recently emerged for the possible generation of radial fast magnetosonic (FMS) oscillations (the sausage mode) of coronal loops in active regions; these oscillations are capable of effectively modulating the magnetic field, density, and temperature of the plasma (Aschwanden *et al.* 1999). Among recent results, we note the coronal-loop oscillations in white light and in the Fe XIV (5303 Å) line with the characteristic period of ~6 s and the modulation depth of ~1% detected by Williams *et al.* (2001).

Although a large number of studies deal with radial oscillations (Aschwanden 1987; Zaĭtsev and Stepanov 1982a, 1989; Edwin and Roberts 1983; Roberts *et al.* 1984; Zaĭtsev *et al.* 1994), many questions have yet to be solved. In particular, the FMS modes in the solar corona are strongly damped (Zaĭtsev *et al.* 1994) because of electron heat conduction (Zaĭtsev and Stepanov 1982a) and ion viscosity (Tsap 2000) as well as the radiation of MHD waves into the surrounding medium (Zaĭtsev and Stepanov 1975; Spruit 1982). The maintenance of the oscillations by perturbations from the photosphere appears somewhat questionable. Thus, for example, even torsional modes that are not accompanied by a change in plasma gas pressure with periods shorter than several tens of seconds are almost completely absorbed by the chromosphere while propagating from the photosphere into the corona (De Pontieu *et al.* 2001), whereas the generation of oscillations at Cherenkov (Zaĭtsev and Stepanov 1982b) or bounce resonance (Meerson *et al.* 1978) requires special conditions. Meanwhile, the number of radi-

---

[*] E-mail: `yulia@saoran.spb.su`

ation oscillations occasionally reach several hundred (Zodi *et al.* 1984). Consequently, the radial coronal-loop oscillations must have a high Q ($\geq 10^2$), at least in some cases. This raises the following question: What mechanisms determine the oscillation duration?

The damping of the radial oscillations of thin magnetic flux tubes due to the radiation of MHD waves into the surrounding medium (acoustic mechanism) was first considered by Zaĭtsev and Stepanov (1975). The damping decrement for the radial oscillations of coronal loops was determined from the dispersion relation for the eigenmodes of the magnetic flux tube. However, the solutions obtained cannot be considered to be reliable enough, because the dispersion relation contains ambiguous Bessel functions of a complex variable. In our view, the energy method appears more attractive (Tsap and Kopylova 2001). First, it allows the above difficulty to be circumvented and, second, it makes it possible to generalize the previous results. As for the ion viscosity, electron heat conduction, and radiative losses, these important dissipation mechanisms for the radial modes have not yet been studied in detail.

Important information on the physical conditions in the region of flare energy release can be obtained by analyzing coronal-loop oscillations (Zaĭtsev and Stepanov 1982a, 1989; Qin *et al.* 1996; Nakariakov and Ofman 2001). This promising field of research called coronal seismology is being intensively developed in connection with the problem of solar coronal heating. It is also of interest to determine the magnetic fields in active regions of the lower solar corona, because direct Zeeman measurements are difficult to make due to the high plasma temperature and because the results of indirect methods strongly depend on the adopted model restrictions. As a result, the field estimates vary over a wide range, from several tens to a thousand gauss (Nakariakov and Ofman 2001). Thus, new methods for diagnosing the solar coronal magnetic fields must be invoked.

In the first section, we analyze the damping mechanisms for radial coronal-loop oscillations in the approximation of a thin magnetic flux tube. The emphasis is on the acoustic mechanism. In the second section, we consider the effect of radial magnetic-field oscillations on the modulation of the nonthermal gyrosynchrotron radiation from trapped electrons in terms of the magnetic-bottle model. A new method for diagnosing the parameters of the energetic particles and magnetic field in the flare region is proposed. In the conclusion, we present and discuss our main results.

THE DAMPING OF RADIAL OSCILLATIONS

The Acoustic Mechanism

The acoustic mechanism can play a significant role in the damping of the MHD oscillations of magnetic flux tubes. The essence of this mechanism is that an oscillating tube is capable of losing its energy through wave radiation into the surrounding medium. Below, we use the technique outlined by Tsap and Kopylova (2001) to calculate the damping of radial oscillations.

Let us consider an oscillating, axisymmetric magnetic flux tube with a magnetic field $\mathbf{B}_0 = (0, 0, B_z(r))$, a plasma density $\rho_0(r)$, and a gas pressure $p_0(r)$. In the case of sausage-mode generation, the perturbations of equilibrium quantities can be represented as $\delta\xi(r)\exp(-i\omega t + ikz)$. After linearizing the system of ideal MHD equations, we derive two equations that describe the perturbation amplitudes of the total pressure $\delta P = \delta p + \delta B_z B_z/4\pi$ and radial velocity δv_r (Edwin and Roberts 1983; Ryutova 1988; Roberts 1991; Tsap and Kopylova 2001):

$$\frac{i\rho_0(\omega^2 - k^2 v_\mathrm{A}^2)}{r}\frac{\partial}{\partial r}\left(\frac{\partial(r\delta v_r)}{\partial r}\right) = \omega\mu^2\delta P, \qquad (1)$$

$$\omega\frac{\partial\delta P}{\partial r} = i\rho_0(\omega^2 - k^2 v_\mathrm{A}^2)\delta v_r, \qquad (2)$$

where

$$\mu^2 = \frac{(k^2 c_\mathrm{s}^2 - \omega^2)(\omega^2 - k^2 v_\mathrm{A}^2)}{(v_\mathrm{A}^2 + c_\mathrm{s}^2)(k^2 c_T^2 - \omega^2)}, \quad c_T^2 = \frac{v_\mathrm{A}^2 c_\mathrm{s}^2}{v_\mathrm{A}^2 + c_\mathrm{s}^2}, \qquad (3)$$

$v_\mathrm{A} = B_z/\sqrt{4\pi\rho_0}$ is the Alfvèn velocity, $c_\mathrm{s} = \sqrt{\gamma p_0/\rho_0}$ is the speed of sound, and $\gamma = 5/3$ is the adiabatic index.

In the approximation of a thin magnetic flux tube (Priest 1982), Eqs. (1) and (2) reduce to the Bessel equation

$$\frac{1}{r}\left(r\frac{\partial\delta P}{\partial r}\right) + \mu^2\delta P = 0. \qquad (4)$$

Its solutions for the internal (i) and external (e) parts of the tube are (Tsap and Kopylova 2001)

$$\delta P_\mathrm{i} = A_1 J_0(\mu_\mathrm{i} r), \quad \delta P_\mathrm{e} = A_2 H_0^{(1)}(\mu_\mathrm{e} r), \qquad (5)$$

where A_1 and A_2 are arbitrary constants; $J_0(\mu_\mathrm{i} r)$ and $H_0^{(1)}(\mu_\mathrm{e} r)$ are the Bessel and Hankel functions, respectively.

Assuming that $\mathrm{Re}\mu \gg \mathrm{Im}\mu$ and $\omega = \omega_0 - i\nu_\mathrm{a}$ ($\nu_\mathrm{a} \ll \omega_0$), we can easily derive an expression for the acoustic damping decrement for the oscillations of a magnetic flux tube with fixed ends of length L and radius a from the conservation of energy (Tsap and Kopylova 2001)

$$\nu_\mathrm{a} = \frac{F_r}{2W}. \tag{6}$$

Here, the radial wave energy flux into the surrounding medium, F_r, and the total oscillation energy, W, are expressed as

$$F_r = 4\pi r L |\delta P_\mathrm{e} \delta v_{r_\mathrm{e}}|, \tag{7}$$

$$W = 2\pi L \int_0^a \rho_\mathrm{i} |\delta v_{r_\mathrm{i}}|^2 \left(1 + \frac{v_{\mathrm{A_i}}^2}{v_\mathrm{p}^2}\right) r dr,$$

where the modulus sign denotes the product of complex conjugate quantities and $v_\mathrm{p} = \omega/k$.

Taking into account the asymptotic behavior of the Hankel functions (Watson 1945)

$$H_n^{(1)}(\eta r) \approx \sqrt{\frac{2}{\pi \eta r}} e^{i(\eta r - n\pi/2 - \pi/4)}, \quad \eta = \mathrm{const}, \tag{8}$$

and the well-known identity

$$\int J_n^2(\eta r) r dr = \frac{r^2}{2} \left(J_n^2(\eta r) - J_{n-1}(\eta r) J_{n+1}(\eta r)\right), \tag{9}$$

and denoting $\mathrm{Re}\,\mu = \mu_0$, we find from (7)–(9) that

$$F_r \approx 8L \frac{|A_2|^2 \omega_0}{\rho_\mathrm{e}(\omega_0^2 - k^2 v_{\mathrm{A_e}}^2)}, \tag{10}$$

$$W \approx \pi L \frac{|A_1|^2 \omega_0^2 (\mu_{0_\mathrm{i}} a)^2}{\rho_\mathrm{i}(\omega_0^2 - k^2 v_{\mathrm{A_i}}^2)^2} \left(1 + \frac{v_{\mathrm{A_i}}^2}{v_\mathrm{p}^2}\right) \times \left(J_1^2(\mu_{0_\mathrm{i}} a) - J_0(\mu_{0_\mathrm{i}} a) J_2(\mu_{0_\mathrm{i}} a)\right). \tag{11}$$

Substituting (10) and (11) in (6) then yields

$$\nu_\mathrm{a} \approx \frac{4}{\pi} \frac{|A_2|^2}{|A_1|^2} \frac{\rho_\mathrm{i}}{\rho_\mathrm{e}} \frac{1}{\omega_0} \frac{1}{(\mu_{0_\mathrm{i}} a)^2} \frac{(\omega_0^2 - k^2 v_{\mathrm{A_i}}^2)^2}{\omega_0^2 - k^2 v_{\mathrm{A_e}}^2} \times \frac{v_\mathrm{p}^2}{v_{\mathrm{A_i}}^2 + v_\mathrm{p}^2} \frac{1}{J_1^2(\mu_{0_\mathrm{i}} a) - J_0(\mu_{0_\mathrm{i}} a) J_2(\mu_{0_\mathrm{i}} a)}. \tag{12}$$

The continuity condition for the total-pressure and radial-velocity perturbations at the tube boundary $r = a$ suggests that

$$\delta P_\mathrm{i}(a) = \delta P_\mathrm{e}(a), \quad \delta v_{r_\mathrm{i}}(a) = \delta v_{r_\mathrm{e}}(a). \tag{13}$$

According to (1), (2), (5), and (13), we then have

$$\frac{|A_2|^2}{|A_1|^2} = \frac{|J_0(\mu_\mathrm{i} a)|^2}{|H_0^{(1)}(\mu_\mathrm{e} a)|^2} = \left(\frac{\rho_\mathrm{e}}{\rho_\mathrm{i}}\right)^2 \frac{|\mu_\mathrm{i}|^2}{|\mu_\mathrm{e}|^2} \frac{|\omega^2 - k^2 v_{\mathrm{A_e}}^2|^2}{|\omega^2 - k^2 v_{\mathrm{A_i}}^2|^2} \frac{|J_1(\mu_\mathrm{i} a)|^2}{|H_1^{(1)}(\mu_\mathrm{e} a)|^2}. \tag{14}$$

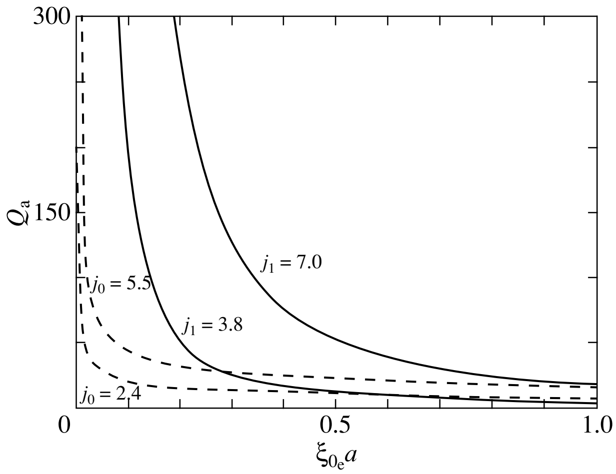

Plots of $Q_\mathrm{a} = \omega_0/\nu_\mathrm{a}$ versus $\xi_{0_\mathrm{e}} a = \omega_0 a / v_{\mathrm{A_e}}$ described by Eqs. (15) and (16). The plots correspond to the cases where the oscillation node of the perturbations in total pressure (dashed line: $j_0 = \xi_{0_\mathrm{i}} a$, where $j_0 = 2.4$ and 5.5 are zeros of the function J_0) or in radial velocity (solid line: $j_1 = \xi_{0_\mathrm{i}} a = j_1$, where $j_1 = 3.8$ and 7.0 are zeros of the function J_1) coincides with the magnetic flux tube boundary.

Combining Eqs. (12) and (14), we may conclude that the minimum values of the acoustic damping decrement ν_a correspond to the minimum values of $|J_0(\mu_\mathrm{i} a)|^2$ or $|J_1(\mu_\mathrm{i} a)|^2$. In the solar corona, the plasma $\beta = 8\pi p/B^2 \approx c_\mathrm{s}^2/v_\mathrm{A}^2 \ll 1$ and Eq. (3) for the radial modes whose frequency squared satisfies the inequality $\omega_0^2 \gg k^2 v_\mathrm{A}^2$ simplifies appreciably: $\mu \approx \omega/v_\mathrm{A} = \xi$. At the same time, if $\nu_\mathrm{a} a / v_\mathrm{A} \ll 1$, then we can expand the Bessel functions into a series, retaining only the term of the first order of smallness, i.e.,

$$J_0(\xi_\mathrm{i} a) \approx J_0(\xi_{0_\mathrm{i}} a) + \frac{i \nu_\mathrm{a} a}{v_\mathrm{A}} J_1(\xi_{0_\mathrm{i}} a),$$

$$J_1(\xi_\mathrm{i} a) \approx J_1(\xi_{0_\mathrm{i}} a) + \frac{i \nu_\mathrm{a} a}{v_\mathrm{A}} \left(J_0(\xi_{0_\mathrm{i}} a) - \frac{J_1(\xi_{0_\mathrm{i}} a)}{\xi_{0_\mathrm{i}} a}\right),$$

where $\mathrm{Re}\,\xi = \xi_0$. The above expressions and numerical estimates show that the functions $|J_0(\xi_\mathrm{i} a)|^2$ and $|J_1(\xi_\mathrm{i} a)|^2$ take on minimum values at zeros of the functions $J_0(\xi_{0_\mathrm{i}} a)$ and $J_1(\xi_{0_\mathrm{i}} a)$, respectively.

For the above cases, we find from Eq. (12) using (14) that

$$\frac{\nu_\mathrm{a}}{\omega_0} \approx \frac{4}{\pi} \frac{1}{(\xi_{0_\mathrm{i}} a)^2} \frac{1}{|H_1^{(1)}(\xi_{0_\mathrm{e}} a)|^2}, \quad J_0(\xi_{0_\mathrm{i}} a) = 0; \tag{15}$$

$$\frac{\nu_\mathrm{a}}{\omega_0} \approx \left(\frac{\pi}{4} \frac{\rho_\mathrm{e}}{\rho_\mathrm{i}} \frac{|H_0^{(1)}(\xi_{0_\mathrm{e}} a)|^2}{(\xi_{0_\mathrm{i}} a)^2}\right)^{1/3}, \quad J_1(\xi_{0_\mathrm{i}} a) = 0. \tag{16}$$

In the figure, $Q_a = \omega_0/\nu_a$ is plotted against argument $\xi_{0_e}a$ of the Hankel functions for various values of the parameter $j_n = \omega_0 a/v_{A_i}$, where j_n are zeros of the Bessel functions J_n, $n = 0, 1$. As we see, Q_a can reach several hundred if $\xi_{0_e}a \ll 1$ ($T_p \gg 2\pi a/v_{A_e}$); i.e., the plasma density inside the magnetic flux tube is much higher than the density outside ($\xi_{0_i}/\xi_{0_e} \approx \sqrt{\rho_i/\rho_e} > 10$). According to the latter inequality, at $T_p = 1$–10 s and $a \sim 10^8$ cm^{-3}, the Alfvèn velocity $v_{A_e} \gg 2\pi a/T_p = 10^7$–$10^8$ cm s^{-1}, which corresponds to the estimates of v_A in the lower solar corona (Aschwanden *et al.* 1999; Nakariakov and Ofman 2001). The increase in Q_a with j_n also engages our attention.

Our results suggest that high Q ($Q_a > 10^2$) radial coronal-loop oscillations can exist. Physically, this is explained by the fact that for the modes with $\omega_0 = j_n v_{A_i}/a$, the oscillation nodes of the perturbations in total pressure, δP_i, or in radial velocity, δv_{r_i}, coincide with the magnetic flux tube boundary, causing the generation of low-amplitude FMS waves in the external medium. Therefore, the minimum values of the acoustic damping decrement correspond to the frequencies for which $J_0(\xi_{0_i}a) = 0$ or $J_1(\xi_{0_i}a) = 0$. In addition, for $\xi_{0_e}a \ll 1$, the perturbations near the outer boundary of the magnetic flux tube are oscillatory in nature and only at large distances ($r \gg a$) do they transform into cylindrical waves capable of effectively transferring energy into the surrounding medium.

For $\xi_{0_e}a \ll 1$, the Hankel function takes the form $H_1^{(1)}(\xi_{0_e}a) \approx -2\xi_{0_e}/\pi$ and formula (15) reduces to the relation

$$\nu_a/\omega_0 \approx \pi\rho_e/\rho_i.$$

To within a coefficient, this relation matches the expression for the acoustic damping decrement derived from the dispersion relation (Zaĭtsev and Stepanov 1975).

The following important point should be emphasized. When examining the sausage modes, Roberts *et al.* (1984) assumed that $\mu_e^2 < 0$, thereby considering the arguments of the cylinder functions to be imaginary. In this case, the solution to the Bessel equation (4) for the external region can be expressed in terms of the Macdonald function $K_0(\mu_e a)$. In contrast to the Hankel function $H_0^{(1)}(\mu_e a)$, the behavior of this function is monotonic and, hence, magnetic flux tube oscillations will not lead to wave radiation into the surrounding medium. At the same time, if $\beta \ll 1$, then the quantity μ_e is imaginary only on condition that $ka > j_0(v_{A_e}^2 - v_{A_i}^2)/v_{A_e}^2$ (Roberts *et al.* 1984). Hence, assuming that $k = N\pi/L$, where N is a natural number, we obtain

$$N > \frac{j_0 L}{\pi a}\frac{v_{A_e}^2 - v_{A_i}^2}{v_{A_e}^2}. \qquad (17)$$

For coronal arches, $L \gg a$ and $v_{A_e} > v_{A_i}$, and in view of (17), we find that the number of nodes is $N_t = N - 1 \sim L/a \gg 1$. Therefore, the running FMS waves forming a standing wave whose wavelength $\lambda = 2L/N$ becomes comparable to the scale height of the lower solar atmosphere will be able to easily penetrate into the photosphere (Tsap and Kopylova 2001). This will cause an energy outflow and, accordingly, a significant decrease in the Q value of the loop oscillations. In addition, during observations with low-spatial-resolution instruments (they constitute a majority), the radiation oscillations produced by loop oscillations with $N_t \gg 1$ must be blurred out.

Ion Viscosity, Electron Heat Conduction, and Radiative Losses

Apart from the acoustic mechanism considered above, the damping of the radial oscillations of coronal loops can be appreciably affected by ion viscosity, electron heat conduction, and radiative losses (Tsap 2000). Before making any estimates, let us ascertain the conditions under which the approximation of frequent collisions may be used to investigate the dissipative processes that accompany wave phenomena.

The approximation of frequent collisions assumes that the following inequalities hold (Braginskiĭ 1963):

$$\lambda > l, \quad T_p > \tau_i, \qquad (18)$$

where $l = v_{T_i}\tau_i \approx v_{T_e}\tau_e$ is the charged particle's mean free path, $v_{T_i} = \sqrt{2k_B T/M}$ and $v_{T_e} = \sqrt{2k_B T/m}$ are the thermal velocities of the ions and electrons, and M and m are their masses. The ion and electron collision time scales, τ_i and τ_e, are related by (Braginskiĭ 1963)

$$\tau_i = \sqrt{\frac{2M}{m}}\tau_e \approx 17\frac{T^{3/2}}{n\Lambda}\ [\mathrm{s}], \qquad (19)$$

where n is the plasma density in cm^{-3} and $\Lambda = 25.3 - 1.15\log n + 2.3\log T$ is the Coulomb logarithm, in which the temperature is in electronvolts.

Using (19), inequalities (18) can be reduced, respectively, to the relations

$$n > 2.2 \times 10^5\frac{T^2}{\lambda\Lambda}[\mathrm{cm}^{-3}], \quad n > 17\frac{T^{3/2}}{T_p\Lambda}[\mathrm{cm}^{-3}]. \qquad (20)$$

For $T = 3 \times 10^6$ K, $\lambda = 10^8$ cm, $\Lambda = 19$, and $T_\mathrm{p} = 1$–10 s, we find from (20) that $n > 10^9\ \mathrm{cm}^{-3}$. Thus, in the case of the sufficiently dense coronal loops concerned, using the approximation of frequent collisions may be justified.

After averaging over the oscillation period, the thermal energies released through ion viscosity E_v, electron heat conduction E_c, and radiative losses E_r can be represented as follows (Braginskiĭ 1963; Gordon and Hollweg 1983; Priest 1982):

$$E_v = \frac{\eta_0}{6}(\nabla\delta\mathbf{v})^2, \quad \eta_0 = 0.96nk_\mathrm{B}T\tau_\mathrm{i}; \tag{21}$$

$$E_c = \frac{\kappa_\parallel}{2}\left(\frac{k}{\omega_0}\right)^2 T(\gamma-1)^2(\nabla\delta\mathbf{v})^2, \tag{22}$$

$$\kappa_\parallel = 3.16\frac{nk_\mathrm{B}T\tau_\mathrm{e}}{m};$$

$$E_r = \frac{(3-\gamma)(5-\gamma)}{16}\frac{n^2R(T)}{\omega_0^2}(\nabla\delta\mathbf{v})^2, \tag{23}$$

$$R(T) = \frac{5\times10^{-20}}{\sqrt{T}}.$$

Note that the dependence of the radiative loss function $R(T)$ on temperature T adopted in (23) corresponds to the temperature range $T = 10^6$–$10^{7.6}$ K (Priest 1982).

Assuming that $k = \pi/L$ $(N = 1)$ and $\omega_0 = j_n v_\mathrm{A}/a$, we find from (19) and (21)–(23) that

$$\frac{E_c}{E_v} \approx \frac{15.5}{j_n^2}\sqrt{\frac{M}{m}}\beta\left(\frac{a}{L}\right)^2, \tag{24}$$

$$\frac{E_c}{E_r} \approx 4.0\times10^{13}\left(\frac{T^2}{Ln}\right)^2.$$

Since $a/L \ll 1$ and $\beta \ll 1$ for coronal loops, it follows from (24) that $E_v \gg E_c$. In turn, for $T = 3\times10^6$ K and $L = 10^9$ cm, the radiative losses $E_r > E_v$ if $n > 3\times10^{11}\ \mathrm{cm}^{-3}$. Here, however, we restrict our analysis to the effect of radial loop oscillations on the microwave radiation from flares produced by the nonthermal gyrosynchrotron mechanism, which will be quenched through the Rasin effect at frequencies $f < f_\mathrm{R} = 14n/B$ (Dulk 1985). Hence, for example, at $n = 3\times10^{11}\ \mathrm{cm}^{-3}$ and $B = 200$–300 G, we obtain $f_\mathrm{R} = 14$–21 GHz, which is in conflict with observations (Bastian 1998). Therefore, below, we restrict our analysis to loops with $n < 10^{11}\ \mathrm{cm}^{-3}$. This implies that in the case concerned, the oscillation damping due to ion viscosity exceeds the damping due to heat conduction and radiative losses.

Taking into account (2), (5), (9), and (11) and assuming that $\nabla\mathbf{v} \approx (1/r)\partial(r\delta v_r)/\partial r$, because the oscillations are transverse relative to the magnetic field, we find for the viscous dissipation decrement ν_v using (21) that

$$\nu_v \approx \frac{\langle E_v\rangle}{2W} \approx \frac{\eta_0}{12}\frac{\xi_{0_\mathrm{i}}^2}{\rho_\mathrm{i}}b, \tag{25}$$

where the angular brackets denote integration over the volume of the magnetic flux tube and the coefficient b is

$$b = \frac{J_0^2(\xi_{0_\mathrm{i}}a) + J_1^2(\xi_{0_\mathrm{i}}a)}{J_1^2(\xi_{0_\mathrm{i}}a) - J_0(\xi_{0_\mathrm{i}}a)J_2(\xi_{0_\mathrm{i}}a)}.$$

When the radial modes with frequency $\omega_0 = j_n v_{\mathrm{A_i}}/a$ are generated, $b = 1$; therefore, given (25), the oscillation Q is

$$Q_v = \frac{\omega_0}{\nu_v} \approx \frac{12}{\pi}\frac{T_\mathrm{p}}{\beta\tau_\mathrm{i}}. \tag{26}$$

Note that relation (26) matches the expression that follows from the formulas derived by Braginskiĭ (1963) for the damping decrement ν_v of plane waves in a homogeneous plasma. For $T_\mathrm{p}/\tau_\mathrm{i} = 10$–$30$ and $\beta = 0.03$–0.1, we obtain $Q_v = 4\times(10^2$–$10^3)$ from (26). Thus, if the plasma β is moderately large (<0.1), then the Q value of the radial oscillations is more likely determined by the acoustic mechanism than by the ion viscosity, let alone the electron heat conduction and radiative losses. Taking into account the damping attributable to strong plasma inhomogeneity at the tube boundary (resonance absorption and phase mixing) will have no significant effect on the results obtained (Roberts 2000). Besides, the nature of the resonance wave absorption is yet to be elucidated. Thus, according to Bellan (1994), the electrostatic properties of the generated waves near the resonance layer must be taken into account. Therefore, the conclusions that follow from the MHD approximation cannot be considered convincing.

MODULATION OF GYROSYNCHROTRON RADIATION AND DIAGNOSING THE FLARE PLASMA

The generation of radial loop oscillations causes changes in the magnetic-field strength, in the scale sizes of the emitting region, and in the plasma temperature and density. This implies that second oscillations can be observed in various wavelength ranges. Let us consider the effect of radial coronal-loop oscillations on the microwave radiation from solar flares for which the nonthermal gyrosynchrotron mechanism is generally responsible (Bastian 1998).

The spectral fluxes for optically thin and optically thick sources are, respectively,

$$F_{f_1} = \eta_{f_1}d\Omega, \tag{27}$$

$$F_{f_2} = \frac{\eta_{f_2}}{k_{f_2}}\Omega, \qquad (28)$$

where Ω is the solid angle of the source and d is its characteristic thickness. We express the emission (η_f) and absorption (k_f) coefficient in terms of the formulas for nonthermal gyrosynchrotron radiation proposed by Dulk (1985):

$$\frac{\eta_f}{Bn_\mathrm{a}} = 3.3\times10^{-24}10^{-0.52\alpha}(\sin\theta)^{-0.43+0.65\alpha} \times\left(\frac{f}{f_B}\right)^{1.22-0.90\alpha}, \qquad (29)$$

$$\frac{k_f B}{n_\mathrm{a}} = 1.4\times10^{-9}10^{-0.22\alpha}(\sin\theta)^{-0.09+0.72\alpha} \times\left(\frac{f}{f_B}\right)^{-1.30-0.98\alpha}, \qquad (30)$$

where n_a is the accelerated-electron density, $\theta > 20°$ is the angle between the magnetic-field direction and the line of sight, the spectral index for the accelerated electrons lies within the range $2 < \alpha < 7$, and $f_B = eB/(2\pi mc)$ is the electron gyrofrequency.

Let us assume that the coronal loop can be represented as a magnetic trap with sharp magnetic walls and that the trapped electrons are responsible for the observed microwave radiation. The behavior of these electrons is described by the continuity equation

$$\frac{\partial N(E,t)}{\partial t} + \frac{N(E,t)}{T_L(E,t)} = S(E,t), \qquad (31)$$

where $N(E,t) = dN(t)/dE$ is the number of electrons per unit energy interval, $T_L(E,t)$ is the electron lifetime, and $S(E,t)$ is the spectral power of the particle source.

In the case of fairly intense microwave bursts, one might expect the so-called moderate diffusion to take place in the coronal magnetic bottle (Stepanov and Tsap 1999). Therefore, $T_L = \sigma T_0$, where $\sigma = B_\mathrm{max}/B$ is the mirror ratio, $T_0 = L/v_\mathrm{a}$ is the characteristic time of electron escape from the magnetic trap through the loss cone, and v_a is the electron velocity. Electrons with $E = E_0 > 300$ keV give a major contribution to the microwave radiation from solar flares (White and Kundu 1992). Therefore, we may take the velocity to be $v_\mathrm{a} \approx c$ by assuming that the lifetime of the trapped electrons is $T_L(E,t) \approx T_L(t) = L/c$.

Since the magnetic field due to the generation of radial oscillations is $B = B_0 + \delta B\sin\omega_0 t$, because of the modulation of the mirror ratio σ, the lifetime is $T_L(t) = T_{L_0}/(1+\zeta\sin\omega_0 t)$, where $\zeta = \delta B/B$. Integrating Eq. (31) over energy E yields

$$\frac{dN(t)}{dt} + \frac{N(t)}{T_{L_0}}(1+\zeta\sin\omega_0 t) = S(t), \qquad (32)$$

where

$$N(t) = \int_{E_0}^{\infty} N(E,t)\,dE, \quad S(t) = \int_{E_0}^{\infty} S(E,t)\,dE.$$

Let the power of the source of accelerated particles be $S(t) = S_0 = \mathrm{const}$ and $N_0/T_{L_0} = S_0$ at the initial time. Assuming that

$$N(t) = N_0 + N'(t), \quad |N'(t)/N_0| \ll 1, \qquad (33)$$

and substituting (33) into (32), we obtain a differential equation with separable variables for $N'(t)$:

$$\frac{dN'(t)}{dt} + \frac{N'(t)}{T_{L_0}} + \frac{N_0\zeta}{T_{L_0}}\sin\omega_0 t = 0.$$

Given (33), its solution can be represented as

$$N'(t) = C_1(\cos\omega_0 t - \exp(-t/T_{L_0})) - C_2\sin\omega_0 t, \qquad (34)$$

where the coefficients

$$C_1 = \frac{N_0\zeta}{\chi^2(1+\chi^{-2})}, \quad C_2 = \frac{N_0\zeta}{\chi(1+\chi^{-2})}, \quad \chi = \omega_0 T_{L_0}.$$

In Eq. (34), the exponential term describes the transient process attributable to the fact that the trapped electrons tend to an equilibrium, which may be disregarded for $t \gg T_{L_0}$, and

$$N'(t) = C_1\cos\omega_0 t - C_2\sin\omega_0 t. \qquad (35)$$

Since the longitudinal magnetic flux is conserved, the volume of the oscillating loop is $V = V_0/(1+\zeta\sin\omega_0 t)$; hence, according to (33) and (34),

$$n_\mathrm{a} = n_{\mathrm{a}_0}(1+\zeta\sin\omega_0 t) - \frac{n_{\mathrm{a}_0}\zeta}{\chi^2}\frac{1}{1+\chi^{-2}} \times(\chi\cos\omega_0 t - \sin\omega_0 t), \qquad (36)$$

where $n_{\mathrm{a}_0} = N_0/V_0$. Eq. (36) suggests that in the limiting cases,

$$n_\mathrm{a} = \begin{cases} n_{\mathrm{a}_0}(1+\zeta\sin\omega_0 t), & \chi \gg 1 \\ n_{\mathrm{a}_0}, & \chi \ll 1. \end{cases} \qquad (37)$$

For flare loops with length $L = 10^9$ cm and a mirror ratio $\sigma = 3$–10 oscillating with period $T_\mathrm{p} = 3$ s, $\chi = 0.02$–$0.6 < 1$. Consequently, when moderate diffusion takes place, we may take the accelerated-electron density to be $n_\mathrm{a} = \mathrm{const}$.

Again, taking into account the law of conservation of longitudinal magnetic flux ($d \propto B^{-1/2}$, $\Omega \propto B^{-1/2}$), we have from (27)–(30)

$$F_{f_1} \propto B^{0.90\alpha-1.22}, \quad F_{f_2} \propto B^{-1.02-0.08\alpha}. \qquad (38)$$

We see from (38) that, as the magnetic field B increases in strength, the radiation flux rises for an optically thin source and falls for an optically thick source;

i.e., the corresponding oscillations are in antiphase. Note that Gotwols (1973) and Gaizauskas and Tapping (1980) investigated the effect of magnetic-field modulation only on the intensity of the synchrotron radiation.

Defining the modulation depth as $M = (F_{\max} - F_{\min})/F_{\max}$, where $F_{\max}$ and $F_{\min}$ are the maximum and minimum spectral flux densities, respectively, we find from (38) that for optically thin (M_1) and optically thick (M_2) sources

$$M_1 = 2(0.90\alpha - 1.22)\frac{\delta B}{B}, \quad (39)$$
$$M_2 = 2(0.08\alpha + 1.02)\frac{\delta B}{B}.$$

Having compared the last two expressions, we conclude that $M_1 > M_2$ for $\alpha > 2.7$ and, in addition, magnetic-field perturbations are capable of generating gyrosynchrotron-radiation oscillations with a maximum modulation depth of $\sim$30%.

If the same population of accelerated electrons is responsible for the radiation, then we can determine the particle spectral index from (39):

$$\alpha = \frac{1.22 + 1.02M_1/M_2}{0.90 - 0.08M_1/M_2}. \quad (40)$$

Using (27)–(29), let us express the optical depth in terms of the radiation fluxes F_{f_1} and F_{f_2} and the spectral index α:

$$\tau_{f_2} = k_{f_2}d = \frac{F_{f_1}}{F_{f_2}}\left(\frac{f_1}{f_2}\right)^{0.90\alpha - 1.22}. \quad (41)$$

Based on (30) and (41), we estimate τ_f at any frequency and determine the frequency $f_{\rm p}$ at which the flux of gyrosynchrotron radiation is at a maximum ($\tau_{f_{\rm p}} \approx 1$):

$$\tau_f = \tau_{f_2}\left(\frac{f_2}{f}\right)^{1.30+0.98\alpha}, \quad (42)$$
$$f_{\rm p} = f_2(\tau_{f_2})^{1/(1.30+0.98\alpha)}.$$

Finally, eliminating the accelerated-electron density $n_{\rm a}$ from the relation (Dulk 1985)

$$f_{\rm p} = 2.72 \times 10^3 10^{0.27\alpha}(\sin\theta)^{0.41+0.03\alpha} \times (n_{\rm a}d)^{0.32-0.03\alpha}B^{0.68+0.03\alpha},$$

using (30) yields

$$B = \left(\frac{f_{\rm p}}{D(\sin\theta)^{0.439-0.203\alpha+0.022\alpha^2}}\right)^{1/(0.584-0.275\alpha+0.030\alpha^2)}, \quad (43)$$

where

$$D = 10^{3.585-1.695\alpha+0.182\alpha^2} f^{0.416+0.275\alpha-0.030\alpha^2} \times \tau_f^{0.320-0.030\alpha}.$$

Let us now analyze a specific event—the solar flare of May 23, 1990 (Qin *et al.* 1996). The most interesting feature in the fine temporal structure of the microwave radiation at the impulsive flare phase ($F_{\max} \sim 10^3$ s.f.u.) was that the high Q ($Q > 200$) quasi-periodic ($T_{\rm p} \sim 1.5$ s) pulsations at $f_1 = 15$ GHz and $f_2 = 9.375$ GHz were in antiphase; the modulation depth was $M_1 \approx 5\%$ and $M_2 \approx 2.5\%$, respectively.

The observed features of the microwave radiation may be assumed to have resulted from radial flare-loop oscillations. In this case, the gyrosynchrotron radiation of the trapped electrons was optically thin at $f_1 = 15$ GHz and optically thick at $f_2 = 9.375$ GHz. As follows from (38), the radiation oscillations must then be in antiphase. Meanwhile, Qin *et al.* (1996) also proceeded from the idea of radial modes for the event under consideration. However, in contrast to our approach, the radiation sources at the two frequencies were assumed to be optically thin and the oscillations in different parts of the loop top were assumed to be shifted in phase. Still, the generation mechanism of such oscillations remains unclear.

Let us make some estimates using the derived relations. Taking into account the ratio of the modulation depths in our case, $M_1/M_2 \approx 2$, we determine the spectral index of the emitting electrons from formula (40), $\alpha \approx 4.4$. For the event in question, the flux ratio is $F_{f_1}/F_{f_2} \approx 0.5$; hence, using (41) and (42), we obtain $\tau_{f_1} \approx 0.1$ and $\tau_{f_2} \approx 2$, which is in satisfactory agreement with our model. Based on expression (35), we can also easily determine the frequency that corresponds to the maximum of gyrosynchrotron radiation: $f_{\rm p} \approx 10.6$ GHz. If we set $\theta = \pi/4$, $f = 9.375$ GHz, and $\tau_f = 2$ in (43), then we obtain the magnetic-field strength for the specified parameters, $B \approx 190$ G. Note that the inferred magnetic-field strength slightly exceeds the estimate ($\approx$130 G) by Qin *et al.* (1996).

DISCUSSIONS AND CONCLUSIONS

Here, we have analyzed the damping mechanisms for the radial oscillations of magnetic flux tubes. We showed that these oscillations could have a high Q in the solar corona.

We used the energy approach (Tsap and Kopylova 2001) to estimate the acoustic damping decrement for the radial oscillations. It follows from our analysis that if the oscillation node of the total pressure or radial velocity coincides with the magnetic flux tube boundary, then the damping decrement takes on the lowest value. Our result can be explained in terms of a weak plasma perturbation at the outer tube boundary. The oscillations will have a high Q if the plasma density inside the magnetic flux tube is much higher than the plasma density outside ($\rho_{\mathrm{i}}/\rho_{\mathrm{e}} > 10^2$), which is quite acceptable both for flare loops (Doschek 1994) and for loops in active regions (Aschwanden 2001).

By comparing various dissipative processes, we concluded that for coronal loops with $n \sim 10^9$–10^{11} cm^{-3}, the damping of the radial oscillations due to ion viscosity exceeds the damping due to heat conduction and radiative energy losses. Nevertheless, the oscillation Q is most likely determined by acoustic damping.

In our calculations, we assumed that the magnetic flux tubes were not twisted ($B_\varphi = 0$). This approximation may be considered to be justified for coronal loops with $B_z^2 \gg B_\varphi^2$, because in this case, the effect of the B_φ magnetic-field component on the linearized equations of ideal magnetohydrodynamics that describe the radial wave modes of magnetic flux tubes may be ignored (Goossens 1991). Besides, the latter inequality suggests that the coronal loops are stable against helical perturbations (Priest 1982).

We considered the effect of radial coronal-loop oscillations on the microwave radiation from trapped electrons in terms of the model of a coronal magnetic bottle for the nonthermal gyrosynchrotron mechanism. The oscillations for optically thin and optically thick sources were found to be in antiphase. The relations given here allow the spectral index for the accelerated electrons, the optical depths of the radiation sources, and the magnetic-field strength to be estimated from the modulation depth of the nonthermal gyrosynchrotron radiation. Based on the derived relations, we determined the nonthermal electron spectrum at the impulsive solar flare phase, $\alpha \approx 4.4$, and the magnetic field in the region of energy release, $B \approx 190$ G, for the event of May 23, 1990. In our estimates, we proceeded from the idea of moderate diffusion by assuming the oscillation frequency ω_0 to be much shorter than the characteristic lifetime of the trapped electrons T_{L_0}.

Here, we did not touch on the origin of the radial oscillations. Meanwhile, these wave modes can be generated, for example, by a shock wave (McLean *et al.* 1971), an increase in gas pressure (Zaĭtsev and Stepanov 1982a; Qin *et al.* 1996), or the injection of energetic protons (>1 MeV) into the loop, which cause instability of the FMS waves at the Cherenkov (Zaĭtsev and Stepanov 1982b) or bounce resonance (Meerson *et al.* 1978). In addition, the observed high-velocity plasma flows propagating along the loop are also capable of generating radial oscillations (Ryutova 1988).

In conclusion, note that high-spatial-resolution observations in various wavelength ranges are required for the nature of the solar-flare oscillations to be firmly established. In particular, X-ray data that are expected to be obtained from the R HESSI (High-Energy Spectroscopic Imager) Orbiting Station could be of great help.

ACKNOWLEDGMENTS

This study was supported by the INTAS (grant no. 00-543) and the Russian Foundation for Basic Research (project no. 00-02-16356).

REFERENCES

1. M. J. Aschwanden, Sol. Phys. **111**, 113 (1987).
2. M. J. Aschwanden, Astrophys. J. **560**, 1035 (2001).
3. M. J. Aschwanden, L. Fletcher, C. J. Schrijver, *et al.*, Astrophys. J. **520**, 880 (1999).
4. T. S. Bastian, in *Proceedings of the Nobeyama Symposium, Kiyosato, 1998,* Ed. by T. Bastian, N. Gopalswamy, and K. Shibasaki, 1998, NRO Report No. 479, p. 211.
5. P. M. Bellan, Phys. Plasmas **1**, 3523 (1994).
6. S. I. Braginskiĭ, in *Reviews of Plasma Physics,* Ed. by M. A. Leontovich (Gosatomizdat, Moscow, 1963; Consultants Bureau, New York, 1963), Vol. 1.
7. B. De Pontieu, P. C. Martens, and H. S. Hudson, Astrophys. J. **558**, 859 (2001).
8. G. A. Doschek, in *Proceedings of the Kofu Symposium, Kofu, 1993,* Ed. by S. Enove and T. Hirayama, 1994, NRO Report No. 360, p. 173.
9. G. A. Dulk, Annu. Rev. Astron. Astrophys. **23**, 169 (1985).
10. P. M. Edwin and B. Roberts, Sol. Phys. **88**, 179 (1983).
11. V. Gaizauskas and K. F. Tapping, Astrophys. J. **241**, 804 (1980).
12. M. Goossens, in *Advances in Solar System Magnetohydrodynamics,* Ed. by E. R. Priest and A. W. Wood (Cambridge Univ. Press, Cambridge, 1991; Mir, Moscow, 1995).
13. B. E. Gordon and J. V. Hollweg, Astrophys. J. **266**, 373 (1983).
14. B. L. Gotwols, Sol. Phys. **33**, 475 (1973).
15. S. R. Kane, K. Kai, T. Kosugi, *et al.*, Astrophys. J. **271**, 376 (1983).
16. P. Kaufmann, G. Trottet, C. G. Giménez de Castro, *et al.*, Sol. Phys. **197**, 361 (2000).

17. B. Kliem, M. Karlicky, and A. O. Benz, Astron. Astrophys. **360**, 715 (2000).
18. D. J. McLean, K. V. Sheridan, R. T. Stewart, and J. P. Wild, Nature **234**, 140 (1971).
19. B. I. Meerson, P. V. Sasorov, and A. V. Stepanov, Sol. Phys. **58**, 165 (1978).
20. V. M. Nakariakov and L. Ofman, Astron. Astrophys. **372**, L53 (2001).
21. E. R. Priest, *Solar Magnetohydrodynamics* (Reidel, Dordrecht, 1982; Mir, Moscow, 1985).
22. Z. Qin, C. Li, Q. Fu, and Z. Gao, Sol. Phys. **163**, 383 (1996).
23. B. Roberts, in *Advances in Solar System Magnetohydrodynamics,* Ed. by E. R. Priest and A. W. Wood (Cambridge Univ. Press, Cambridge, 1991; Mir, Moscow, 1995).
24. B. Roberts, Sol. Phys. **193**, 139 (2000).
25. B. Roberts, P. M. Edwin, and A. O. Benz, Astron. Astrophys. **279**, 857 (1984).
26. H. Rosenberg, Astron. Astrophys. **9**, 159 (1970).
27. M. R. Ryutova, Zh. Éksp. Teor. Fiz. **94** (8), 138 (1988) [Sov. Phys. JETP **67**, 1594 (1988)].
28. H. C. Spruit, Sol. Phys. **75**, 3 (1982).
29. A. V. Stepanov and Yu. T. Tsap, Astron. Zh. **70**, 895 (1993) [Astron. Rep. **37**, 452 (1993)].
30. A. V. Stepanov and Yu. T. Tsap, Astron. Zh. **76**, 949 (1999) [Astron. Rep. **43**, 838 (1999)].
31. Y. T. Tsap, Sol. Phys. **194**, 131 (2000).
32. Yu. T. Tsap and Yu. G. Kopylova, Pis'ma Astron. Zh. **27**, 859 (2001) [Astron. Lett. **27**, 737 (2001)].
33. G. N. Watson, *Treatise on the Theory of Bessel Functions* (Cambridge Univ. Press, Cambridge, 1945; Inostrannaya Literatura, Moscow, 1949).
34. S. M. White and M. R. Kundu, Sol. Phys. **141**, 347 (1992).
35. D. R. Williams, K. J. H. Phillips, P. Rudawy, *et al.*, Mon. Not. R. Astron. Soc. **326**, 428 (2001).
36. J.-P. Wulser and N. Kampfer, NASA Conf. Publ., No. 2449, 301 (1987).
37. V. V. Zaĭtsev and A. V. Stepanov, Issled. Geomagn. Aéron. Fiz. Solntsa **37**, 3 (1975).
38. V. V. Zaĭtsev and A. V. Stepanov, Pis'ma Astron. Zh. **8**, 248 (1982a) [Sov. Astron. Lett. **8**, 132 (1982a)].
39. V. V. Zaĭtsev and A. V. Stepanov, Astron. Zh. **59**, 563 (1982b) [Sov. Astron. **26**, 340 (1982b)].
40. V. V. Zaĭtsev and A. V. Stepanov, Pis'ma Astron. Zh. **15**, 154 (1989) [Sov. Astron. Lett. **15**, 66 (1989)].
41. V. V. Zaĭtsev, A. V. Stepanov, and Yu. T. Tsap, Kinematia Fiz. Nebesnykh Tel **10**, 3 (1994).
42. V. V. Zaitsev, A. V. Stepanov, S. Urpo, and S. Pohjolainen, Astron. Astrophys. **337**, 887 (1998).
43. D. M. Zarro, J. L. R. Saba, and K. T. Strong, NASA Conf. Publ., No. 449, 289 (1987).
44. A. M. Zodi, P. Kaufmann, and H. Zirin, Sol. Phys. **92**, 283 (1984).

Translated by V. Astakhov

Astronomy Letters, Vol. 28, No. 11, 2002, p. 792. Translated from Pis'ma v Astronomicheskiĭ Zhurnal, Vol. 28, No. 11, 2002, p. 880.
Original Russian Text Copyright © 2002 by the Editorial Board.

ERRATA

Erratum: "Orbital Evolution of Saturn's New Outer Satellites and Their Classification"

[*Astronomy Letters* 27, 455 (2001)]

M. A. Vashkov'yak

The third panel of Fig. 10 erroneously shows a plot of the longitude of the ascending node against time. Actually, this panel must show a plot of the pericenter argument against time. The correct Fig. 10 is given below.

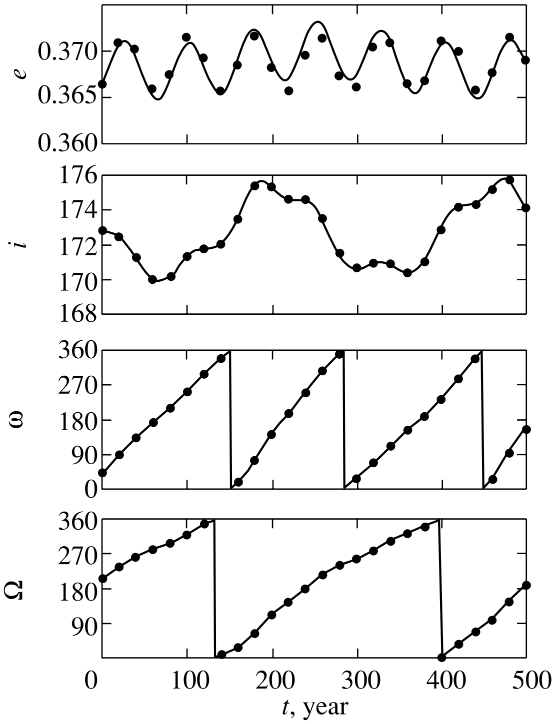

Fig. 10. Orbital evolution of S/2000 S1.